January 2020

Advanced Electrodes And Electrolytes For Long-Lived And High-Performance Lithium-Sulfur Batteries

Deepesh Gopalakrishnan
Wayne State University

ADVANCED ELECTRODES AND ELECTROLYTES FOR LONG-LIVED AND HIGH-PERFORMANCE LITHIUM-SULFUR BATTERIES

by

DEEPESH GOPALAKRISHNAN

DISSERTATION

Submitted to the Graduate School

of Wayne State University,

Detroit, Michigan

in partial fulfillment of the requirements

for the degree of

DOCTOR OF PHILOSOPHY

2020

MAJOR: MECHANICAL ENGINEERING

Approved By:

_____

Advisor Date

_____

_____

_____

_____

DEDICATION

Dedicated to my parents Mr. Gopalakrishnan and Mrs. Pushpalatha, my sister Divya, my wife Aparna Unni, my nephews Aadhi and Adhiseshan, my brother in law Udayasankaran, and my best friend Sandeep Nair, who have always supported me through unconditional love.

ACKNOWLEDGMENTS

Firstly, I would like to thank my advisor Dr. Leela Mohana Reddy Arava for giving me the wonderful opportunity to complete my Ph.D. thesis under his supervision, it is truly an honor. Thank you for all the advices, ideas, moral support, and patience in guiding me throughout this project. I appreciate all your contributions of time and funding to make my Ph.D. experience productive and stimulating. Your wealth of knowledge in the field of Material Science & Batteries is always inspiring. Thank you for giving me the opportunity to grow in this field of battery research. Also, I would like to acknowledge National Science Foundation (grant nos. 1751472, 1748363), ACS Petroleum Research Fund (ACSPRF: 57647-DNI10) and Hartley Family Foundation through Rice University (Contract R07721) for the funding support of my research.

I would like to thank Dr. Xin Wu, Dr. Guru Dinda, Dr. Ratna naik and Dr. Mahbub Islam for being on my doctoral committee and providing with useful critiques for my work. I thank my department chair Dr. Nabil Chalhoub and Secretary Lisa Rapicano for their help and support in getting approvals done quickly. I thank Dr.Verani and Dr. Rabuffetti from Department of Chemistry, Wayne state university for giving me access to their labs for the synthesis and characterization of different materials used for my Ph.D research works. Also, I would like to thank Dr. Zhi Mei, Department of Chemistry, Wayne State University for helping me with SEM and TEM samples.

I am deeply grateful to my former advisors Dr. Pradeep Thalappil (IIT Madras, India), Dr. M.M. Shaijumon (IISER TVM, India) and Dr. Seeram Ramakrishna (NUS, Singapore) for introducing me to the filed of research on material sciences and for keeping me always motivated. I extend my sincere gratitude for Dr. Sreejith Sivaramapanicker, Dr. Sreeprasad Sreenivasan, Dr. Girilal, Dr. Adarsh P, Dr. Molamma Prabhakaran, Dr. S. Balakumar, Dr. Prasanth krishnan and Dr. Dijo Damien for their support, guidance and valuable suggestions throughout my research

career. I sincerely thank Dr. Renjith Sasi, Dr. Ayana Baskaran and Dr. Binitha G for their personal and scholarly interactions, suggestions at various points of my research programme. I am thankful to my colleagues at the Functional Nanomaterials and energy devices laboratory for providing their support in my research work: Dr. Hesham Al Salem, Dr. Bhuvaneshwari Dharmarajan, Dr. Khalid Ababtain, Dr. Nirul Masurkar, Abdualrazzag Sawas, Uday Praveen, Kiran Mahankali, Sathish Rajendran, Sudhan Nagarajan and Sanjeev Porchelvan. I am grateful to work with Dr. Babu Ganguli and Dr. Naresh Thangavel who helped me a lot and cleared my scientific doubts throughout my Ph.D. journey. A special thanks for Dr. Munaiah Yeddala for helping me in correcting and modifying the thesis. I had immense pleasure in guiding and nurturing research study of undergraduate and graduate students Neha Bhagirath, Ann Amarachi Mark, Andrew Lee, Samia Alkatie, Deviprasad, Victoria Lebryk, Rijo John and Raghavendra.

I would like to thank my parents Mr. Gopalakrishnan and Mrs. Pushpalatha, my sister Divya, my nephews Aadhi and Adhiseshan, my brother in law Udayasankaran for their endless encouragement in all my pursuits and inspiring me to follow my dreams. I am especially grateful to my parents and my sister, who supported me emotionally and believed in me and wanted the best for me. And most of all for my loving, supportive, and encouraging wife Aparna whose faithful support during the final stages of this Ph.D. is also greatly appreciated. Special thanks to my in-laws Mr. Unnikrishnan, Mrs. Suja and Harikrishnan for their love, care, and support. Thank you, my best friend and brother Sandeep Nair, for your love and support, sense of humor, and advice, was more valuable than you could ever imagine. And special thanks to Dr. Sreeja Sekhar and Dr. Arun Sankar for listening, offering me advice, and supporting me through this entire process. Also, Thank you my "Poker Buddies" for all your love, care, wishes, prayers, and constant support.

TABLE OF CONTENTS

LIST OF TABLES

LIST OF FIGURES

CHAPTER 1 INTRODUCTION

1.1 Lithium Ion Batteries

Over the past decades, the energy storage has become a universal concern due to the increasing demand for the fossil fuels, their fast depletion and growing environment concerns leading to serious problems to human health[1-3]. Development of clean and sustainable energy technologies including biomass, solar, wind, and hydro resources is crucial to address this inevitable challenge. However, solar radiation, wind and waves are energy sources that are seasonal in availability and thus, these sources require energy storage[4]. In this regard, development of greener power sources in the form of electrochemical energy storage devices plays an important role. Thus, batteries, fuel cells, photovoltaic devices and super capacitors that can efficiently store and deliver energy on demand attract considerable attention as a promising route for energy storage[5, 6]. Electrochemical energy storage (EES) devices especially batteries become the promising technology through their technical advancement along with attractive characteristics including high round-trip efficacy, flexible power, long cyclability, and low maintenance[7]. Rechargeable batteries, such as redox flow batteries make the energy storage technology viable and contribute towards integration of renewable resources into the grid to balance the intermittent power supply. Rechargeable Li-ion battery (LIB) have become successful energy storage device specifically for portable electronics due to its high gravimetric energy density and power density. Figure 1 is the comparison of different battery technology in terms of energy density per unit volume and weight. Being the lightest metal, Lithium gives high gravimetric density and it is also considered as the most electropositive metal with much negative electrochemical reduction potential, -3.04 V vs SHE which offers high energy density to the batteries[7]. Thus, there was a tremendous development in the portable electronic devices enabling

the visualization of cellular phones and laptops achieved through the higher volumetric and gravimetric energy density of a Li battery[8].Lithium batteries with layered Titanium sulfide (TiS_2) as cathode and metallic lithium as anode was first reported by Whittingham in 1976[9]. Later, Yoshino successfully built a prototype cell with carbon-based anode and $LiCoO_2$ (Lithium Cobalt Oxide) as cathode in 1987[10] which is considered as the first generation lithium ion batteries[11]. This battery design inspired the large-scale manufacturing of lithium ion batteries in early 1990s and later was commercialized by Sony in 1991. There is a tremendous progress in the Li ion battery field in past two decades, the introduction of lithium iron phosphate ($LiFePO_4$) by Goodenough (1996) and high capacity anode, C-Sn-Co by Sony (2005) are considered as some of the milestones during the journey. However, significant challenges like cost-effectiveness, safety, energy density, charge/discharge rates, and cyclability are some of the issues that limit their development for the potential applications such as electric vehicles(EV)[12, 13].

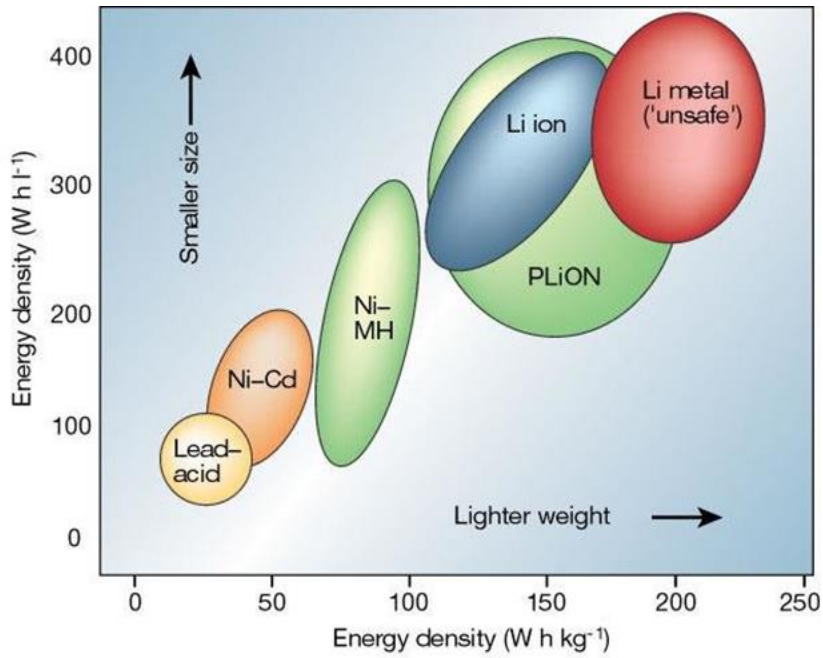

Figure 1.1 Comparison of different battery technology[7].

For lithium-ion batteries to meet the requirements in the field of electric vehicles and other storage systems, it must be improved in terms of cost-effective and safety along with other requirements such as cell cyclability, higher energy and power density, and ability to operate at wide range of temperatures.

1.2 Working principle of a lithium-ion battery

An electrochemical cell or battery consists of two electrodes – anode and cathode, which are separated by Separator and connected through the electrolyte. During the operation of the battery, the electrolyte conducts the ionic component of the reaction through them while forcing the electronic part to travel through the external circuit. A conventional lithium ion battery consists of graphite anode and lithium metal oxide (commonly $LiCoO_2$) will be cathode. Li ions get intercalate and deintercalated into the solid electrode during the charging and discharging of the battery. Like any other electrochemical system electrolyte conducts ions and electron travel through external circuit. The electrochemical reaction occurs at the electrodes during charging will be reversed during discharging of the battery i.e. these electrochemical reaction or highly reversible in nature[14] [15, 16].

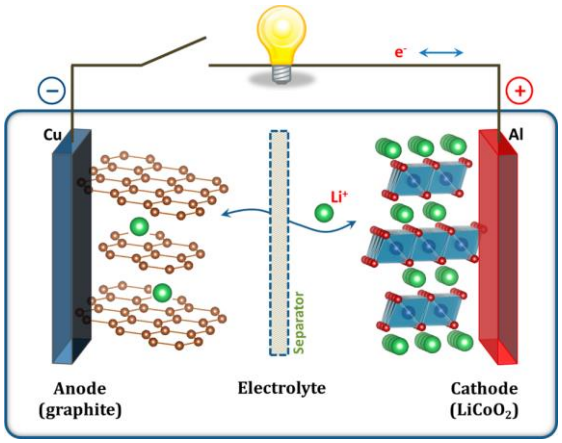

Figure 1.2 Schematic illustration of the Li-ion battery ($LiCoO_2$/Li+ electrolyte/graphite).

In a conventional Li ion battery (Figure 1.2), during charging the lithium ions will get intercalate into the negative electrode and the positive material gets oxidized, while the negative material will get reduced. During the discharge process, the reverse process happens. The electrochemical reactions at the electrode and overall chemical reaction is as follows[6].

At the positive electrode:

$$xLi^{+} + Li_{1-x}CoO_2 + xe^{-} \leftrightharpoons LiCoO2 \qquad (E_c = 0.6 \text{ V vs. SHE}) \qquad (1.1)$$

At the negative electrode:

$$LiC_6 \leftrightharpoons Li_{1-x}C_6 + xLi^{+} + xe^{-} \qquad (E_a = -3.0 \text{ V vs. SHE}) \qquad (1.2)$$

Accordingly, the net cell reaction during charge-discharge processes is:

$$LiC_6 + Li_{1-x}CoO2 \leftrightharpoons Li_{1-x}C_6 + LiCoO_2 \qquad (E_{cell} = 3.6 \text{ V}) \qquad (1.3)$$

The energy that can be drawn out of the battery will mostly depend on the basic electrochemical reactions at both electrodes, even though there are several other factors influencing its performance or rate capability. Few among those factors are the electrode design, ionic conductivity of the electrolyte and separator characteristics are which influence the charge transfer reaction, diffusion rates and magnitude of energy loss.

Electrochemical reaction kinetics play a major role towards the overall polarization. The activation polarization is one related to the kinetics if the charge-transfer reactions happens at the electrode/electrolyte interface. Secondly, the ohmic polarization which can be ascribed to the resistance of each cell components and to the resistance due to contact issues between the cell components. The concentration polarization comes next which is due to mass transport limitations during the battery operations. The current-voltage characteristics during discharge is shown in the

figure, determining the cell capacity, the effect of the discharge-charge rate and overall information on the state of the battery[17].

1.3 Challenges of Lithium Ion Batteries

Although Li ion battery has a very impressive success story, there are still some notable challenges in the development of next generation batteries. The battery performance is related to the intrinsic material property of the anode and cathode. The information about Solid electrolyte interface (SEI) which is one of the vital factors that decide the performance of the battery is not sufficient. There is an urgent need for high capacity anodes and high potential cathodes and electrolytes with wide electrochemical potential develop next generation batteries[13, 18, 19].

To improve the energy density of Li ion batteries, lot of potential anode and cathode are discovered. There is a much amount of progress in the positive pole of the electrode, called cathode which absorbs Li ions as the battery delivers its power. Scientist are developing smaller and thinner cathode materials to improve Li ion mobility by shortening the distance between the electrodes. But the results of the efforts are still under progress and remains challenging. Graphite based electrode have been using as anode to avoid the dendrite formation during the charging of the battery. Other materials such as , Sn and Si are also proposed as anodes in Lithium ion battery. Theoretical capacities of Sn and Si are 960 mAh/g and 3579 mAh/g respectively which is higher than that of graphite anode. However, the high-volume changes (~ 400 % and 257 % for Silicon and Sn anodes respectively). Along with that, cheap and large-scale production of Si nanomaterial is challenging. Pulverization of Sn based anodes leads to poor cycling performance. A composite of Si and Sn is also explored as anode material in Li ion battery[20].

In case of cathode materials, existing candidates like $LiCoO_2$ and $LiFePO_4$ are expensive, highly toxic and have very low capacity. The cell capacity is limited by the capacity of cathode. Recent NMC (Ni-Co-Mn based metal oxides) cathode materials are highly attractive in the industrial prospective, though the specific capacity is moderate. NMC cathodes also have Co and Ni which are found to be very expensive and toxic. It is necessary to find out an affordable, nontoxic, eco-friendly, possess high specific capacity and long-term durability[21].

Separator in battery prevent the contact between the electrodes which is permeable to the ions to flow through the electrolytes[22]. These separators can be pierced by the dendrites which grow across the electrodes and short-circuit the battery ending up in shortening the battery life. When the capacity of the battery is attributed by the electronic and structural behavior of electrodes, the poor cycle life is due to the side reactions happening at the electrode – electrolyte interface. Thus, formulating an electrolyte which is chemically stable at the interface with respect to its operating liquid is important[23].

The battery safety measures are as important as their performance, because even a small failure which can leads to leaves a disaster to the manufacturer, Sony in 1992 and Samsung in the case of galaxy mobile phones are some of the examples[21]. In the times of increasing demand for EVs significant investment should be made on battery management systems to ensure safety. It is required to develop non-flammable Li ion batteries which includes those based on aqueous or ceramic electrolytes. Electrode (high voltage cathodes and high capacity anodes) electrolyte interaction in terms of stability should be studied for developing next generation Li ion batteries. Towards this, a better understanding of interaction between electrode materials and electrolytes is required urgently. Higher the energy of a battery higher the chances of failure (low safety) of the

battery. Hence, before commercialisation it should be ensured that they meet all the standardised safety requirements[21].

In addition to the technical challenges discussed above, there are other challenges on which less attention was paid.

- Limited availability of Li sources makes it difficult to reduce the cost of Li ion batteries.
- Lack of development in recycling of Li ion batteries materials.

Therefore, it is high time for the development of those advanced battery technologies (such as Na-ion, Mg-ion, Ca-ion, Al-ion, and F ion batteries) beyond Li-ion batteries.

1.4 Li -O_2 and Li-S chemistry

Even though the Li ion battery technology is fully developed to an extent, the highest energy storage that they can deliver is not high enough to meet the current requirement of emerging applications, such as all electric vehicles. New technologies like Li-air (Li-O_2) and Li- Sulfur (Li-S) are getting more attention which have the potential to address the shortcomings of Li ion batteries[1, 24, 25]. Both Li-O_2 and Li-S are good enough to attaining an energy density greater than 400 Wh kg^{-1}, and the cathode material are less expensive, eco-friendly and highly abundant than the conventional transition metal oxide cathode of li ion battery[26]. The Li-S and Li- O_2 systems share same anode and highly active cathode components such as sulfur and oxygen respectively which undergo conversion reaction with lithium, having multiple steps and several intermediates. the nature, reactivity and stability of the intermediate species are extremely different for S and O_2 reactions, which can be seen in their characteristic charge-discharge polarization curves. The cycle life and rate capability of both the system are extremely different[27]. Thus, the exploration of new materials for these chemistries is one of the challenges

that attracts the attention of the research community. There is tremendous research going on in the field of Li-S and Li-O_2 batteries expecting their commercialisation in the future[28, 29].

Li-O_2 battery is an outstanding system when compared with the Li-S in terms of energy density. However, highly reactive intermediates, high polarization, short cycle life and inconsistent charge-discharge behavior dampened the glory of this system[30]. There is an intensive research going on with new electrolyte formulations, new cell configurations and development of novel electrocatalysts to decrease the cell polarization and increase cycle life of this alluring system[31-34]. The inferences acquired on electrodes for fuel cells over the past few decades can be used as a reference for the development of Li-O_2 batteries. Issue associated with the volatile electrolyte, getting evaporated into the gas phases can lead to the battery failure. One of the other challenges is tackling the formation of solid phases which has never occurred in a fuel cell, makes Li –O_2/ S battery chemistry unexplored[21].

1.5 Li-S batteries

Sulfur is one of the 5th most abundant elements in the earth crust and it offers high theoretical capacity of 1672 mAhg^{-1}. Due to its high theorical capacity, abundance and ecofriendly nature makes sulfur as the most suitable cathode for lithium-based technologies. A typical Li-S cell consist of Li metal anode, organic electrolyte and sulfur containing cathode where electrical energy will be stored. The open circuit potentials of Li-S battery is about 2.4 – 2.5 V[24, 35-37]. During discharge of the battery Lithium ions produced at the anode diffuse through membrane and reduce the sulfur to lithium polysulfide at the cathode electrode. The electrochemical reactions during discharge are given below.

At anode

$$Li \rightarrow Li^{+} + e^{-} \quad (1.6)$$

At cathode

$$S + 2Li^{+} + 2e^{-} \rightarrow Li_2S \qquad (E^{\circ} \approx 2.15\ V\ vs\ Li / Li^{+}) \quad (1.7)$$

overall cell reaction

$$2Li + S \rightarrow Li_2S \quad (1.8)$$

1.5.1 Voltage characteristic of Li–S battery

The discharge process can be divided into four stages. In the first stage, the reduction of cyclo-S_8 produces high-order lithium polysulfides Li_2S_8, which is soluble in organic electrolyte and thus, dissolves in liquid electrolyte.

$$S_8 + 2\ Li^{+} \rightarrow Li_2S_8 \quad (1.9)$$

In stage 2, high-order lithium polysulfides (dissolved Li_2S_8) reduces to lower order lithium polysulfides Li_2S_x ($4 < x \leq 8$), which are still soluble in the electrolyte.[35, 38] During this stage, the cell voltage decreases linearly and the viscosity of the electrolyte solution increases.

$$Li_2S_8 + 2Li^{+} \rightarrow Li_2S_{8\_n} + Li_2S_n \quad (1.10)$$

In stage 3, the soluble LiPS gets reduced to the insoluble lithium disulfide (Li_2S_2) or lithium sulfide (Li_2S), which accumulates on the cathode surface, forming an insulating passivation layer. This stage contributes to the major capacity of the Li–S cell.

$$2Li_2S_n + (2n-4)Li^{+} \rightarrow n\ Li_2S_2 \quad (1.11)$$

$Li_2S_n + (2n-2)Li^+ \rightarrow n\ Li_2S$ (1.12)

In the final stage, the insoluble Li_2S_2 to insoluble Li_2S and this is reflected by a steep voltage decline in the discharge profile.

$Li_2S_2 + 2Li^+ \rightarrow 2Li_2S$

The two discharge plateaus at 2.3 and 2.1 V represent the conversions of S_8 to Li_2S_4 and Li_2S_4 to Li_2S, respectively. The charge profile is complicated due to the redox shuttle of dissolved LiPS and poor nucleation of elemental sulfur. During charge the as formed Li_2S converted to S_8 via the formation of the intermediate lithium polysulfides. Typical charge discharge curve of Li-S battery is shown in the figure. The initial sharp rise in the charge profile is due to the polarization of the Li_2S passivation layer on the cathode surface followed by a shallow dip which is due to the depolarization by the oxidation of insoluble Li_2S to soluble LiPS.. Thus, the two charge voltage plateaus are attributed to the oxidation of short to long chain LiPS and long LiPS to elemental sulfur respectively[35].

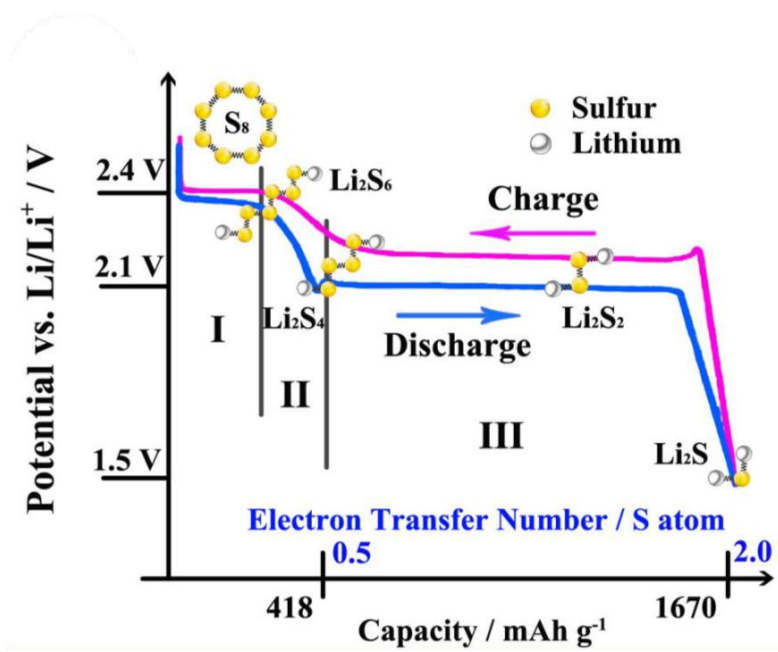

Figure 1.3 Voltage profile of Li-S cell with the intermediate products[39].

1.6 Problems and challenges

In the past few decades, Li-S battery chemistry has developed vigorously, and substantial achievement has been realized. However, there are many scientific and technical problems hindering their practical applications and they are the following.

1.6.1 Polysulfide shuttling effect

The dissolution of LiPS facilitates the electrochemical reaction of the insulating sulfur species which can cause severe redox shuttle between the sulfur cathode and Li anode. This LiPS shuttle results in low coulombic efficiency for charging and fast self-discharge for storage[40]. Soluble long chain LiPS formed during the charging process can diffuse to the Li anode surface and are either electrochemically reduced or chemically react with lithium to generate short chain LiPS. These formed short chain LiPS diffuse back to sulfur cathode and undergo oxidation to regenerate long chain LiPS. These reactions cause problems like reducing charging coulombic efficiency, Li anode corrosion and polarizing Li anode when the insoluble discharge products get deposited onto Li surface[41].

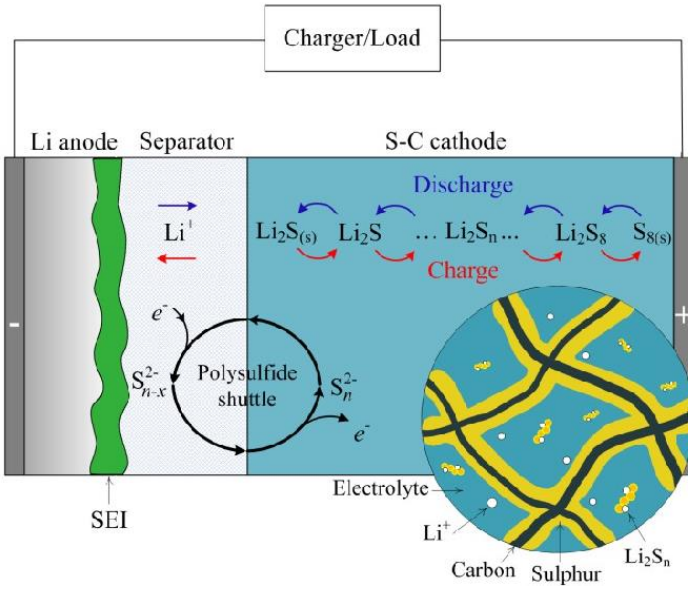

Figure 1.4 Summary of the effects of polysulfide shuttle phenomenon[42].

Significant progress has made on Li-S rechargeable battery field with the invention of novel nanocomposites, electrolytes, and various cell configurations to address the above-mentioned issue. A remarkable improvement in the field of Li-S battery have been triggered with the invention of new electrolytes such as ether chains, glymes, polyethileneoxide etc[43-45]. Though the recent research shows prominent results, efforts are needed towards commercialization of Li-S battery.

1.6.2 Sulfur cathode

There are many problems in the Li-S battery chemistry in relation to the sulfur cathode. Sulfur being an electrical insulator, high amounts of conductive carbon is required to promise reasonable utilization of sulfur active material and at least 70% of sulfur content is needed to achieve high energy density Li-S battery. In addition, the insoluble discharge products like Li_2S_2 and Li_2S on the cathode surface form a passivation layer on the electrode due to their insulating nature which also reduces the utilization of sulfur active material. The Li_2S species on the electrode surface prevent the contact of unreacted sulfur with the reaction sites and leads to the low active sulfur utilization and thereby low capacity[46]. Significant volumetric change about 79% by the conversion process between elemental sulfur and lithium sulfur is considered as another problem with Li-S battery cathode. The repeated dissolution and precipitation of sulfur active material can degrade the structure of cathode leading to the fast capacity fade. Thus, with the impregnation of sulfur into the porous carbon can help in buffering from the expansion which benefit in long cycling stability[47]. Dissolution of long chain PS into the organic electrolyte leads to the formation of voids in early stage of discharge is another problem with the existing Li-S electrode chemistry. Also, the conventional binders for Li ion batteries like Poly(vinylidene fluoride) cannot

be used here as they swell in the presence of organic electrolyte and there by cannot retain the porous structure of cathode leads to the capacity fading in Li-S batteries[48].

1.6.3 Lithium anode

The main issues with the Li anode in the Li-S battery are the corrosion, low coulombic efficiency, and rough morphology of Li plating, which are related to the reactions with dissolved PS. These parasitic reactions with the Li metal anode can form passivation layer on the electrode surface leading to the capacity fade. The reaction between the dissolved PS and Li anode is considered as the most important factor in initializing thermal runaway in Li-S batteries at high temperature[49].Another big problem with anode is the formation of needle shaped dendrites on their surface which are due to the uneven coating of the Li ions while battery is charging. Separators in battery prevent the contact between the electrodes which are permeable to the ions to flow through the electrolytes[50].These separators can be pierced by the dendrites which grow across the electrodes and short-circuit the battery ending up in shortening the battery life.

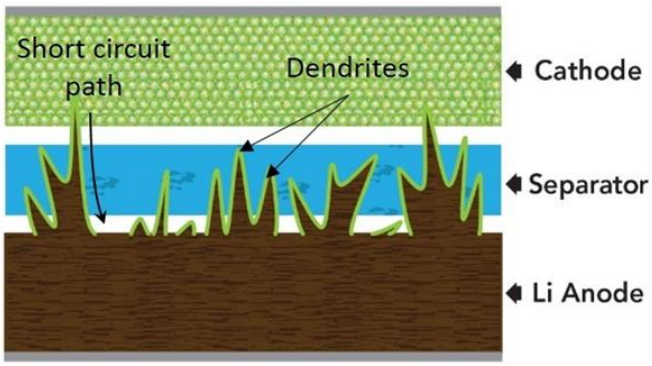

Figure 1.5 The formation of Li dendrites

1.6.4 Electrolyte

Electrolyte is the main key in determining the operation temperature range of Li–S batteries and influencing the dissolution and chemical stability of LiPS. The PS in the electrolyte will

disproportionate into low soluble or insoluble short-chain PS and elemental sulfur, which can precipitate out and clog the separator pores. Hence, in terms of the sulfur utilization and reaction kinetics, a liquid electrolyte that can stabilize the PS is highly needed; on the other hand, this stimulates the redox shuttle of PS. Electrolytes can also affect the coulombic efficiency and the formation of a passivation layer on the Li anode. Therefore, the electrolytes for the Li-S battery should have high ionic conductivity, moderate PS solubility, low viscosity, wide electrochemical window, good chemical stability, and reliable safety[9]. However, there is no electrolyte serve all these requirements and the practical solution is to optimize the electrolyte formula by a solvent mixture and additives. Conventional salts used in Li-ion batteries cannot be used in Li-S batteries and the one in Li-S should be chemically stable with PS which can form stable protective film on Li surface.

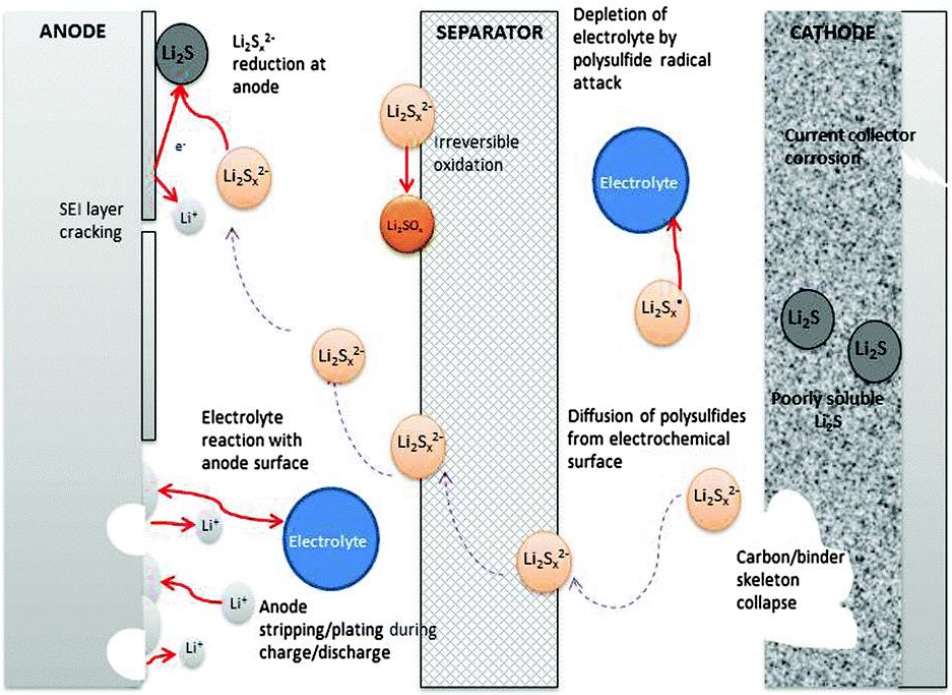

Figure 1.6 Degradation mechanism due to the electrolyte[42].

Thus, Li-S battery faces many challenges which can be summarized as follows. The insulative nature of the sulfur in the cathode (electrical conductivity is 1 x 10^{-15} S/m) which diminishes the sulfur utilization. To improve the conductivity of the cathode, highly conductive material like carbon are compounded with sulfur and employed as cathode. However, these carbon hosts can decrease the energy density of the battery. The discharge products like Li_2S_2 and Li_2S are electrochemically inactive which are responsible for irreversible capacity fading. Deposition of these inert end products (Li_2S_2 and Li_2S) on electrodes reduce the utilization of active materials and diminution of specific capacity[35]. As mentioned above, the dissolution of polysulfides into the electrolyte is a problem of Li-S battery where the dissolved polysulfides diffuse through membrane to anodic compartment react with lithium and yields short chain polysulfides which gets deposited onto the lithium anode surface [51, 52]. Adsorption of LiS_x onto the cathode surface and impregnating them into nanostructures are the possible ways to overcome the shuttle effect[36]. Volume expansion is another challenge which leads to cracks in the conductive network resulting in drastic fade in the battery performance. Most of the electrolytes used in Li-S batteries are ether based and the polysulfide are highly soluble in the solvents (ethers) and could not suppress the shuttling of polysulfides. The ethers are highly flammable, and the boiling point of ether-based electrolytes are low which offer a great threat to the safety of the battery. Therefore, the development of safer and efficient electrolyte is also essential for Li-S battery. Lithium dendrite formation affects the safety of the battery by causing short circuit[53]. Therefore, protection of Li metal is also crucial area to focus on for practical realization of Li-S batteries[38].The heterogenic anode materials can lead to the formation of dendrite on their surface which inversely effects the Li battery performance in terms of safety and cycle life. The dendrite like growth limiting the battery stability can be due to the continuous Li deposition and stripping which ends up in cell

short circuiting, cell failure and later its explosion. Thus, researchers have taken tremendous efforts towards suppressing the dendrite growth through various techniques like electrode modification, implementing solid, different kinds of electrolytes including solid gel electrolytes, designing different cell configurations. The mere kinetic performance of solid electrolytes due to their poor conductivity and high interfacial resistance, leads to their limited implementation in commercial batteries[12]. Thus, the electrochemical process inside lithium-sulfur batteries is a complex process, and the various problems mentioned above must be addressed to realize the full potential of Li-S battery[38].

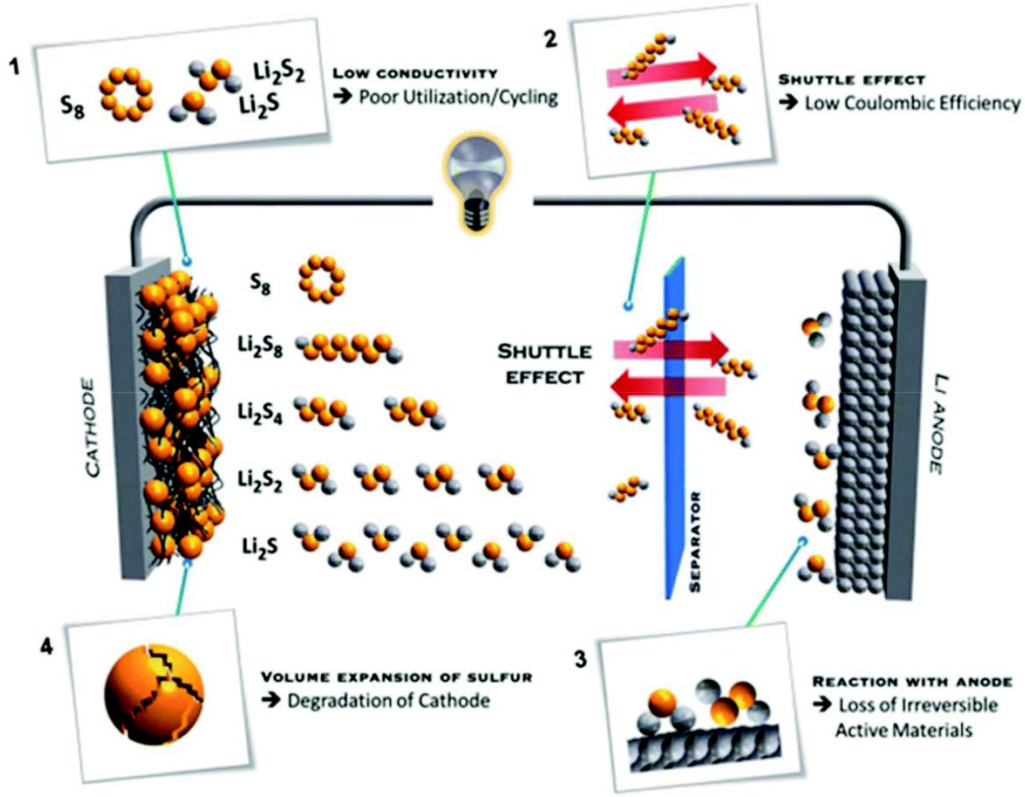

Figure 1.7 Schematic illustration of the challenges faced by Li-S batteries[54].

1.7 Proposed strategies towards suppressing polysulfide shuttle effect and Li dendrite formation

As discussed in the previous section, the uncontrolled growth of Li dendrites and fatal effect of polysulfides shuttle limit the practical applications of Li-S batteries[55, 56]. Many efforts have been taken towards addressing these two major issues[57]. Among them, restraining polysulfides shuttle by confining sulfur in the porous hosts was one of the widely applied approach where the generated intermediate polysulfides are immobilized either by physical adsorption and/or chemical binding. Though enhanced cycling performance of Li-S batteries can be attained through these the encapsulation approaches, it fails in the complete prevention of dissolution of polysulfides particularly with the high sulfur loading cases due to the limited adsorption capacity and binding sites[58, 59]. Protecting layer on the surface of Li metal can prevent the reaction between polysulfides and Li metal along with inhibiting the dendrite growth[60]. However, excess formation of solid-electrolyte interphase (SEI) layer on the Li metal surface lead to a high resistance at the electrode-electrolyte interface causing poor rate performance.

An overview of different strategies to confine the polysulfides to prevent the polysulfide shuttling process is discussed initially followed by the efforts taken to protect Li anode from dendrite formation and relieving the consequent degradation and safety concern.

1.7.1 Strategies to prevent polysulfide shuttling process in Li-S batteries

(i) Porous carbon to entrap polysulfides

In the past decade, much efforts have been devoted to the physical confinement of lithium polysulfides (LiPS) using carbonaceous materials[61]. Various 3D porous carbon materials including hollow carbon spheres, carbon nanotubes, nanofibers and microporous carbons been

used as host for sulfur to suppress the dissolution of LiPS into the electrolytes through their nanostructured pores. The impregnation of sulfur within the 2D graphene nanosheets or conductive polymers was also found to be an effective way to trap LiPS. Carbonaceous materials are also capable for improving the electron conduction and providing pathways for easy Li+ diffusion thereby enhancing the cycling performance of Li-S batteries. However, these non-polar carbonaceous hosts with their weak interaction with polar LiPS species can only spatially confine the LiPS resulting a rapid capacity fading over the long-term cycling. The eventual migration of LiPS out of the carbon hosts will not only cause the loss of active materials, but also the uncontrolled deposition of discharged products. This can lead to the cathode passivation and deterioration. Thus, there is an urgent need of materials with stronger binding for LiPS, to achieve stable cycling performance of the Li-S cell[62].

(ii) Chemical approaches for polysulfide adsorption

Chemical adsorption benefits the strong chemical binding for LiPS with the sulfur host materials and thus, improved cyclability can be achieved. Functionalization of carbonaceous materials make them polar which can strongly interact with polar LiPS, is the most common approach taken in this aspect. Graphene oxide (GO) is the most studied functionalized carbon materials as sulfur hosts showed great improvement in cycling performance viz only 0.039% fade in the capacity over 1500 cycles[63]. Metal oxides are intrinsically polar in nature and thus n further surface modification is required. $Mg_{0.6}Ni_{0.4}O$ and Al_2O_3 nanoparticles within a size regime of ~50 nm was used as adsorbent additives in carbon/sulfur composites and the coulombic efficiency, initial discharge capacity, and cycling stability were found to be improved[64]. Xiao et al demonstrate the use of hybrid TiO_2/graphene interlayer between the sulfur cathode and the separator, serve as a polysulfide reservoir layer where TiO_2 nanoparticles can chemically bind the

dissolved polysulfides.[65] The mesoporous silica SBA-15 with high surface area (850 m2 g-1) and large pore volume (1.2 cm^3g^{-1}) when added as an additive into carbon/sulfur composite, initial discharge capacity and cycling stability was enhanced due to the polysulfide absorption into the silica pores suppressing their diffusion into the electrolyte[66].

(iii) Non solvent electrolytes to suppress the solubility of polysulfides

There are many studies conducted to overcome the LiPS dissolution/ shuttle problem with the development of novel electrolytes with suppressed LiPS solubility. The dissolution of LiPS depends on the solvation of Li+ cations and the counter anions. Electrolyte with lower electron donor ability are less likely to solvate Li+ ions and thus can suppress the LiPS solubility when compared to conventional dilute ether-based electrolytes. Amide-based room temperature ionic liquids (RTILs) comes under the few reported “nonsolvent” electrolytes and solvates of Li salts, lithium bis(trifluoromethane) sulfonimide (LiTFSI), in conventional solvent systems. A recent study on an electrolyte (ACN)2-LiTFSI complex which contain two moles of acetonitrile (ACN) molecules are coordinated to one mole of Li+ cations form counter ion pairs with TFSI- anions suppress the electrolyte reaction with lithium metal and have extremely low LiPS solubility[67].

1.7.2 strategies towards Li dendrite suppression:

Since the 1960s, these above-mentioned approaches to suppress dendrite growth can be classified into the following categories.

(i) *In situ* stable SEI film

Solid electrolyte interface is the ionically conducting layer formed through the reaction between the metal and non-aqueous electrolyte, which comes about in a range of ~2nm thickness. During the charge process, due to the formation of dendritic Li, the surface area of the exposed Li

will be increased, and newly formed fresh Li will get exposed to the electrolyte which ends up in repeated SEI formation. Repeated SEI formation consumes more Li from the electrolyte and leads to the drying up of electrolyte. This will influence the cell resistance and coulombic efficiency adversely. For a limited dendrite growth, ideal SEI should be formed which is highly ionic conductive, dense, thinner and with a high elastic strength. To acquire these, we need to play with the organic solvents, Li salts and functional additives, which is practically far in application to the existing systems [68].

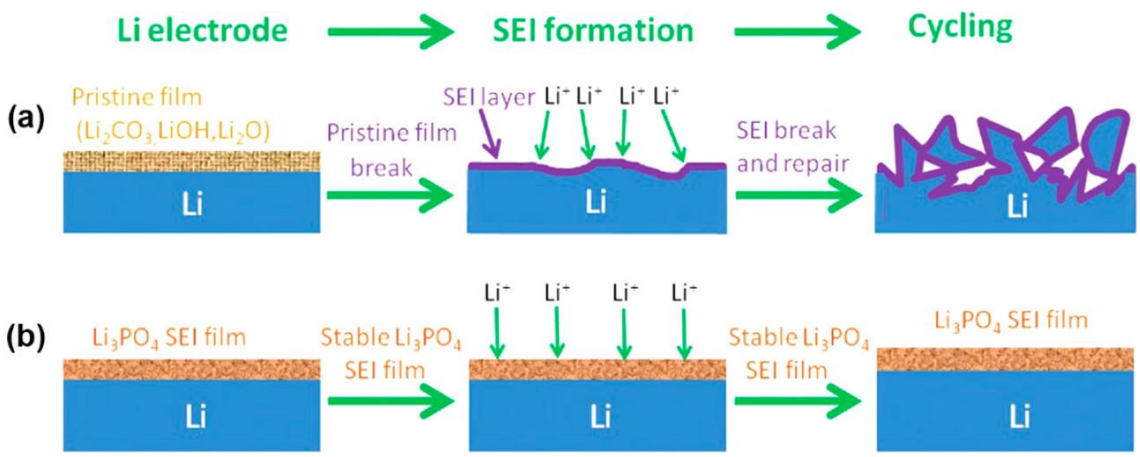

Figure 1.8 Scheme of Li metal anode with and without chemical pretreatment[69].

(ii) Ex situ formed surface coating

Choosing appropriate chemicals, we can treat the Li metal will end up in a stable protective layer. During Li deposition or stripping, Li can be plated beneath these protecting layers hindering the growth of dendrites. This layer will prevent the reaction between Li metal and non-aqueous electrolyte which causes the dendrite formation, thus stabilizing the SEI formation. However, these layers will get destroyed during cycling process which results in broken SEI, non-uniformity in SEI and thus accelerates the dendrite formation[70]. Amorphous hollow carbon spheres are deposited onto the Li metal anode using flash evaporation technique which had a high Young's

modulus. The carbon coating has a proper strong adhesion to the current collector which moves up and down to accommodate the Li ions which were plated or stripped on them. These methods helped to enhance the columbic efficiency by 99% for more than 150 cycles. But still the repeated cycling results in the breakdown of these protective making a rough SEI exposed to the liquid electrolyte which accelerates the dendrite formation sue to the non-uniform Li metal anode surface[71].

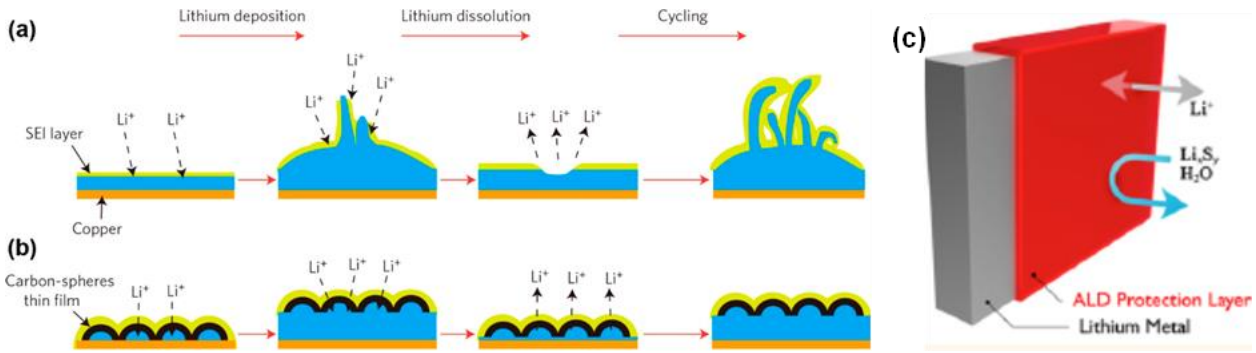

Figure 1.9 schematic illustration of depositing physical coating a. without coating,[71] b. with carbon nano spheres and c. ALD of Al_2O_3[72].

(iii) Solid state polymer electrolyte

Solid state electrolytes have high modulus can effectively relieve the safety issues through suppressing the Li dendrite growth. Dendrite suppression can be achieved if the shear modulus of the electrolyte is twice higher than that of Li metal anode which is around 10(^9) Pa. The solid electrolytes have higher mechanical strength which is good enough to suppress the dendritic protrusions[73]. Polymer electrolytes including poly ethylene oxide (PEO) will not go for any interfacial reaction with Li and they are thermodynamically very stable with Li at higher temperature. The gel electrolyte based on PEO, Poly (propylene oxide) (PPO), Poly (ethylene glycol) (PEG), Poly (acrylonitrile) (PAN) etc. The mechanical mixing of polymers with filler inorganic nanoparticles is most convenient method to improve the ionic conductivity, structural

stability and anode surface contact. There are many studies including incorporation of ceramic filler particles like SiO2, with varying particle size of the inorganic fillers towards a better composite polymer electrolyte. The combination of ceramic fillers and polymer electrolytes can construct excellent electrolytes with high ionic conductivity and good mechanical properties. A 3D polymer ionic conducting network with ceramic fillers were introduced through electrospinning method for mechanically suppress the dendrite formation and to eliminate the intrinsic SEI formation. However, some of the polymer-based electrolytes including PEO based showed a significant reduction in their mechanical strength when the temperature is increased. Thus, solid state electrolyte is having low room temperature conductivity i.e. in the range of 10^{-8} to 10^{-5} cm^{-1}[74].

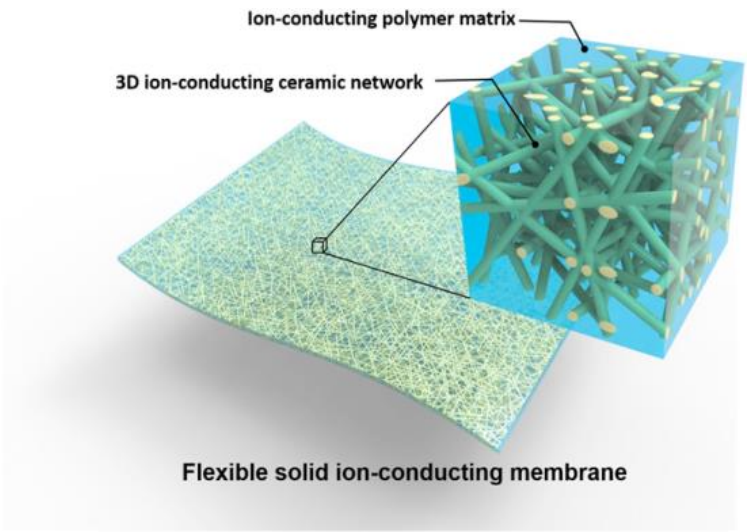

Figure 1.10 hybrid solid state composite electrolyte[74].

(iv) Structured anode

The main issue with the Lithium Metal Batteries (LMBs) is the volume change. Li metal anode will undergo infinite volume change during the Li plating / stripping process resulting in

the reduction in the columbic efficiency, poor stability of the formed SEI, and finally the poor life span of the batteries. So, with a proper matrix to accommodate the Li plating / stripping will help to significantly mitigate the infinite volume change along with regulating the Li stripping/ plating process towards suppressing Li dendrite growth[75].

Placing glass fibers with polar functional groups on the Li metal anode surface can distribute the Li ions uniformly. The binding energy between the glass fiber and Li ions is higher than that between the Cu foil and Li ions, which facilitates more adsorption of Li ions compensating the interaction between the Li ions and protuberance of Cu foil or the previously grown dendritic peaks. This method prevents the accumulation of Li ions which results in the dendrite growth inhibition[76].

But it is very difficult to do the selection of lithophilic matrix and their ratio in the composite anode which limit this method from practical applications.

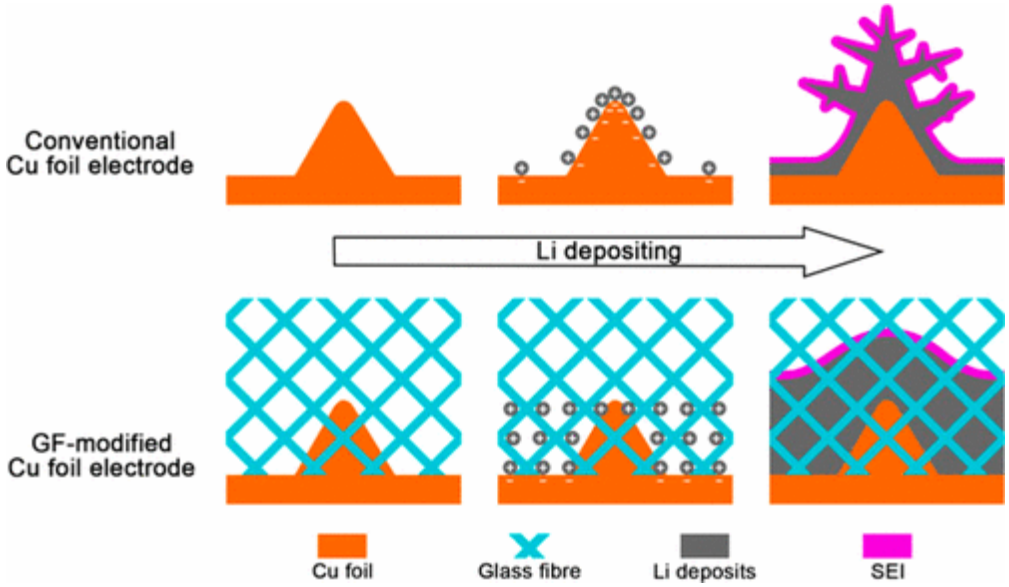

Figure 1.11 Controlled Li deposition in presence of polar fiber membrane[76].

1.8 Scope of the study

We believe that suppression of dendrite formation and reducing the shuttle effect are the key issues to realize the full potential of commercial Li-S battery. The optimization and designing of high capacity electrode materials is also a crucial issue to make the Li-S batteries suitable for the future requirements. These issues can be addressed only when we have a better mechanistic understanding about chemical and electrochemical processes happening in the battery. Several strategies have been developed to do so by several research groups around the world. Recently, our group demonstrated utilization of electrocatalyst to improve the polysulfides reaction and trap the polysulfides inside the cathode of Li−S battery[28, 29, 77].The electrocatalyst not only reduce the energy barrier of electrochemical reaction but also act as an anchor for polysulfides and confide them to cathode and reduce the shuttle effect. The fundamental understanding about electrocatalytic reaction such as redox kinetics, adsorption process of electroactive materials over the electrocatalyst are essential to design appropriate electrode materials Li−S battery. Moreover, It is well-known that Li metal is highly unstable in traditional organic liquid or polymer gel electrolyte systems due to the formation of Li dendrites at the electrode/electrolyte interface. Over multiple charge and discharge cycles the formation of dendrites at the interface results in: reduced Li availability for the electrochemical reactions, disruption in Li transport through the interface and increased safety concerns due to short circuiting. There is an urgent need to attain a profound mechanistical understanding on how the interfacial chemistry and Li deposition is correlated, how anode overpotential affect the cell characteristics etc. Our research will explore the use of a special class of ionic liquids (ILs) with liquid crystal properties for the electrolyte of Li metal batteries.

The research combines experimental development and characterization of the ILCs and analysis of their potential as electrolyte for improving Li battery performance.

The objectives of this thesis work is addressing two of the major research issue 1) shuttle effect and 2) dendrite growth, fill the knowledge gap thus enabling the mechanistic understanding of electrode/electrolyte interface to design the target specific materials for Li-S batteries. To address the shuttle effect, we considered an electrocatalytic driven approach for polysulfide adsorption onto cathode surface. The fundamental understanding of this electrocatalysis sulfur cathode is still lacking. We believe that, surface area and effect of conductivity of the electrocatalyst have pivotal role unfortunately which are least researched areas. The research on these areas can open a great demand to explore the novel concept of electrocatalysis driven Li-S battery chemistry. We hypothesize that the major problem called polysulfide shuttle effect can be addressed and thus improved electrochemical performance can be achieved through embedding electrocatalyst with highly conductive and high surface area host materials. Second issues that we are addresses in the thesis is lithium dendrite formation mechanism. Though the dendrite formation is one of the oldest issues, fundamental understanding about how the interfacial chemistry and Li deposition is correlated, how anode overpotential affect the cell characteristics etc are still have no answers which are essential to address the dendrite formation. Here we explore the use of a special class of ionic liquids (ILs) with liquid crystal properties as electrolyte of Li metal batteries which can also suppress the dendrite formation. The research combines experimental development and characterization of the Ionic liquid crystals (ILCs) and analysis of their potential as electrolyte for improving Li battery performance.

CHAPTER 2 EXPERIMENTAL METHODS

2.1 Material Characterization Techniques for Electrocatalysts

2.1.1 X-ray diffraction spectrometer

X-ray diffraction (XRD) is a non-destructive analytical tool for the characterization of crystal structure, chemical composition, and physical properties of materials. This technique is based on elastic scattering of X-rays with high energy electromagnetic radiation having energies ranging from about 200 eV to 1 MeV. XRD can also be used to determine the crystalline size and orientation of powder samples. XRD works based on Bragg's diffraction model. When electromagnetic radiation with wavelength comparable to the atomic spacing incident on a crystalline sample, the waves are scattered by the successive planes of atoms and will undergo constructive interference and thus form a diffraction pattern. The waves are scattered by lattice planes, which are separated by interplanar distance "d". The path difference between waves undergoing constructive interference gives a mathematical relationship, which is called Bragg's equation and can be written as: $n\lambda = 2d\sin\theta$,

$n \rightarrow$ integer determining order
$\lambda \rightarrow$ wavelength
$d \rightarrow$ spacing between planes in atomic lattice.
$\theta \rightarrow$ angle between incident ray and scattered planes.

This is Bragg's law which describes the condition for constructive interference from successive crystallographic planes (hkl) of the crystalline lattice.

X-ray unit used in the present study is a fully automated Bruker AXS, D8 Discover diffractometer using monochromatic CuKα radiation of λ=1.5418Ao as a source at an energy of 8.04 KeV. The finely powdered sample is spread on a flat non-diffracting glass slide and then

exposed to X-ray beam. The automatic arrangement was set on for the desired scanning speed and the spectrum was recorded for 2θ values from 0º to 90º. From the maximum of recorded diffractograms, lattice parameter (a) and crystallite size can be acquired. Lattice parameter was determined assuming cubic symmetry and planes were identified by matching with standard values of International Centre for Diffraction Data (ICDD).

2.1.2 Scanning Electron Microscopy (SEM)

The scanning electron microscope (SEM) is used to detect the low kinetic energy secondary electrons from solid surfaces. When an electron beam interacts with a solid, various types of processes including electron scattering and excitation occurs, which produces (1) secondary electrons, (2) backscattered electrons, (3) Auger electrons, (4) x-rays, (5) photons of various energies. The fraction of energy deposited by an electron beam associated with different processes is dependent on the sample. The secondary electrons are produced by the primary electron beam as it enters a sample, and typically, they have kinetic energies < 50 eV, which are sensitive enough to the differences in surface topology. Such secondary electrons form the basis of SEM. All the produced signals are detected to reveal the information about the sample's surface morphology[70]. The electron beam is scanned, and the beam's position is combined with the detected signal to produce an image of the sample surface. Generally, SEM can obtain images of resolution up to 1 nanometer. In the present studies, surface morphology analysis was performed using JSM 7600 FE SEM.

2.1.3 Transmission Electron Microscopy (TEM)

TEM is a microscopic technique where the electron beam is transmitted through an ultra-thin specimen, and an image is formed from the interaction of the electrons with the specimen.

The as formed image is magnified and focused onto an imaging device, such as a fluorescent screen or to be detected by a sensor such as a CCD camera. A TEM is composed of several components, which include an electron emission source for the generation of the electron stream, a vacuum system through which the electrons travels, a series of electromagnetic lenses, as well as electrostatic plates. The latter two will allow the operator to guide and manipulate the beam as required. Imaging devices are then used to create an image from the electrons that exit the system. TEM images of samples in this present study was carried out with a JEOL-3010 instrument.

2.1.4 Optical Absorption Spectroscopy

Ultraviolet-visible spectroscopy (UV-Vis) is the analytical technique that can detect nearly every molecule. Here, the UV-Vis light is passed through a sample and the transmittance of light by the sample is measured. From the transmittance (T), the absorbance can be calculated as A=-log (T) and the absorbance spectrum obtained shows the absorbance of a compound at different wavelengths. The amount of absorbance at any wavelength depends on the chemical structure of the molecule. In the work presented in this thesis, UV-Vis absorption spectroscopy has been used to monitor adsorption behavior of polysulfides onto the catalyst surface and the absorption spectra were obtained using Shimadzu UV-3600 UV- Vis- NIR spectrophotometer.

2.1.5 X-ray Photoemission Spectroscopy (XPS)

XPS is a highly surface sensitive analytical technique used to study the composition and electronic state of the surface region of a sample. XPS is based on the principle called photoelectric effect and photoelectron spectroscopy uses monochromatic source of radiation. In XPS, the photon of energy is absorbed by an atom in a solid, leadsto ionization atom and emission of the core electron. The kinetic energy distribution of the emitted photoelectrons is calculated, and

corresponding photoelectron spectrum is obtained. In this work, XPS of electrode surfaces were collected using a PHI Quantera spectrophotometer and deconvolution of spectra was carried out with open source XPS peak fit 4.1 software.

2.1.6 Thermal studies

Thermo gravimetric analysis (TGA) is a technique to determine the change in weight of a sample in relation to change in temperature. It is commonly used to identify the characteristics of different materials, their degradation temperatures, absorbed moisture content, level of inorganic and organic components, decomposition points etc. It involves the change in weight of a system as the temperature gets increased, preferably at a linear rate. Thermal events like melting, crystallisation does not affect the weight of the sample. But some events like desorption, sublimation, oxidation, reduction, vaporisation etc. can bring change in the weight of the sample. This technique can be used to to analyse the sample where volatile and gaseous products lost during a reaction. A high precision balance with a pan having sample is placed in a small electrically heated space with a thermocouple attached to measure the temperature. The atmosphere is purged with inert gas to prevent oxidation or other similar reactions. TGA studies in the present study were carried out using TA Instruments TGA Q500 in the temperature range from ambient to 900 ^{o}C at a heating rate of 10 ^{o}C per minute.

2.1.7 Raman spectroscopy

Raman spectroscopy is a vibrational spectroscopic method based on the inelastic scattering of a monochromatic excitation source. It is a powerful tool to examine the fine structure, atomic bonds, and mechanical of materials. When the sample is irradiated with a monochromatic source, most of the radiation is elastically scattered (Rayleigh scattering) whereas a small portion is in

elastically scattered (Raman scattering). Raman spectrum of a molecule consists of stokes and anti-stokes lines. When the molecule excited to higher unstable vibrational state returns to a different one other than its original vibrational state, stokes lines are obtained.if the molecule initially in the first excited vibrational state is excited to higher unstable vibrational state and returns to ground state, then anti-stokes lines are generated. Stokes lines are those lines whose wavelengths are longer than that of the incident light, whereas anti-stokes lines are those with wavelengths shorter than the incident line. Raman studies were carried on Andor 500 series spectrometer with 532-nm green laser excitation.

2.2 Characterization of Ionic Liquid Crystal (ILC) electrolytes

All the combinations of ILC electrolytes with varying concentrations of additives will be studied for their ionic conductivity and anisotropic nature using conductivity and DSC analysis. Electrochemical impedance spectroscopy (EIS) studies will help us to elucidate SEI nature and stability. NMR is conducted to understand the fundamental interactions between additives and the salt/solvent of the electrolyte. Further, wide-angle X-ray diffraction (WAXD), small angle X-ray scattering (SAXS) and polarizing optical microscopy (PLM) studies are used to determine the crystal data and orientation of additive containing ILC electrolytes.

2.2.1 Nuclear Magnetic Resonance spectroscopy

The Nuclear Magnetic Resonance spectroscopy (NMR) is a technique based on the absorption of electromagnetic radiation in the radiofrequency region by the nuclei of atoms. Certain elements possess random nuclear spin, which generates a magnetic field. But in the presence of an external magnetic field, nuclei align themselves either with or against it. The external magnetic field creates energy transfer between the ground state and excited state at a

wavelength that corresponds to radiofrequency. Hence, when the spin comes back to the ground state, the absorbed radiofrequency energy is emitted at the same frequency level, which gives the NMR spectra of concerned nuclei. That is NMR occurs when nuclei aligned with an applied field are induced to absorb energy and change their spin orientation with respect to the applied field. It is used to determine the content, molecular structure and purity of a sample.

2.2.2 Fourier transform infrared spectrometer

Fourier transform infrared spectrometer (FT-IR) is another vibrational spectroscopic technique to which is widly used to identify the functional groups. the technique uses mid and near IR frequencies. When IR radiation is passed through a sample, some radiation is transmitted, and some absorbed by the sample. The Fourier transform converts the detector output to an interpretable spectrum that have the patterns that provide structural insights. Here FT-IR analysis was carried out using Varian/Digilab Excalibur 3100 High Resolution FT-IR with NIR.

2.2.3 Differential Scanning Calorimetry

The Differential Scanning Calorimetry (DSC) is a type of thermal analysis in which the energy required to establish a zero-temperature difference between sample and reference material is measured as a function of temperature. The instrument is used to study the thermal stability of a material and to identify the structural transitions. In endothermic reactions, (such as melting, vaporisation, boiling) more energy is needed to maintain a zero-temperature difference between a sample and reference material where as in exothermic reactions, (such as crystallization) only less energy is needed. DSC can also be used to measure heat capacities of condensed phases, which makes it is an inexpensive and rapid analyzing tool for characterizing liquid crystal mesophases. It provides in depth information on the phase transitions that a molecule undergoes when it is

heated or cooled, such as transition temperatures and enthalpies. Thus, the kind of liquid crystalline phase can be identified from this enthalpy, i.e. higher the enthalpy, higher the intermolecular interactions in highly ordered LC phase. Here DSC analysis was carried out using TA Q20 where the sample is heated and cooled from -20 to 200 ^{o}C.

2.2.4 Polarized light microscopy

Polarized light microscopy (PLM) is the standard tool that uses the principle of the polarization of light to identify the phases and phase transitions of LCs. The anisotropy nature of LCs causes the light polarized along the director to travel with a different velocity than the one perpendicular to the director. Thus, LC will look bright under crossed polarizers.

2.2.5 Wide-angle X-ray diffraction (WAXD) and Small Angle X-ray Scattering (SAXS)

WAXD will help in identifying the mesophases, determining the LC phase structure, explains the presence of long range ordered molecules. SAXS can be helpful to analyze the phase transitions, smectic ordering of a liquid crystal, or to detect defects in the structure. This method uses the elastic scattering of X-rays at angles between zero to 10 degrees, gives information about the low orientational and high translational order of compounds.

2.2.6 Anisotropy conductivity measurement

Anisotropic ionic conductivity can be measured in both directions parallel and perpendicular to the self-assembled layers using alternating current impedance technique. Anisotropy in ionic conductivity of ILCs is analyzed by a pair of comb-shaped gold electrodes (Cell A) and a pair of Indium tin oxide(ITO) plates (Cell B).The experimental setup was shown in the figure 2.1. Firstly, gold was sputtered onto a glass plate in comb shape by leaving a 1mm distance between the teeth, and their sidewise width was nearly 0.3mm. The thickness of the

sputtered gold was about 0.8 µm. The compound mixtures were filled in both the cells, and their orientation is confirmed by a polarizing microscope. Ionic conductivity parallel to the oriented layer is measured using cell A and the one perpendicular to the oriented layer can be obtained by using cell B. In Cell B, a pair of indium tin oxide (ITO) electrodes were separated with a thickness of 30 µm using a Teflon spacer. In both cases, the homeotropic alignment of sample mixtures can be observed.

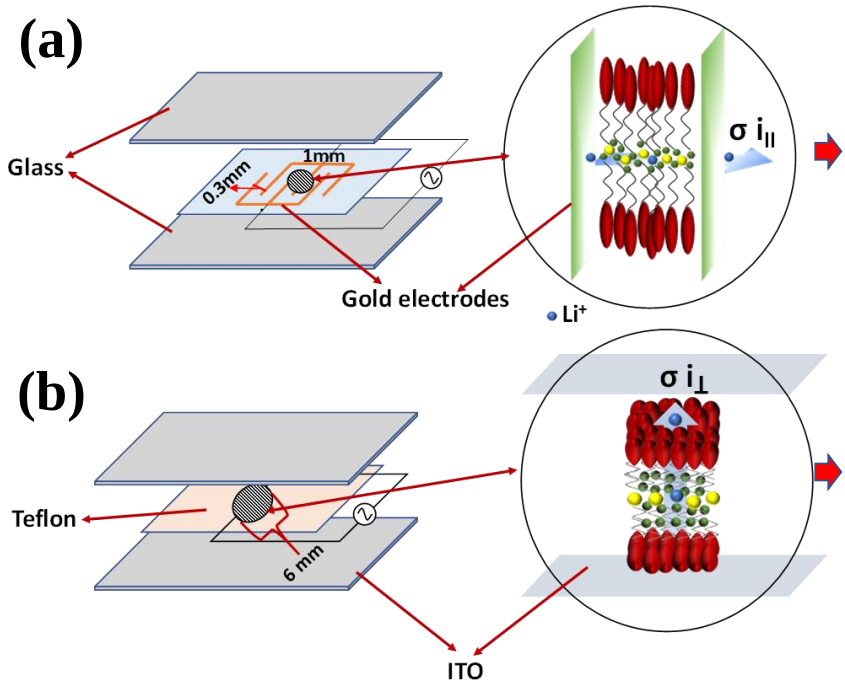

Figure 2. 1 Experimental set up to measure anisotropy

2.3 Electrochemical Testing

2.3.1. Cyclic voltammetry

Cyclic voltammetry (CV) is an electrochemical technique used for acquiring information of both kinetics and thermodynamics details of electron transfer at the electrode/electrolyte interfaces. CV involves sweeping the electrode potential between two preset values at a known sweep rate. Basically, the potential of the working electrode is swept from the initial potential (E_i)

till switching potential (E_s) where an electrode process occurs, where direction of the scan is reversed and swept back to final potential (E_f). The choice of potential window depends on the stability range of the electrolyte.

2.3.2. Electrochemical impedance spectroscopy (EIS)

Electrochemical impedance spectroscopy (EIS) is the technique used to investigate the electrical properties of materials and interfaces of electrochemical systems. EIS measurements involve the perturbation of the electrochemical system by applying a low amplitude ac signal, and the response can differ in phase and amplitude from the applied signal. Measurement of phase difference and amplitude allows the analysis of the electrochemical process undergone by the electrode in relation to contribution from diffusion, kinetics, double layer, etc. There are various applications with EIS studies in membranes, ionic solids, solid state electrolytes, conducting polymers and liquid/liquid interfaces. The EIS data is represented in complex plane plots as $-Z''$ vs. Z', normally called Nyquist diagrams. Lithium-ion conductivity is an important feature of a component expected to be used as an active material within a lithium-ion battery. To examine the ionic conductivity through battery materials, EIS represents a fast, easy, and standardized technique. The impedance is the resistance encountered when current flow through a circuit composed of resistors, capacitors, or inductors or any other combination of these. The cell was excited with 5 mV AC signal and impedance was calculated in the frequency range from 100 kHz to 10 mHz at open circuit potential using Biologic EC-lab impedance analyzer.

2.3.3 Chronoamperometry

Chronoamperometry (CA) is an electrochemical technique used to study the kinetics of chemical reactions, diffusion processes, and adsorption. Here, a potential step is applied to

the electrode and the subsequent current vs. time is obtained. CA measurement gives additional qualitative and quantitative information about the electrolyte composition, speed of electrode processes and the chemical reaction that occurs at the electrodes and in the electrolyte. Chronoamperometric curves should be recorded at potential higher than the overpotential value.

2.3.4 Tafel plot

Tafel plot is widely used in electrochemistry to estimate the catalytic reaction parameters by plotting logarithm current density *vs* potential(see Figure 2.2). The coefficient of charge transfer can be obtained from the slope of the linear region, which is related to the catalytic activity of the material. Exchange current density (i_0), related to the reaction kinetics, can be determined from the Tafel plot by extrapolating the current density in the linear region. A high exchange current density value signifies the smaller activation barrier, which requires a small over potential. The rate of an electrochemical reaction to the overpotential can be obtained by the mathematical equation:

$$\eta = A\ X \ln (i/i_o)$$

Where:

η is the overpotential, V

A is the so-called "Tafel slope", V

i is the current density, A/m^2

i_o is the so-called "exchange current density", A/m^2

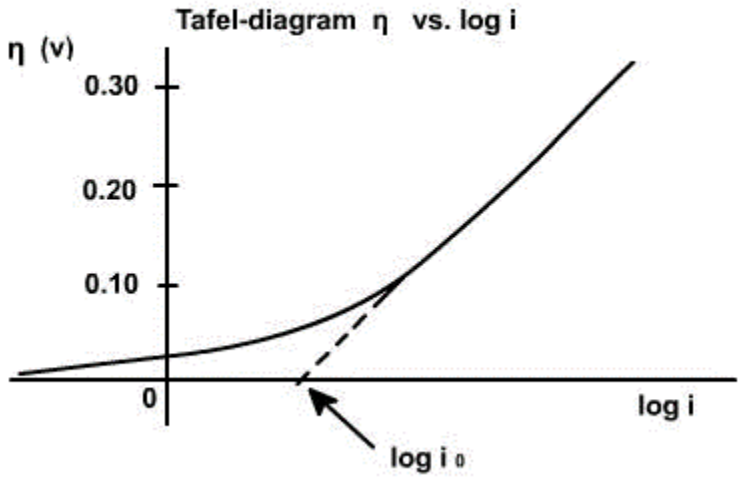

Figure 2.2 Tafel plot: Electrochemical potential vs the logarithm of exchange current density.

CHAPTER 3 UNDERSTANDING HETEROGENEOUS ELECTROCATALYSIS OF LITHIUM POLYSULFIDE REDOX ON Pt AND WS_2 SURFACES

3.1 Background and Motivation

Regardless of gaining high energies with Li-S batteries, technology is hampered by several challenges which are already discussed in previous chapters such as structural & volumetric changes, poor rechargeability due to the formation of insulating discharge end products (Li_2S_2/Li_2S), polysulfide (PS) shuttling effect, dissolution of soluble higher order polysulfides Li_2S_x ($4 < x < 8$) into the electrolyte during prolonged cycles, severe capacity decay, low coulombic efficiency and limited cyclic life. Significant progress has been made towards mitigating the above mentioned issues through developing efficient electrolytes[78-80], novel cell configurations[81, 82], efficient separators[83, 84], cathode sulfur host materials[62, 85, 86] and anode protective coatings[87, 88] etc. Cathode surface modification has been considered and explored as an efficient approach among the strategies undertaken for soluble PS encapsulation. In this scenario, porous carbon-sulfur cathode designs provide effective electronic conduction, better soluble PS absorption and shuttling effect minimization [89-93]. However, intrinsic issues such as physical confinement of PS and pore blockage due to the deposition of insoluble products (Li_2S_2/Li_2S) fetch severe capacity fade. The functionalization of cathode surfaces has been considered as an effective approach for efficient retention of polysulfides through developing strong covalent linkages[86, 94-96]. Despite remarkable success of these strategies, low surface area with minimal areal sulfur loading and low electronic conductivity diminishes the Li-S cell performance.

Accelerating the polysulfide redox reaction kinetics on the cathode surface was appeared to be a viable approach along with the proven sorption method to seize the shuttling effects. Highly conductive metallic oxides and hybrid host surfaces can trigger the reduction of adsorbed

intermediate soluble PS to solid product Li_2S and permit their controlled deposition[92, 97]. In addition, the inclusion of sulfiphilic CoS_2 promotes the PS adsorption onto the surface and significantly manipulates redox activity of liquid-liquid PS conversion resulting in prompt deposition of solid Li_2S[52]. This finding imparts the role of conductive surface in the formation of solid end products during cycling and how it controls the Li-S redox reaction kinetics. However, the conductive surface effect on mass transport and electron transfer rate involved in redox reactions are not properly studied yet. Recently, our group has reported a new avenue explaining the electrocatalysis of polysulfide reaction in Li-sulfur by using conventional conductive catalytic surfaces such as Pt or Ni coated Al foil/high surface area matrix *viz.* graphene[77, 98]. Electrocatalyst having 3D porous structures can minimize the mass transport problems with a great improvement in rate capability. The use of an electrocatalyst in the multistep sulfur redox process has shown great potential in (i) trapping of polysulfides (ii) reducing the polarization (iii) enhancing the specific capacity with long cycle life and (iv) exhibiting excellent reversibility. However, the involvement of an electrocatalyst in each single step and their influence on the rate of reaction is remaining unexplored.

Despite having a massive number of reports on the Li-S chemistry, mechanistic features of sulfur redox reaction and its kinetics are still unclear[99-104]. It is elucidated that overall sulfur redox reaction involves a multielectron process proceeding *via* formation/dissociation of many intermediate polysulfides (Li_2S_x, x = 2-8) through (electro) chemical/disproportionation reaction at the cathode regime[105, 106]. It is essential to have a fundamental understanding of the surface effect on Li-sulfur redox reaction kinetics which holds the key for advancing in the design of pioneering cathode surfaces. In this context, here we evaluate the kinetics of sulfur redox chemistry on different electrocatalytic surfaces (Platinum and WS_2) and their influences on reaction kinetics

at different stages. To deduce the accurate diffusion and steady state kinetic parameters, we carried out the three-electrode cyclic voltammetry with the advantage of maintaining a constant working electrode potential. Potentiostatic experiments are performed to understand the surface dependent PS adsorption, reaction kinetics and cell reversibility.

3.2 Experimental Methods

3.2.1 Preparation of lithium polysulfides (LiPS) (Li_2S_4 and Li_2S_8): Stock solutions of LiPS (0.6M) have been prepared with calculated stoichiometric amounts of Li_2S and Sulfur in Tetraethelenglycol dimethyl ether (TEGDME) solvent and were heated at 90° C for 12hrs. For electrochemical studies, we used a 2 mM Li_2S_8 solution with 1 M of lithium bis(trifluoromethanesulfonyl) imide (LiTFSi) and 1 M of lithium nitrate ($LiNO_3$) mixture as supporting electrolyte. All the polysulfides solutions were prepared inside the Ar filled glove box having oxygen and moisture level below 0.1ppm. For LiPS adsorption studies, 10 mM of lithium polysulfide (Li_2S_4) solution was used.

3.2.2 Adsorption studies: In a typical process, 1 mg of carbon, Pt and WS_2 samples were dispersed individually in TEGDME/ 10 $mmolL^{-1}$ Li_2S_4 solution mixture inside Argon filled glove box. Solution mixtures were kept aside overnight to discern the color changes and then, the supernatant solution was separated through centrifugation at 5000 rpm for 30 min. Finally, these samples were used for ultraviolet-visible spectroscopy (UV-Vis) adsorption characterization.

3.2.3 Electrochemical studies (potentiodynamic): Three electrode cyclic voltammetric experiments were performed to evaluate the catalytic surface effect involved in LiPS redox reactions. The electrochemical cell was consisting of bare glassy carbon, Pt and WS_2 (40 $\mu g/cm^2$ each) coated glassy carbon (GC) as working electrode, lithium foil as counter/reference electrodes and 2 mM Li_2S_8 solution as catholyte dissolved in TEGDME containing 1M LiTFSi + 1M $LiNO_3$

mixture. Cyclic voltammetry studies were conducted using CH 760E bipotentiostat in the potential window of 3.0 -1.5 V at a scan rate of 0.1 mV/s and the scan rate studies were carried out in the range of 10 to 100 mV/sec.

3.2.4 Chronocoulometric method: To obtain adsorption parameters, individual coin cells were first discharged galvanostatically at the current rate of C/20 till 2.1 V and interval time of 1 minute was allowed for equilibration. After discharge, a potential of 2.1V was constantly applied for about 600 seconds and resultant transient plot Q *vs* t was used for analysis.

3.2.5 Li_2S Nucleation studies: Carbon, Pt and WS_2 coin cells were first discharged galvanostatically at 0.04 mA until 2.02 V to reduce all the higher order polysulfides. Then, the analysis turned to potentiostatic mode after maintaining a potential of 2.05 V for 10 hrs. to measure the kinetics involved in Li_2S formation.

3.2.6 Electrochemical Impedance: Charge transfer measurements of Carbon, Pt and WS_2 coin cells against LiPS redox reaction were performed using Biologic EC-lab impedance analyzer. Nyquist impedance spectra were recorded potentiostatically at different discharge/charge potential in the range of 3.2 to 1.5 V with 15 minutes interval between each measurement. Prior to this, cells were subjected to galvanostatic discharge/charge process till the corresponding potentials to confirm the cathode surface has undergone different polysulfide redox reactions. AC frequency between 1 MHz to 1 mHz with an amplitude of 10 mV was employed for impedance measurements.

3.2.7 Coin Cell fabrication and electrochemical measurements (potentiostatic): coin cell electrodes were prepared by mixing an appropriate mixing of bulk WS_2 or Pt individually with conductive carbon (Super-P) and polyvinylidene fluoride (PVDF) binder in the weight ratio of 80: 10: 10. The mixture was ground well with *N*-methyl-2-pyrrolidone (NMP) as a solvent, until a

mirror-polished thick slurry is obtained and then it is coated uniformly with a thickness of 40µm on thin aluminum foil using doctor blade film coater. The electrode coated Al foil was dried overnight in a vacuum oven at 90 °C to evaporate the solvent and is cut into circular discs of having 12.7 mm dia. Standard 2032 coin cells were fabricated using individual coated materials as working electrode, lithium metal as both counter cum reference electrode and celgard membrane as a separator. Here, pre-calculated amount of 200 mM catholyte containing 0.00029 mg of sulfur was used as active material along with the electrolyte consisting of 1 M of LiTFSi and 1 M $LiNO_3$ in TEGDME.

3.3 Results and discussion

3.3.1 Electrocatalysis in LiPS reduction

In this work, we have systematically examined the electrocatalysis of LiPS redox activity on different surfaces like Platinum (Pt), Tungsten disulfide (WS_2) and Carbon using cyclic voltammetry (CV). As shown in figure 3.1a, Li_2S_8 undergoes similar CV features at all the surfaces and have three distinct redox process as marked I, II, III and are discussed in detail as following: First redox corresponds to the reduction of S_8 /S_8^{2-} proceeding via $2e^-$ and follows a similar trend on all the surfaces, their corresponding CV parameters such as peak potentials (E_{pa}, E_{pc}), (anodic peak (pa) and cathodic peak (pc)) peak current densities (I_{pa}/I_{pc}), peak separations (ΔE_p), are listed in Table 3.1. However, the peak potential (E_{pc1}) was found to be anodically favored and an increment in the current (i_{pc1}) was observed on Pt and WS_2 when compared to carbon. The peak positioning for carbon was found at 2.43 V which got anodically shifted to 2.46 and 2.47 V for Pt and WS_2 respectively. Moreover, the potential difference between the anodic and cathodic peak ($\Delta E_p = Ep_a - Ep_c$), found to be decreased from 110 mV (carbon) to 70 mV (Pt) and got further lowered on WS_2 surface (30mV). This result implies the dependence of Li_2S_8 redox activity on the

nature of the surface and confirms the surface involved electrocatalysis mechanism. In fact, lowering the overpotential of LiPS redox is the best strategic way to minimize cell polarization and increase the rate capability with long cycle life.

Surface	E_{pc}, E_{pa}, V	ΔE_p, mV	i_{pc}, i_{pa}, µA
Carbon	2.43, 2.54	110	-0.30, 0.67
Platinum	2.46, 2.53	70	-0.40, 0.78
WS_2	2.47, 2.50	30	-0.36, 0.72

Table 3.1. Comparison of LiPS reduction (E_{pc})-oxidation (E_{pa}) potential, Redox peak potential difference (ΔE_p) and current (I_{pc}, I_{pa}) on different surfaces

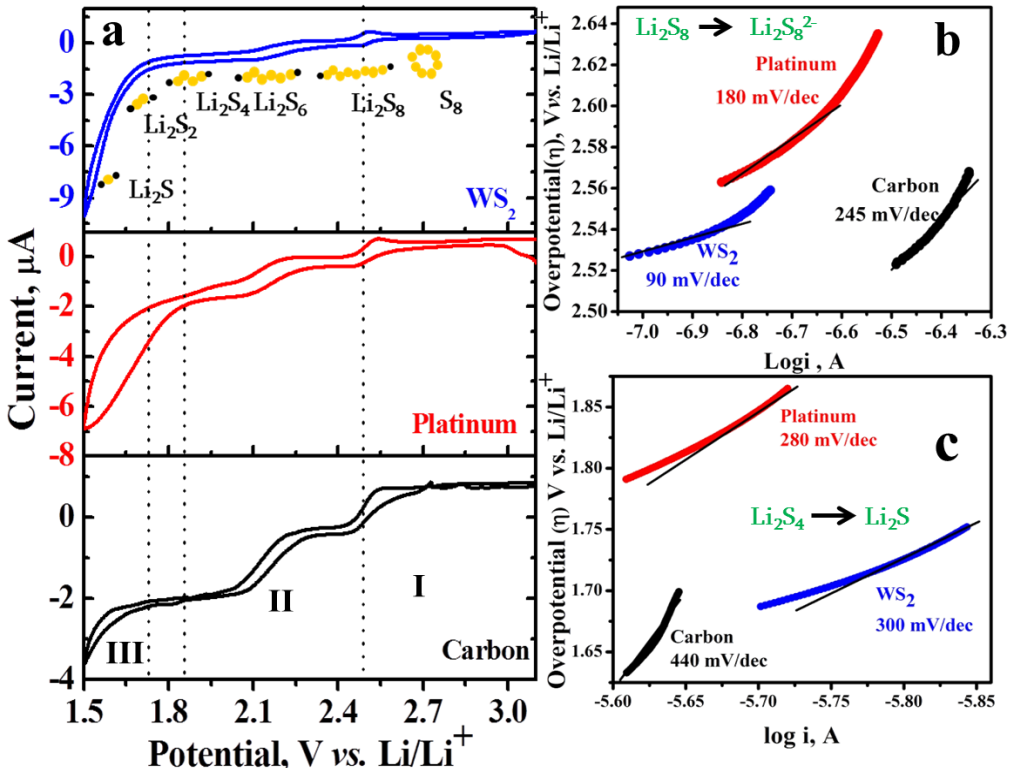

Figure 3.1. Evaluation of electrocatalytic activity**:** (a) Cyclic voltammogram of carbon, Pt and WS_2 modified electrode and their corresponding Tafel plot for (b) ~2.6 V Li_2S_8 (reduction peak) and (c) ~1.9 V (reduction peak). Scan rate: 0.1mV/sec.

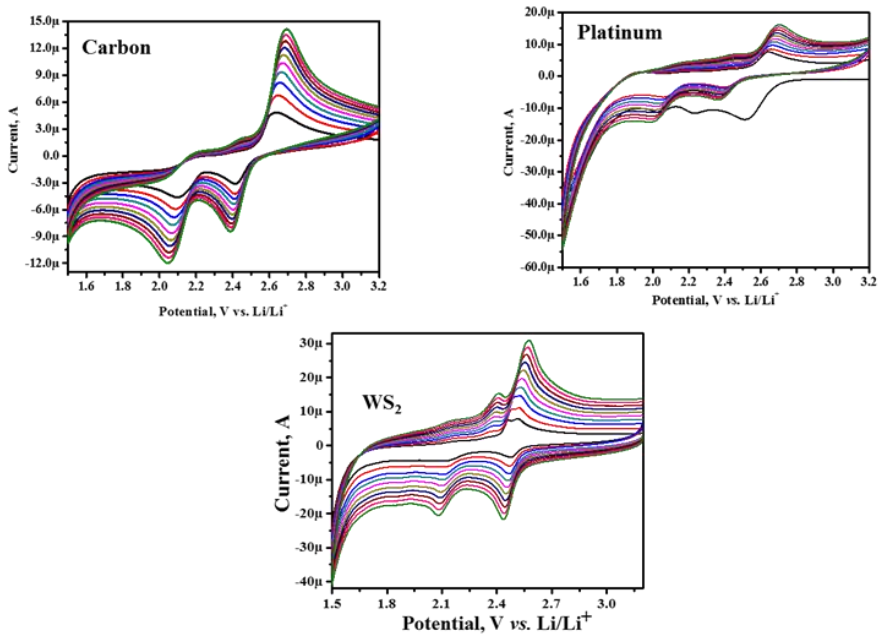

Figure 3.2. Cyclic voltammetric response of carbon, Pt, and WS_2 surfaces at different scan rate (10-100 mV sec^{-1}) in 2mM Li_2S_8 solution.

To get more insights on S_8/S_8^{2-} redox properties, we carried out CV at different scan rates (figure 3.2). A linear increment in Peak ΔE_p potential with scan rate was observed on all the surfaces which account for the irreversibility of the redox process. This could be ascribed to intervene of the chemical charge transfer step and indicates that the reaction was controlled apparently by mass transport of active species. It is further validated from the log values of i_p *vs scan rate (v)* giving a slope of 0.5 at all surfaces denoting the diffusion process (figure 3.3 a) and is in good agreement with the previous reports[107, 108]. We calculated the diffusion coefficient of LiPS (D_{Li2S8}) by using well-known *Randles-Sevcik* correlation as shown below (eqn 1) and it is found to be higher on both Pt (8.01 X 10^{-6} cm^2/sec) and WS_2 (7.96X 10^{-6} cm^2/sec) when compared with that of GC (7.6 X 10^{-6} cm^2/sec) surface. Despite of diffusion coefficient measurement in Li-S coin cell giving an overall cell LiPS diffusion parameter, these values from the three-electrode system are solely with respect to the cathode surface.

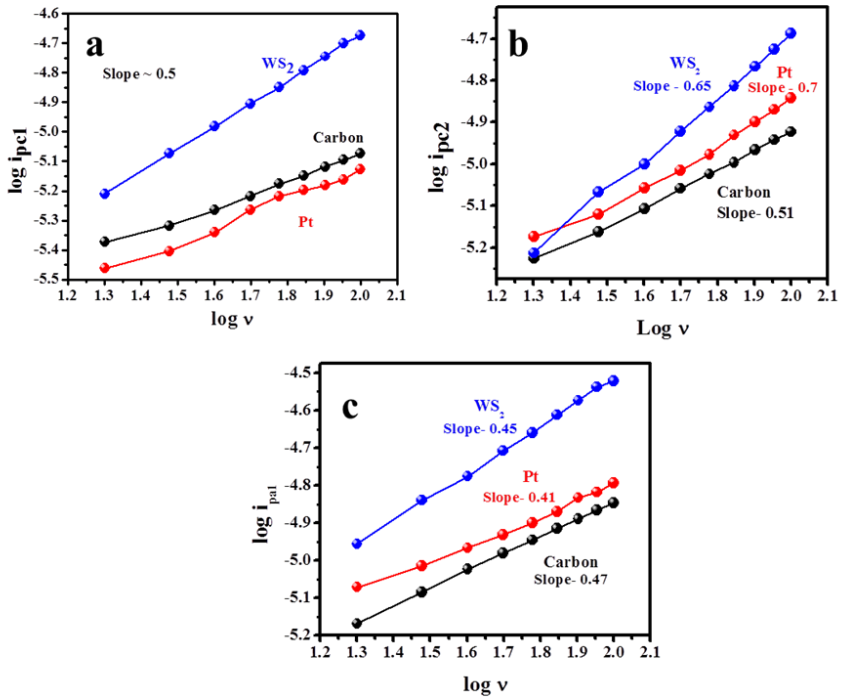

Figure 3.3. *log ip vs log v* plot for (a) cathodic peak (i_{pc1}) at 2.4 V, (b) cathodic peak (i_{pc2}) at 2.1V, (c) anodic peak (i_{pa1}) at 2.6V. The scan rate employed between 10 - 100mV sec^{-1}.

The observed negligible difference (error bar ±0.2) in diffusion coefficient values for different surfaces can be because of the polysulfides getting diffused towards the surface either by absorption or adsorption process.

$$D^{1/2} = i_p / (2.99*10^5)\, n\, (n\alpha_n)^{1/2}\, A\, C\, v^{1/2} \qquad \ldots\ldots\ldots\ldots (1)$$

Where, i_p - peak current(A), A- area (cm^2), C- Concentration (mM), ν-scan rate (mV/sec), D-diffusion coefficient (cm^2/sec), n –number of electrons and α-transfer coefficient. Due to the irreversible features of E_{pc1}, peak position was observed at a higher potential with a potential dependent heterogeneous rate constant. Since diffusion and sweep rate parameters are directly related to the peak potential, catalytic surface's influence on the rate of the reaction can be anticipated. Further, it is corroborated from the heterogeneous rate constant measurement by using *Nicholson* equation as shown below (Eqn 2). It is found that Pt and WS_2 exhibit higher rate constant

value compared to the carbon surface which indicates the facile conversion of polysulfides.

$$k(E_p)= 2.18\ [D\beta nF\nu/RT]^{1/2} \qquad \text{…….} (2)$$

Where, k (E_p) – potential dependent rate constant (cm^2/sec), β- transfer coefficient, R- gas constant (8.314 J K^{-1} mol^{-1}), T-temperature (K). Here, the transfer coefficient value was taken as 0.5 based on the assumption that the peak current is gained from the reversible process[109]. To get a complete understanding of the surface role on lithium-sulfur redox kinetics, we performed Tafel plot measurement *i.e.* current *vs.* over potential relationship, as shown in figure 3.1b. Pt (180 mV/sec) and WS_2 (90 mV/dec) surfaces displays significantly lower Tafel slope value when compared to the carbon (245 mV/dec). Hence, CV derived parameters such as peak potential (ΔE_p), diffusion coefficient and Tafel slope evidently reveal that the surface dependency on LiPS redox reaction kinetics. It is widely known that the unsaturated coordinated planes (active sites) and d-band characteristic present in transition metal/dichalcogenides is responsible for catalytic activity and is proved in several electrochemical reactions. Similarly, aqueous polysulfide redox process is activated by using catalytic surface in solar cell[110, 111], flow battery[112-114] applications which support the surface involved electrocatalysis of sulfur redox process in the Li-S cell.

Certainly, all the polysulfide anions are electron rich and that can share electrons with empty d-band of metal *via* Lewis acid-base interaction, which could bring adsorption at any stage. The liquid polysulfides dissolution is the major cause of shuttling and hence, it is anticipated that the catalytic surface can involve in chemisorption with those LiPS and further in their redox reaction activation. As predicted, the raise of faradic current at this region (2.05 Peak II) on both Pt and WS_2 when compared to the carbon denotes better electroactive species accessibility. Furthermore, E_{pc2} peak potential shifts linearly more cathodic with scan rate and give slopes (log

i_{pc2} *vs* log ν) about 0.51, 0.7 and 0.68 for carbon, Pt and WS_2 surface respectively (figure 3.3b). The slope above 0.5 indicates the domination of surface kinetics rather than diffusion and however, slope value less than 1.0 represents the chemical reactions are still inevitable. To sum up, the adsorption of intermediate soluble polysulfides on catalytic surface significantly reduces the shuttling effect and resolves the major issue related to the capacity fade. The electron transfer rate will be faster on adsorbed molecules than the non-adsorbed and hence strong interaction of LiPS on catalyst surface may have an impact on subsequent reaction *viz.* liquid-solid conversion (Li_2S_4 to Li_2S_2/Li_2S) reaction. It is noteworthy to mention here that most of the cell capacity is gained from the charge transfer process of liquid Li_2S_4 to solid Li_2S conversion.

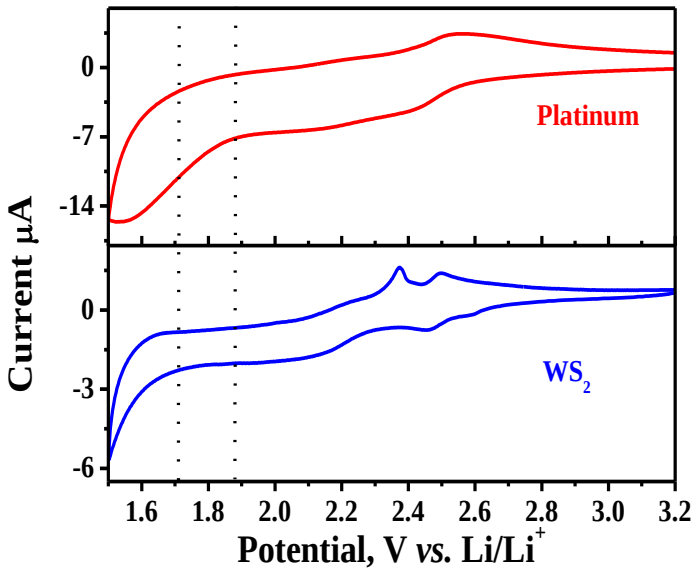

Figure 3.4: Cyclic voltammogram of Pt and WS_2 catalyst modified electrodes in 2 mM Li_2S_8 + 1M LiTFSi in TEGDME solvent (without $LiNO_3$). scan rate: 0.2 mV sec^{-1}.

In the juxtaposition with above suggestion, Pt and WS_2 surface shows a continuous flow of cathodic faradaic current after Li_2S_6-Li_2S_4 redox reaction which can be ascribed to the growth of Li_2S. In addition, the continuous increase in cathodic current in successive cycles is from the conversion reaction of Li_2S_4 to Li_2S rather than from the irreversible reduction of $LiNO_3$. This can be proved by carrying out a controlled experiment without $LiNO_3$ additives and shown in figure

3.4. Hence, current originating from the irreversible reduction reaction of $LiNO_3$ can be neglected here. It is well known that the nucleation followed the growth of Li_2S solely depends upon the nature of the surface rather than the diffusion of active species. As mentioned previously, enhanced LiPS (Li_2S_4) retention on the catalytic surface in conjunction with conductivity can efficiently catalyze the kinetics of Li_2S nucleation (reduced over-potential) which is followed by growth. On the other hand, a very small faradaic current was observed at 1.7 V on the carbon attributing towards the negligible charge/mass transfer occurring between electrode/electrolyte interfaces and illustrating the Li_2S transformation is diffusion limited. Furthermore, Tafel slope (as shown in figure 3.1c) got significantly decreased from 440 mV/dec (Carbon) to 280 mV/dec (Pt) and 300 (WS_2) confirming the electrocatalytic activity. The decreased overpotential and low Tafel value indicate the significance of electrocatalysis driven reaction process in the presence of metal surfaces. This can be due to the polar nature of active sites in Pt and WS_2 providing low surface energy barrier for nucleation and growth of Li_2S compared to the carbon (non-polar) which is in good agreement with the previous reports on conducting substrates[52, 115].

The overall reduction process can be summarized as the following: WS_2 showed better catalytic activity than Pt during the initial stages of reaction which is due to the weak interaction of latter with the polysulfides. But in the subsequent regions, the oxidation of Pt surface encourages stronger interaction of polysulfides and eventually ends up with Pt-sulfide bond formation. In contrast, the inability of WS_2 to oxidize limits itself from retaining the initial activity throughout the redox reaction process. This can be clearly inferred in cyclic voltammogram where the kinetics of the first reduction process undergoes much faster on WS_2 surface, whereas successive reaction (region II & III) is accelerated on Pt surface.

3.3.2 Electrocatalysis in LiPS oxidation:

It is widely postulated that the adsorption of sulfur on metal surfaces has a remarkable effect on electrochemical reactivity. Despite sulfur induced inhibitions in catalytic activity, few reports demonstrate that the sulfur layer significantly enhances the electrocatalytic activity of some metals like platinum and thereby improving the reaction rate. The adsorbed sulfide anion on the catalytic surface like Pt (111), (100) planes favors oxidation and consequential accumulation of elemental sulfur/polysulfides, along with regeneration of the active sites[116, 117]. Similarly, it is expected that the catalytic surface can also influence the Li_2S oxidation kinetics. In agreement with the literature, carbon, Pt, WS_2 surface shows one major anodic peak at ~2.6 V attributing towards the conversion S_8^{2-} intermediate to stable sulfur (S_8). In addition to this, we found a new peak at 1.9 V during oxidation on Pt surface which is not reported elsewhere. To get more insights, we carried out the Li_2S_8 redox reaction on bare polycrystalline Pt electrodes due to its high catalytic activity (figure 3.5).

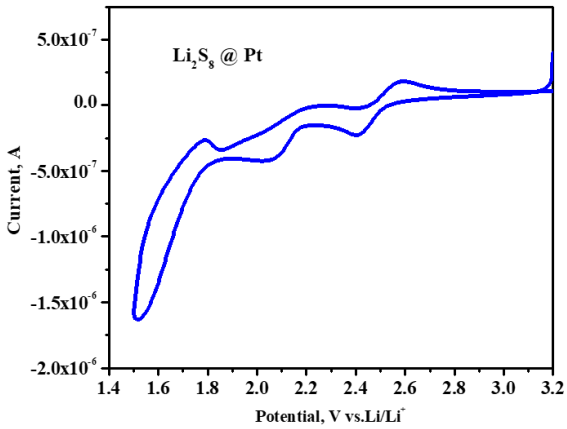

Figure 3.5: Cyclic voltammetric response of polycrystalline Pt surface in 2 mM Li_2S_8 solutions (Scan rate: 0.1 mV sec^{-1})

Polycrystalline Pt surface exhibits similar CV behavior with well-defined peaks, proving the dependency of adsorption and reaction kinetics on surface active sites. Instead, during the reverse cycle, an oxidation peak appears at 1.9 V which is similar to the one observed on Pt and

ascribed to the electro-oxidation of solid sulfides (S^{2-}) to S_4^{2-} on the catalyst surface. Increasing of S_4^{2-} concentration indirectly accelerates the formation of S_6^{2-} followed by its reaction with available Li_2S producing S_8^{2-} intermediates. Therefore, initiation of Li_2S oxidation sequentially promotes the kinetics of the oxidation process on the catalytic surface. However, WS_2 surface did not show any such response at 1.9 V which can be due to the limited number of active sites.

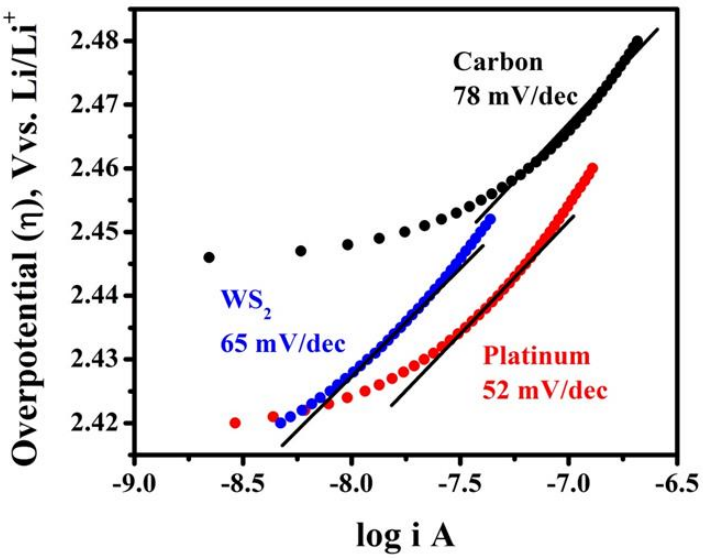

Figure 3.6: Tafel plot for LiPS oxidation peak (~2.6V)

Finally, anodic peak observed at ~ 2.6 V corresponds to the oxidation of S_8^{2-} to stable sulfur (S_8) forms Anodic reaction peak positioning (ipa) was found cathodically shifted from a potential of 2.54 V (carbon) to 2.53 V and 2.50 V for Pt and WS_2 respectively. In addition, current increases linearly with the scan rate and the slopes calculated from the *log v vs log* (i_{pa}) plot are found to be 0.41, 0.45 & 0.47 for Pt, WS_2 and carbon surface respectively (figure 3.3c). Thus, the oxidation kinetics are limited to diffusional process and found to be less than the typical value due to the intervention of chemical reaction. Moreover, we calculated the diffusion coefficient from the plot and found that Pt and WS_2 surface shows 1.47 X 10^{-6} cm^2/sec and 1.35 X 10^{-6} cm^2/sec respectively which are higher than that of GC (1.148 X 10^{-6} cm^2/sec). Tafel slope decreased from 78 mV/dec

for carbon to 52 and 65 mV/dec for Pt and WS_2 respectively (figure 3.6) which demonstrates the involvement of electrocatalysis mechanism in Li_2S oxidation.

From the above observations, it can be inferred that Pt and WS_2 surface shows similar catalytic behavior towards polysulfide's redox. However, their respective reaction mechanism is expected to differ from each other. In the case of Pt, the surface tends to undergo oxidation (Pt^{2+}) and reduction (Pt^0) along with polysulfide's reduction/oxidation during the operation. The interaction between the Pt and PS leads to the Pt-sulfide bond formation at the end of discharge. Subsequently during charging, oxidized Pt surface undergoes reduction while polysulfides getting oxidized. Hence, polysulfides will go through electrochemical reversible adsorption/desorption process on Pt surface which was reported in our earlier studies[77]. In contrast, the interaction between WS_2 and polysulfides is purely based on charge transfer rather than direct bond formation. Edge sites present in the WS_2 including W and S edges have unsaturated dangling bonds that tend to interact with polysulfides more strongly and thus allows the polysulfide's reduction/oxidation on the surface. In brief, three-electrode CV results reveal the role of catalytic surface in (i) enhancing the polysulfide's adsorption (ii) accelerating the liquid (Li_2S_6-Li_2S_4) to solid PS conversion (iii) improving the Li_2S oxidation kinetics. These results are in good agreement with the previous surface driven Li-S studies with various cathodes such as metal oxide, carbides and sulfides. Furthermore, to prove our hypothesis and get more understanding of the electrocatalytic surface effect on polysulfide's redox kinetics, we performed three different potentiostatic measurements by using two electrode coin cells (CR 2032) system.

3.3.3 Adsorption of polysulfide on catalytic interface:

Adsorption of LiPS is one of the dominant factors which determine the redox kinetics on the catalyst surface and hence fundamental understanding of such properties is critical. As

predicted in CV, catalytic surface accelerates the solid Li_2S formation and then obviously one can assume that the adsorption of Li_2S_6/Li_2S_4 holds the key factor for the same. To reveal the adsorption driven electrocatalysis based Li-S system, we performed chronocoulometric test accompanied with UV-vis spectroscopy. It is well known that the chronocoulometric method is often used to recognize and quantify the adsorbed reactants on the surface from the intercept of charge (Q) *vs.* $t^{1/2}$ plot, so called surface coverage (Γ) [118, 119]. Here we estimate the surface coverage of adsorbed LiPS (Li_2S_4) on various surfaces by measuring charge with respect to the applied potential for about 600 seconds. The chronocoulogram wave obtained when the potential of the working electrode stepped to 2.1 V is displayed in Figure 3.7a showing an increment in the charge on Pt and WS_2 surfaces. Besides, surface coverage estimated from the intercept of Q *vs* $t^{1/2}$ (after subtracting the double layer charge by using equation 3) was found to be higher on Pt (4.9×10^{-7} mol cm^{-2}) and WS_2 (6.5×10^{-8} mol cm^{-2}) when compared to the carbon surface (3.68×10^{-8} mol cm^{-2}) (figure 3.7b). The resultant surface coverage estimation demonstrated that the catalyst surface is covered with adsorbed LiPS molecules.

$$Q = nFA\Gamma \qquad \text{..... (3)}$$

Where Q - the charge, n - the number of electrons, F - the Faraday constant, A - the area of the electrode (geometric) and Γ - surface coverage in mol cm^{-2}. Furthermore, the adsorption capability test was carried out using UV- Vis spectroscopy along with the visual inspection analysis. For the static adsorption studies, a known amount of electrocatalyst was added in 10 mmol L^{-1} of Li_2S_4 in TEGDME followed by vigorous stirring for 1hr and the whole solution was kept undisturbed overnight. In figure 3.7c, blank Li_2S_4 showed an absorption peak around 420 nm and the peak intensity was found to decrease when added with the adsorbents in order of C <WS_2 < Pt confirming the strong affinity of polysulfides towards the well-known catalysts. These results were

in good agreement with the visual inspected camera images, showing a drastic color loss for Pt, then WS_2 indicating the better adsorption of polysulfides onto these catalytic surfaces than carbon (as shown in figure 3.7d). Adsorption behavior ascribed to the transfer of an electron from the electron rich polysulfide species to the available vacant d-orbital on the metal surface. Also, these findings can be explained as the facile charge transfer from negatively charged $Li_2S_4^{2-}$ to the positively charged metal/metal sulfide active sites compared to the neutrally charged carbon surface resulting in high affinity.

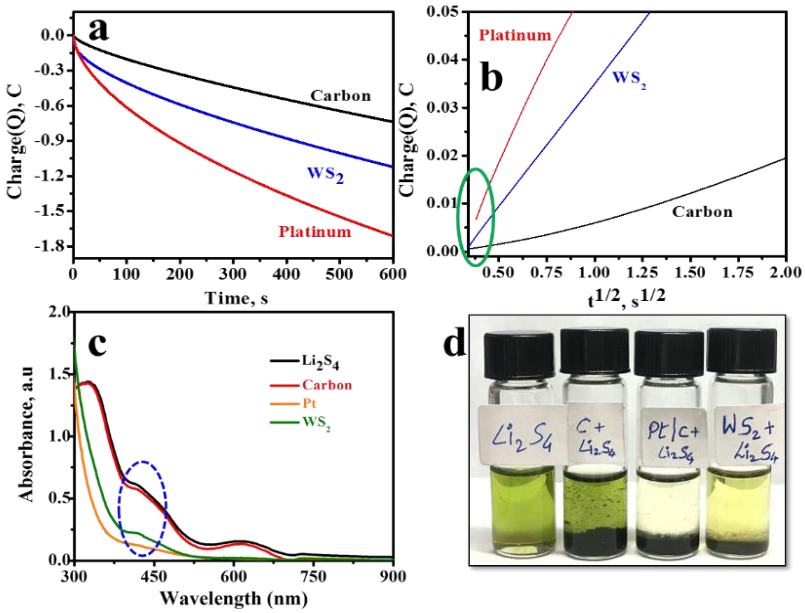

Figure 3.7. Adsorption characteristics of LiPS on catalytic surfaces**:** (a) chronocoulometric plot Charge *vs* time (b) Charge *vs* $t^{1/2}$ (c) UV-Vis spectrum and (d) visual inspection of LiPS color changes in presence of carbon, Pt and WS_2 materials.

3.3.4 Li_2S_2/ Li_2S growth on the catalytic interface

Adsorption studies can validate the potential ability of catalytically active sites to hold intermediate LiPS during the reaction, thus greatly hinders the shuttling effect. Pre-adsorbed LiPS obviously undergo subsequent reactions in faster kinetics compared to the non-adsorbed. As illustrated in CV curve (figure 3.1a), the electrocatalytic surface reduces the overpotential for Li_2S

nucleation and accelerates the conversion of liquid PS (Li_2S_4)-to-solid (Li_2S) thereby gaining high capacity. Previous reports elucidated that polar conductive/metal oxides provide low surface energy that favors the electrodeposition of Li_2S via nucleation followed by growth[115]. Also, we recently reported that Li_2S deposition preferentially occurs on catalytically active sites such as edge planes compared to the basal by lowering the activation energy required for the reduction[120]. However, the effect of the catalytic active site on nucleation followed by growth and spatially controlled deposition of LiPS is persisting in its status of being unexplored. We have performed potentiostatic discharge of Li_2S_4 at 2.05 V and monitored insoluble reduction products (Li_2S_2/Li_2S) for about 10 hrs (Figure 3.8a-c). Prior to doing this, we executed the typical discharge up to 2.02 V with C/20 current rate to reduce all the higher polysulfides to Li_2S_4. In figure 3.8(a-c), the shape of transient time *vs.* current differs from each other which reveals that the nucleation and growth pattern is varying with respect to the surface. The current was reached higher in shorter duration on the catalyst surfaces compared to the carbon confirming the early nucleation of Li_2S which supports the CV data. Also, the measured charge was found to be higher for catalytic Pt (0.165 Q/cm^2) and WS_2 (0.15 Q /cm^2) surfaces than carbon (0.12 Q/cm^2) which indicate the high yield deposition of Li_2S. Obviously, more Li_2S deposition yields an impingement effect leading to the Li_2S growth termination[121, 122]. However, Li_2S growth is controlled by two types of mechanism *viz.*, instantaneous, and progressive nucleation which depends upon the nature of the substrate being used. In general, instantaneous nucleation followed by growth occurs in a three-dimensional pathway whereas progressive nucleation leads a two-dimensional pathway over a longer period.

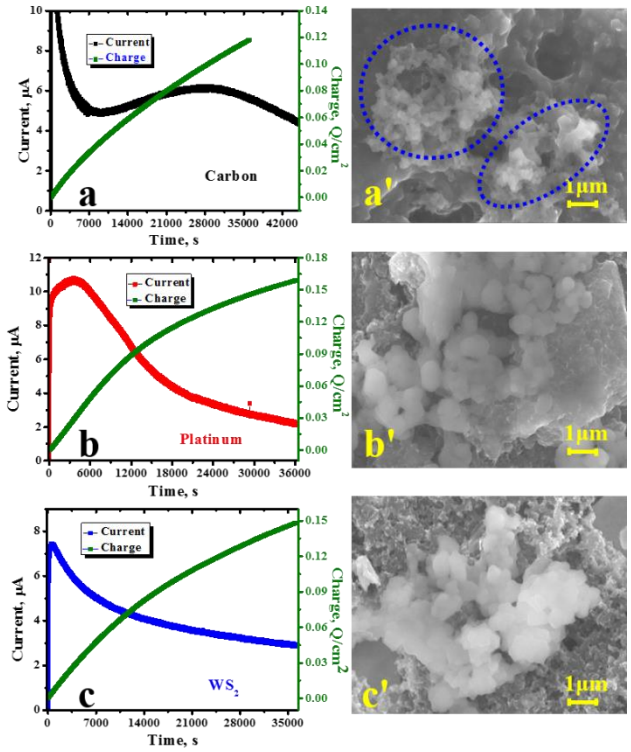

Figure 3.8. Li_2S Nucleation and growth studies**;** (a-c) potentiostatic deposition of Li_2S at 2.05 V on carbon, Pt, WS_2 surface and their corresponding SEM images (a'-c') [Image scale bar 1μm; 13kx resolution]

To ascertain the type of nucleation and growth on the catalytic surface, we examined each transient curve with developed *Avrami* theory and its correlated equation 4 & 5 are shown below.

$$\left(\frac{i}{i_{max}}\right)^2 = 1.9542\ \frac{t_{max}}{t}\ \left[1\text{-}\exp\left(-1.2564\frac{t}{t_{max}}\right)\right]^2 \qquad \text{…….. (4)}$$

$$\left(\frac{i}{i_{max}}\right)^2 = 1.2254\ \frac{t_{max}}{t}\ \left[1\text{-}\exp\left(-2.3367\frac{t}{t_{max}}\right)^2\right]^2 \qquad \text{…… (5)}$$

Dimensionless relation between i^2/i^2_{max} vs. t/t_{max} predicts instantaneous Li_2S nucleation which proceeds on ($t < t/t_{max}$) both catalytic surface and that obviously leads to the 3D growth (figure 3.9). But, progressive Li_2S nucleation observed on the carbon surface restricts the growth in 2D direction and allows limited deposition. Furthermore, morphological studies of 10hrs

discharged cell were carried out to prove the Li_2S growth which is shown figure 3.8a'-c'. SEM images show similar faster growth of Li_2S particles on both catalytic surfaces with larger particle sizes. But limited Li_2S deposition was observed on carbon even after potential applied for longer duration and has a smaller particle size. In fact, larger particle size increases the interfacial contact with the cathode surface, and it is highly beneficial for Li_2S oxidation. This can be explained by the following aspects (i) strong interaction between Li_2S and catalytic active sites such as Pt (100), (111) planes, unsaturated edge planes of WS_2 (ii) higher conductivity of the surface that reduces the activation energy and prompts the Li_2S nucleation followed by 3D growth. This can be realized in two folds' higher discharge capacity gained on Pt and WS_2 surfaces with smaller surface area compared to the carbon. This is well agreed with previous reports that conductive surfaces enhance the liquid to solid PS conversion. Therefore, surface with catalytically active sites is capable of tuning the Li_2S growth mechanism with reducing nucleation overpotential and offers more capacity close to the theoretical value from this region.

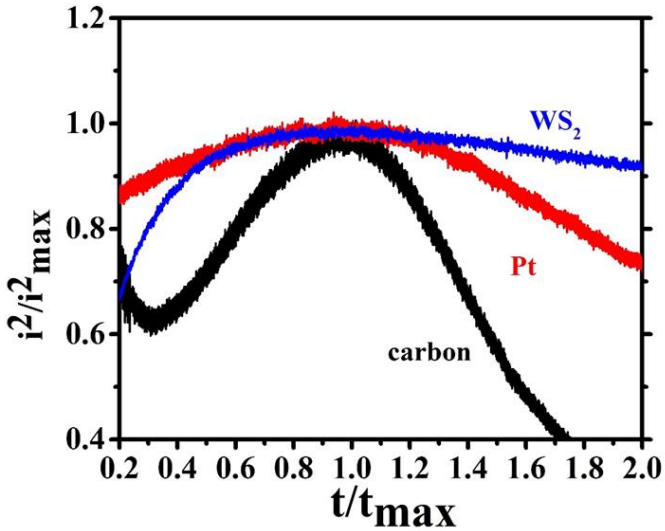

Figure 3.9. Li_2S nucleation dimensionless t/t_{max} vs. i^2/i^2_{max} plot for carbon, Pt and WS_2 surface.

Despite accelerating the Li_2S deposition, inherent problems such as insulating nature and

their sluggish oxidation kinetics practically limit the cell reversibility and capacity retention. Strong interaction between the LiPS and catalytic active sites anticipates the catalysis of Li_2S oxidation as well. Also, cathode surface should essentially have reversible behavior towards adsorbed molecules which can regenerate the active sites for PS readsorption. To evaluate these premises, we carried out potentiostatic electrochemical impedance spectroscopy to identify the charge transfer properties of the surface during discharge-charge reactions.

3.3.5 Charge transfer at the catalytic interface:

It is well known that, extent of active material reduction (Li_2S_8)/oxidation (Li_2S) during discharge/charge modifies the charge transfer resistance and ionic diffusion on the cathode surface. Particularly, the insulating nature of charge-discharge products and the irreversible behavior of chemically adsorbed polysulfides on the cathode surface significantly increases the impedance leading to the capacity fade. Here, we monitored the Pt, WS_2 and carbon cell impedance at different discharge-charge potentials as shown in figure 3.10a-c. The Nyquist plot reveals those potential dependent changes of the semicircle in higher and medium frequency region and an inclined slope line in low frequency region. To correlate obtained data, equivalent circuit fitting was performed with appropriate parameters and the values are given in table 3.2. Electrolyte resistance R_1 and charge transfer resistance R_2 from the anode surface are found to be at the high frequency region of impedance spectra. However, these resistances have undergone very negligible changes with respect to the potential and thus their effects on the cathode surface's activity is insignificant. On the other hand, there were substantial potential dependent changes for the resistance, R_3 (2nd semi-circle) in the mid frequency region which correspond to the charge transfer at the cathode interface.

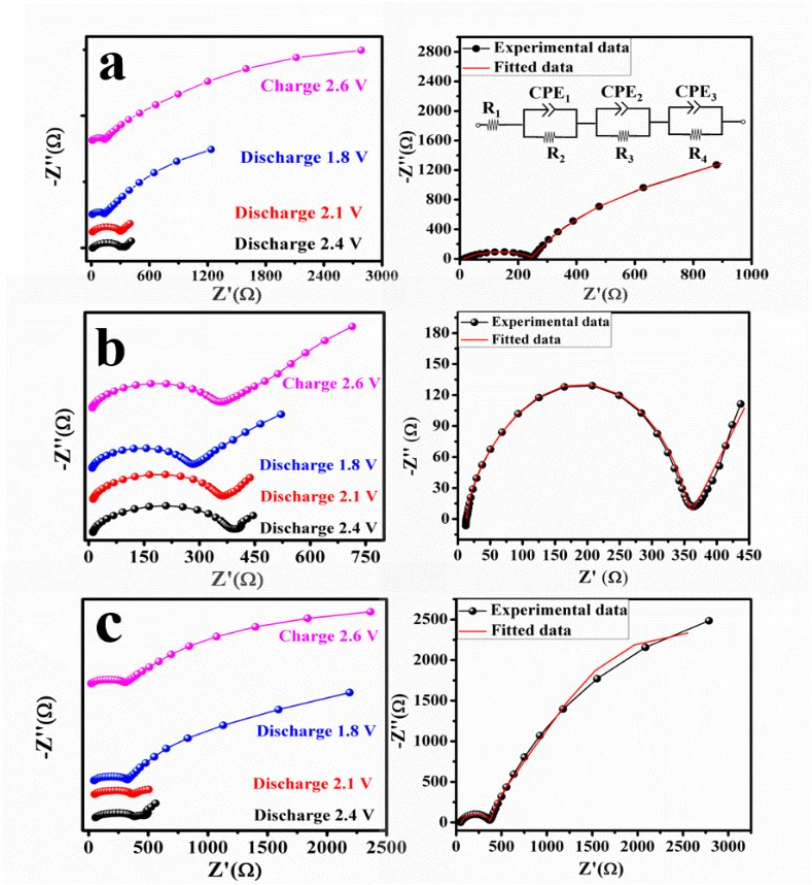

Figure 3.10. Charge transfer properties**:** Nyquist impedance spectra of LiPS on (a) carbon (b) Pt (c) WS_2 surfaces at different discharge/charge potential and their corresponding equivalent circuit (right side). AC frequency employed between from 1MHz to 1mHz with 10mV amplitude.

Typically, cathode charge transfer resistance is originated from the intermediate polysulfide reaction followed by the morphological changes on cathode surfaces with respect to the potential. As shown in table 3.2, Pt and WS_2 surface exhibits a slight decrease in the charge transfer resistance during the discharge whereas carbon shows drastic reduction implying the higher accessibility of the cathode interface. This can be due to the huge volume changes seen on carbon which reduce their interaction with the polysulfides ending up inactive material dissolution. But the presence of active sites on Pt and WS_2 surface helps in polysulfide adsorption avoiding the volume changes resulting in slight R_3 variation with respect to the discharge. Resistance R_4

corresponds to the formation and dissolution of S_8 and Li_2S during cycling. As clearly seen in figure 3.10, R_4 decreases drastically at the midway of discharge on all the surfaces indicating sulfur utilization and the semi-circle reappeared in low frequency region on discharge completion confirms the Li_2S formation.

Table 3.2. Comparison of LiPS charge transfer resistance (R_3) variation during discharge/charge on different surfaces

	Carbon			Platinum			WS_2		
Potential	R_2	R_3	R_4	R_2	R_3	R_4	R_2	R_3	R_4
Discharge 2.4	30	320	1780	14	393	786	45	337	1387
Discharge 2.1	18	278	980	13	328	450	38	309	380
Discharge 1.8	13	114.4	2050	10	266	3738	56	251.6	3167
Charge 2.6	14	117.7	6291	13.2	374	3486	50	311.3	3278

Similar fashioned impedance changes can be expected upon the charging process to ensure the cell reversibility. Yet again, R_1 and R_2 resistance undergo negligible changes when charging progress as like the discharge one. More importantly, minimal changes in R_3 resistance was observed during charging on carbon surface at 2.6 V when compared with that of the discharge at 1.8 V. This observation indicates that irreversible interfacial change like volume expansion reduces the polysulfide interaction with surfaces resulting in capacity fade upon cycling. However, Pt and WS_2 surface showed the same negligible R_3 variation confirming their availability for further polysulfide interaction improving cycle reversibility. Thus, we prove the significance of having a catalytic surface towards better polysulfide adsorption for enhanced redox kinetics and improved cell reversibility.

3.4 Conclusion

In this chapter, we demonstrated that the significance of electrocatalytic surfaces on lithium-sulfur redox kinetics by electrochemical potentiodynamic and potentiostatic methods. Catalytic interface reduces the redox overpotential and enhances the surface diffusion properties of LiPS anions. Thorough analysis corroborates that enhanced adsorption of soluble LiPS at the catalytic interface and assists the successive reactions rather than dissolution. More importantly, catalyst exhibits a substantial activity towards LiPS liquid-to-solid conversion and directs the Li_2S nucleation process *via* instantaneous growth, which has a direct impact on high capacity gaining. In-depth analysis further confirms that electrocatalyst plays a predominant role in accelerating the kinetics of Li_2S process among multistep LiPS redox reactions. Furthermore, impedance analysis makes evident that the potential ability of catalytic active sites for improving the cell reversibility.

CHAPTER 4 FACILE SYNTHESIS OF ELECTROCATALYTICALLY ACTIVE NBS_2 NANOFLAKES FOR ENERGY-RELATED ELECTROCATALYSIS

4.1 Background and Motivation

Over the past decade, intense research efforts have been taken to stabilize the polysulfide shuttle process in the Li-S battery system mainly by physically constraining the sulfur within the pores of various carbon materials[51, 123, 124]. However, the low active material loading in these electrodes and their poor polysulfides adsorption capabilities have limited success. These unsolved concerns necessitate a critical need for a fundamental breakthrough to stabilize the polysulfide shuttle effect. Recently, our group proposed an electrocatalytic driven approach to Li-S batteries, where metals like Ni, Au and Pt were found to enhance reaction kinetics and stabilize the polysulfide shuttle process[28, 29]. Even though this innovative approach taken on cell design has improved the overall electrochemical performance, the high cost and limited availability of the elctrocatalyst are surely constrained their practical applications. Hence, there is a great demand to find cheap and efficient electrocatalysts with the aim of producing these promising energy-related technologies commercially viable. In search of efficient and cost-effective electrocatalyst as an alternative to those noble metals, two-dimensional transition metal dichalcogenides, XS_2 (X=Mo, W) materials were found to be potential candidates as they are previously reported as catalysts in hydro-desulfurization[125], solar cells[126], photocatalysis, hydrogen evolution reaction[127-130] and for their stability towards sulfur chemistries[131]. XS_2 materials with their synergism among metal d-orbitals and the unsaturated heteroatom (such as sulfur) resulted in an effective d-band structure, imparting catalytic characteristics similar to the d-band of Pt. The catalytic efficiency of these materials for a reaction was correlated to the number of exposed edge sites that have unique chemical and electronic structure when compared to their respective basal planes (0001) [132].Hence, it is crucial to design and improve the preferential catalytic active sites (edge

sites) for efficient reaction kinetics. Considerable efforts were made to maximize the no of active catalytic sites in XS_2 materials through various process including designing, modifying the structure and morphology, through adopting various synthesis routes. Among the various configurations including nanoparticles, porous structures, nanowires, and hybrid heterostructures , atomically thin two-dimensional layered structure was emerged as an exciting area of catalytic activity due to its highly exposed edge sites and high accessibility of large catalytic surface[133-136]. There are a substantial number of literature studies which are exclusively on Group 6 TMDs like MoS_2, WS_2, $MoSe_2$ and WSe_2 when compared with other group TMD materials[137-140].This limited study outside of the Group 6 TMDs urges for exploiting group 5 TMDs including VS_2, VSe_2, NbS_2, $NbSe_2$, VTe_2, TaS_2, etc. NbS_2 exhibits the same lamellar structural features of MoS_2 and WS_2, which allowed researchers to easily find an alternative promising catalyst to MoS_2/WS_2[141].

The catalytic, intercalation, optical, and superconductivity properties along with its abundance make NbS_2 a potential candidate among TMDs [142]. NbS_2 is unique with the lack of one electron in the d bands which gives the compound its peculiar electronic and magnetic properties[128, 143]. Also, like MoS_2, NbS_2 has a prismatic 2H structure and is capable of forming in the 1T metallic phase. As per reports, NbS_2 has four phases: two stoichiometric and two non-stoichiometric – 2H NbS_2 ,3R NbS_2 and 2H $Nb_{1+x}S_2$,3R $Nb_{1+x}S_2$, respectively[144]. NbS_2 has been fervently studied as a hydrodesulfurization catalyst in the fields of petroleum purification, sensors, cathode materials and superconductors with a wide transition temperature range[145-147]. But the difficulty in the preparation of stoichiometrically stable NbS_2 nanomaterials hinders it from practical applications. The oxides like MoO_3, WO_3 can react with low pressure sulfur to form corresponding sulfides; but, Nb_2O_5 or NbO_2 requires a high sulfur pressure around 6 atm and

high temperature to form stable NbS_2 crystals which hold back from their simple synthesis routes[148-150]. Also, the number of layers and the thickness of the NbS_2 crystals synthesized cannot be controlled. Thus, it is a challenge to develop a facile synthesis route for few-layered NbS_2 flakes[150]. Chemical vapor deposition involving the thermal decomposition of organometallic niobium precursors is considered as a viable technique for the synthesis of nano-NbS_2[141, 151]. But through CVD, it is more likely to form Nb_2O_5 and NbS as the end products of these reactions. The limited previous studies on NbS_2 nanosheets hinders their exploration in various applications. Thus, it is essential to develop a novel synthesis route for NbS_2 which addresses these key issues. Still, the traditional hydrothermal and other wet chemical synthesis routes have limited controllability on the composition and crystal structure of NbS_2 nanomaterials[152, 153]. These well explored techniques may lead to perceptible changes in the catalytic performance. In addition, the catalytic activity has an intrinsic correlation with the nature, structure and composition of the catalyst. Crystalline nature is an indispensable parameter that can affect the figures of merit namely Tafel slope, turn-over frequency (TOF) and stability of the catalyst towards catalytic performance[153]. Thus, engineering the crystalline structure of NbS_2 is the key factor for enhanced electrocatalytic activity. Lastly, it is indeed essential to develop a facile route for the synthesis of highly crystalline NbS_2 nanostructures for energy related electrocatalysis. Towards this, initially, NbS_2 was synthesized and its catalytic activity towards hydrogen generation is studied, then their Li polysulfide adsorption capability was examined.

The ongoing pursuit of hydrogen as a future energy carrier calls for hydrogen generation catalysts[154]. Active sites in catalysts are normally formed by unsaturated surface atoms with dangling bonds. Unlike the inert basal planes of Group 6 TMDs, the catalytically active basal planes of Group 5 compounds can provide enhanced HER activity and thus can outpace any other

recently known electrocatalysts[155-158].Group 5 TMDs, including NbS_2 with highly metallic nature and a favorable ΔG, are touted to surpass Group 6 TMDs in terms of HER catalytic activity without any further chemical modification, but it has not been experimentally proved yet. The enhanced activity at the basal planes of NbS_2 is not clearly understood. Also, H binding on the basal planes can be improved by increasing the surface area and conducting channels. Herein, we experimentally explore the electrochemical HER activity of highly crystalline NbS_2 nanoflakes as an improved electrocatalyst because of their low onset potential, high exchange current density, and low Tafel slope. In addition, we show an improvement in the H_2 generation reaction kinetics through the addition of a graphene conductive matrix in between NbS_2 nanoflakes. Also, we aim to further examine the ability of transition metal disulfides in the presence of high surface area matrix like carbon cloth (CC) to adsorb LiPS by investigating bare CC, NbS_2/CC and their interaction with PS being an electrocatalyst for enhanced performance in Li-S batteries. Further, the adsorption of LiPS onto the catalytic surface and the electrocatalysis driven electrochemical performance of NbS_2 nanosheets loaded on CC were studied in detail.

4.2 Experimental methods

4.2.1 Synthesis of NbS_2, NbS_2/G

NbS_2 nanoflakes were synthesized using a tube furnace to anneal commercial powdered niobium (1 g, Alfa Aesar, >99% purity) with elemental sulfur (3 g, Sigma Aldrich, >99% purity). The precursors including sulfur and niobium were placed in the first and the middle zone of the tube respectively as shown in Figure 4.1, which schematically illustrates the experimental setup. A constant flow of argon was passed through the tube during the annealing procedure to prevent niobium metal from oxidizing into niobium oxide. The temperature of the furnace was ramped up to the set temperature in 100 minutes, and then kept at the temperature for 80 minutes before being

allowed to naturally cool back to room temperature. The synthesis was done at various temperatures of 750, 850, 950, and 1050 ^{o}C. The niobium to sulfur mass ratio used was 1 : 3. NbS_2/rGO was synthesized by sulfurizing the mixture containing Nb with 20% of GO (prepared through a modified Hummers method) under an argon atmosphere at a temperature of 1050 ^{o}C. The synthesis parameters of NbS_2/rGO were maintained the same as those for the synthesis of NbS_2 flakes.

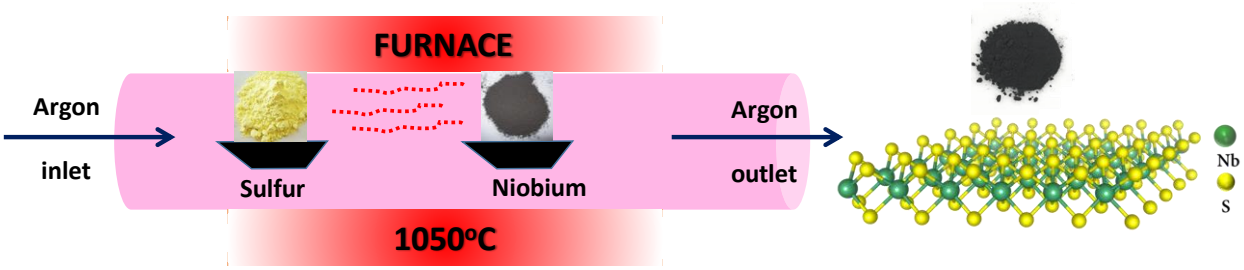

Figure 4.1. Schematic representation of the synthesis of NbS_2 nanoflakes.

4.2.2 Loading NbS_2 onto carbon cloth (CC)

For loading the semiconducting NbS_2 samples on carbon cloth for improving the conductivity of the whole system, the prepared NbS_2 nanoflakes were sonicated in water: ethanol (3:4 ratio) for 1 h. The disintegrated NbS_2 individual flakes were filtered through the carbon cloth which was kept on the whatman filter membranes. The NbS_2 flakes got deposited onto the CC and was used for further characterization and electrochemical measurements.

4.3 Results and Discussion

The crystal structures of NbS_2 synthesized at different temperatures were examined using XRD. The composition of the material formed by annealing at varying temperatures confirms the temperature dependent formation of pure phase NbS_2 and the corresponding XRD patterns of the materials formed are shown in Figure 4.2a. The NbS_2 formed at a temperature of 750 ^{o}C contained

slight traces of unreacted sulfur and Nb_2O_5. The mixture formed at 850 ^oC contained diffraction peaks of both Nb_2S_8 and Nb_2O_5. When the precursors were heated up to 950 ^oC, a composite mixture of NbS_2 and Nb_2O_5 was formed. But we also found here a highly intense peak of unreacted organosulfur. Further when the temperature is increased to 1050 ^oC, NbS_2 is formed with highly intense peaks which correspond to the highly crystalline nature of the as-formed NbS_2 from the higher growth temperature. The sharp peak (003) shows the layer structured NbS_2 with layers piled up with respect to the C axis. The diffraction peaks from the (104) and (015) planes correspond to the disordered and randomly distributed NbS_2 nanosheets. The XRD data analysis indicates the 3R-type rhombohedral structure of NbS_2 at 1050 ^oC with lattice constants, a = b = 3.330 Å and c = 7.918 Å (PDF: 03-065-3655).

Raman scattering measurements were carried out for NbS_2 nanoflakes synthesized at 1050 ^oC and the results are shown in Figure 4.2b. There are four major non-degenerate Raman active modes, at around 290, 330, 386, and 450 cm^{-1} representing E modes (E_1 and E_2) and A modes (A_1 and A_2), respectively. Raman spectrum with all the 4 active modes predicts that NbS_2 exists in the 3R phase. [141] The peaks at 386 cm^{-1} and 450 cm^{-1} are assigned to the A1 and A2 modes of 3R-NbS_2 respectively. A sharper A1 mode at 386 cm^{-1}revealing the crystalline nature of the NbS_2 nanoflakes. The broad peak observed at 158 cm^{-1} is attributed to the existence of single crystalline NbS_2 with defects that help in enhancing the conductivity towards better catalysis. Furthermore, E modes at 330 (E_2) and the shoulder peak at 290 (E_1) correspond to the rigid layer modes whose intensities are relative to the thickness of the layers. In our case, E mode peaks are less sharp which indicates the presence of few-layered NbS_2 nanoflakes. To reconfirm the crystal phase and its influence on conductivity, we calculated the optical bandgap from UV vis absorption spectra. The absorption spectra were collected for the NbS_2 nanoflakes, which were initially dispersed in a

4 : 1 ratio of water-ethanol mixture (Figure 4.2c and d). A characteristic excitonic absorption shoulder around 400 nm was found (Figure 4.2c) and the bandgap calculated from the absorption spectra using the Tauc method was found to be around 1.49 eV (Figure 4.2d), which suggests a semiconducting behavior of 3R-NbS_2. This observed finite optical indirect bandgap confirms the nonmetallic behavior of the synthesized NbS_2 nanoflakes. The inset of Figure 4.2c shows the photograph of the synthesized grey powder; the yield was high through this simple synthesis technique.

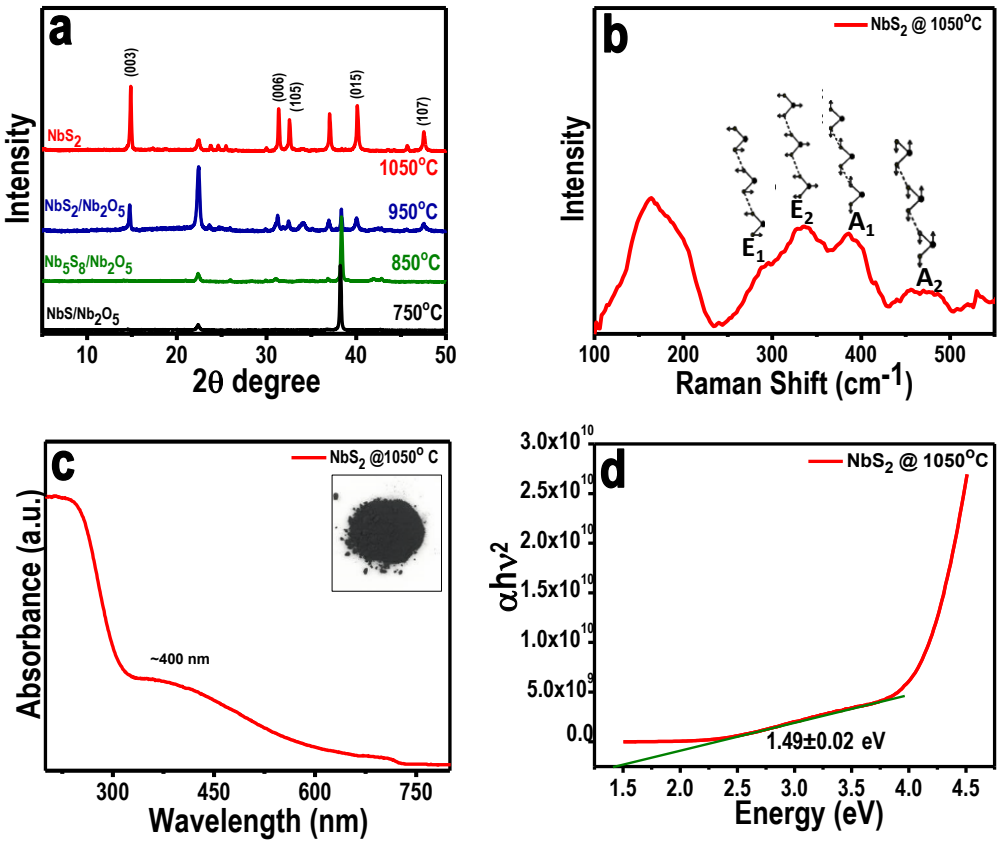

Figure 4.2. Characterization of NbS_2 nanoflakes. (a) XRD patterns of NbS_2 flakes synthesized at different temperatures showing the formation of pure phase NbS_2 nanoflakes. (b) Raman spectrum showing the characteristic vibration modes of NbS_2. (c) UV vis absorption spectra of NbS_2 flakes synthesized at 1050 °C (inset: photograph of the as-synthesized NbS_2 powder). (d) Tauc plot of NbS_2 nanoflakes showing an indirect bandgap of ~1.49 eV.

We examined the morphologies of all the synthesized NbS_2 nanoflakes. Figure 4.3a–d show the SEM images of the as synthesized NbS_2 nanosheets at different temperatures, viz. 750, 850, 950 and 1050 ^oC. The morphological changes are obvious as the temperature increases which confirms the structural formation of pure phase NbS_2 from the NbO/NbS mixture. At 750 ^oC, the nanoflakes coalesced together and later at 850 ^oC they become flakier with fewer unreacted precursors. At 950 ^oC, hexagonal platelets started forming and finally at 1050 ^oC, the flakes formed with a uniform hexagonal platelet morphology whose lateral dimensions extended from a few nm to 2 mm. This also confirms the temperature stability of the NbS_2 nanoflakes. At 1050 ^oC the nanoflakes were found to be layered platelets with definite edges and clearly exposed basal planes which can be correlated with the absence of restacking of the as-formed niobium sulfide nanoflakes.

TEM monitoring of NbS_2 annealed at 1050 ^oC revealed the crystalline nature of the synthesized nanoflakes (Figure 4.3e and f). The lattice fringes were highly ordered with a lattice plane distance of 0.29 nm which corresponds to the (0 1 0) or (1 0 0) plane of highly crystalline NbS_2. The as-synthesized NbS_2 nanoflakes were also found to be very thin and have a defect-free structure.

The evolution of surface morphology depending on the growth temperature has been studied. During the growth, as the temperature increased, the vapor pressure of sulfur got increased up to 1 atm and the vapors of sulfur reacted with Nb particles to form NbS_2 nanoflakes. At a low temperature, the formed coalesced NbS_2 flakes showed a smooth surface with sharp edges; but, the Nb to NbS_2 transformation was incomplete. However, at a higher temperature, the flakes formed were coarse and distinct and their edges were more precise.

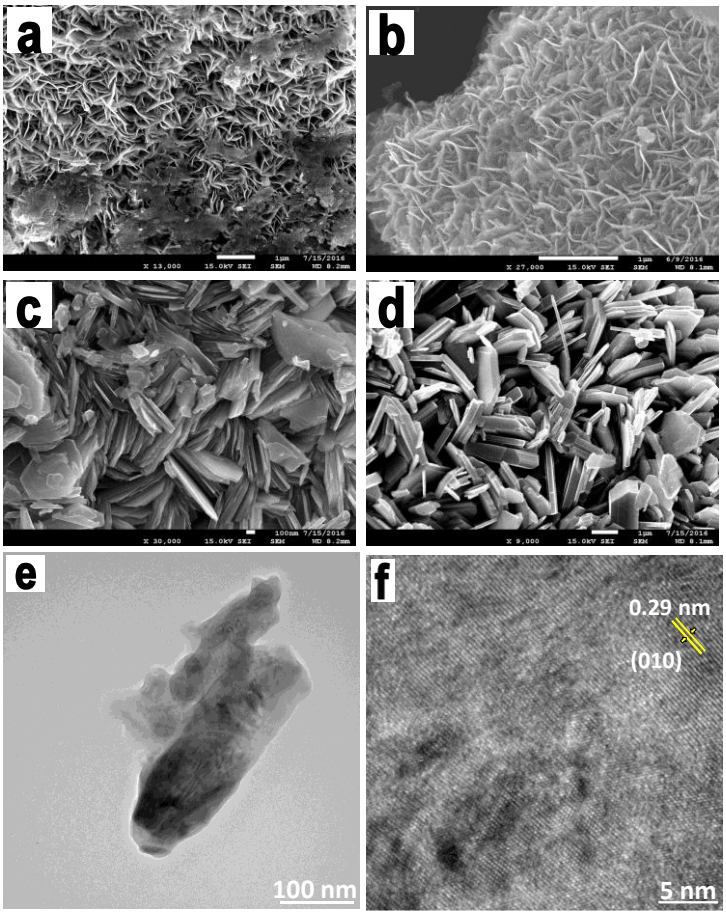

Figure 4.3. SEM images of NbS_2 nanoflakes. (a) 750 ºC, (b) 850 ºC, (c) 950 ºC, and (d) 1050 ºC showing the morphological changes while forming the pure phase NbS_2, (e) and (f) are the TEM images of the formed NbS_2 at 1050 ºC.

A high electrocatalytic activity can be achieved either by increasing the number of exposed active sites, improving the conductivity of the material, or incorporating a cocatalyst[157, 159, 160]. Here, the addition of graphene oxide (GO) to the Nb precursor and its further annealing in the presence of sulfur under an argon atmosphere at 1050 ºC resulted in the thermal reduction of GO along with the sulfurization of Nb to form the NbS_2–rGO composite. The prepared NbS_2–rGO composite was characterized with microscopic techniques and the results are shown in Figure 4.4. The NbS_2 nanoflakes were found to be uniformly dispersed on the graphene surface and retain their crystalline nature.

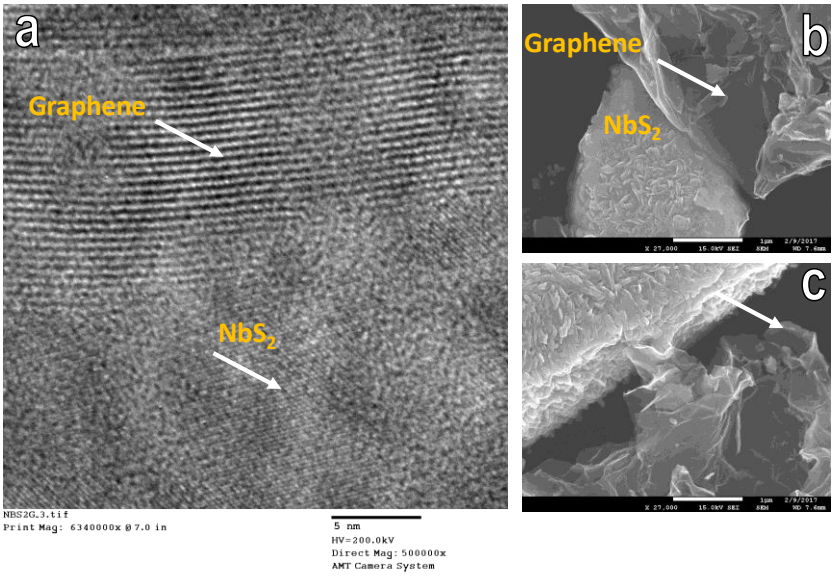

Figure 4.4 a) TEM image of NbS_2/rGO composite. b) SEM images of NbS_2/rGO composite

XPS of NbS_2/rGO was carried out to estimate the oxidation states of Nb and S and the presence of C as shown in Figure 4.5. It was found that Nb exists in the +4 oxidation state, which can be clearly determined from the binding energies of Nb $3d_{3/2}$ at 206.55 eV and Nb $3d_{5/2}$ at 203.8 eV. These results match well with the previous reports and thus confirm the formation of NbS_2 nanoflakes in the presence of carbon. Also, the oxidation state of Nb(+4) is well maintained during the reduction of GO which brings about charge balance during the one-pot synthesis of the NbS_2/rGO composite.

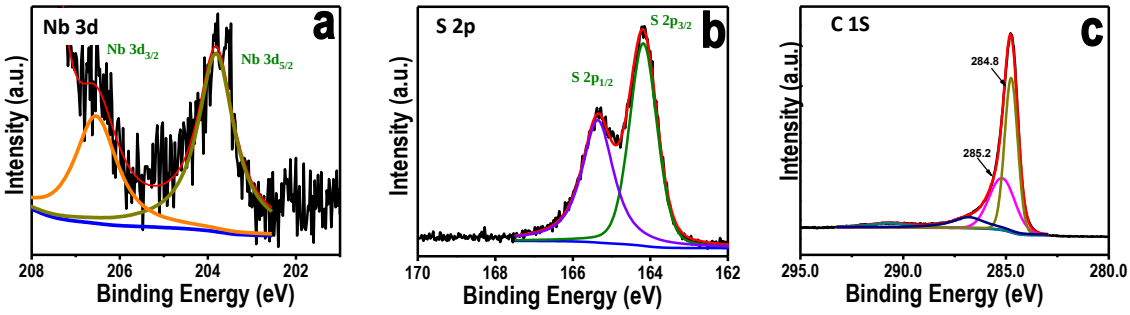

Figure 4.5. XPS of NbS_2/rGO composite towards HER

Moreover, the spectrum showed wot peaks at 162.5 eV and 163.6 eV which correspond to the S $2p_{3/2}$ and S $2p_{1/2}$ components of NbS_2, respectively. The peaks at 284.8 eV and 285.2 eV correspond to the sp^2 graphitic carbon and sp^3 carbon of reduced graphene oxide in the NbS_2/rGO composite.

4.3.1 HER studies of NbS_2 nanoflakes and NbS_2/rGO

Embedding NbS_2 nanoflakes in the graphene matrix is expected to enhance the electrochemical hydrogen evolution through the utilization of the high surface area and conductance of graphene [161-163]. Linear sweep HER measurements have been performed for the NbS_2 based electrocatalyst at a scan rate of 2 mV s^{-1} with a conventional 3-electrode setup. Figure 4.6a compares the IR corrected HER linear polarization current obtained on NbS_2, NbS_2/rGO and platinum–carbon (Pt/C) modified GC electrodes. The NbS_2/rGO surface showed a lower HER onset overpotential, η= 0.35 V whereas bare NbS_2 exhibited 0.42 V vs. the RHE (Pt/C showed 0.025 V). Following the hydrogen reduction onset, a sharp increment in current was observed on both surfaces and NbS_2/rGO achieved 10 mA cm^{-2} current density at 0.5 V vs. RHE whereas the NbS_2 surface required 0.55 V vs. RHE, showing the role of the conductive surface in the enhancement of catalytic activity. For a better electrocatalytic activity comparison, Tafel slopes (η= b log j + a) were derived (Figure 4.6c) from the linear region of the curves and a smaller Tafel slope value of 72 mV per decade on the NbS_2/rGO surface compared to NbS_2 (103 mV per decade) was found. From the slope values, it is quite difficult to ascertain the HER mechanism on the NbS_2 surface since the reaction on the TMD surface is not well established. However, there are three possible reaction steps proposed for the HER in an acidic medium; the first reaction step involves the discharge step (Volmer reaction), which is either followed by atom–atom combination (Tafel reaction) or ion–atom recombination (Heyrovsky reaction)[164, 165]. It is elucidated that if the Tafel slope is 30 mV per decade, the HER proceeds via the Volmer–Tafel mechanism or if it is

above 40 mV per decade, it follows the Volmer–Heyrovsky mechanism. Herein, the HER on both surfaces with Tafel slopes above 40 mV per decade suggests the involvement of the Volmer–Heyrovsky mechanism. Furthermore, the exchange current density (j_o) calculated from the intercept for NbS_2/rGO was found to be 3.16 *10^{-4} A cm^{-2} whereas, NbS_2 exhibited a value of 5.52 *10^{-5} A cm^{-2} suggesting the presence of more active sites on conductive networks.

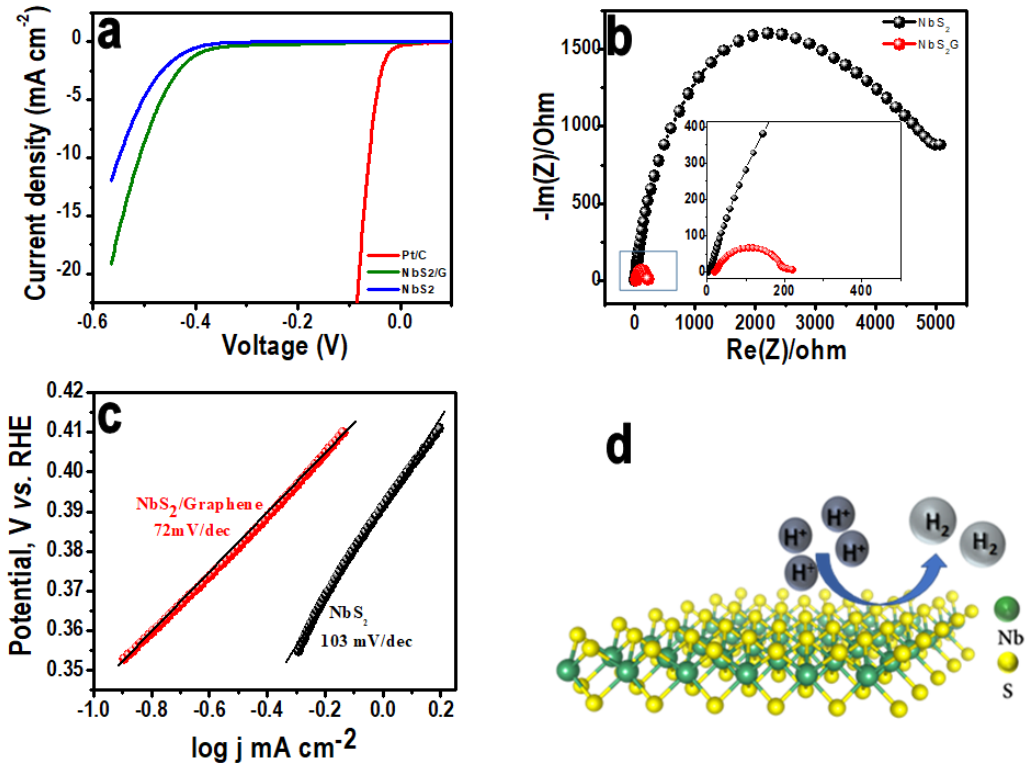

Figure 4.6. Electrochemical HER performance of NbS_2 nanoflakes compared with NbS_2/rGO. (a) Linear sweep voltammogram curves of NbS_2/rGO nanoflakes compared with NbS_2 and Pt/C. (b) EIS spectrum showing the change in R_{ct} for NbS_2/rGO when compared to NbS_2 nanoflakes alone (partial magnification of EIS spectra is shown in the inset). (c) Tafel plot for the HER performance of NbS_2 flakes and NbS_2/rGO (d) Schematic representation of hydrogen evolution on NbS_2 nanosheets.

To further corroborate the activity, interfacial charge transfer resistance (R_{ct}) values for NbS_2/rGO and the NbS_2 surface were measured using electrochemical impedance spectroscopy at open circuit potential (Figure 4.6b). The NbS_2/rGO shows a charge transfer resistance value of

200Ω whereas the NbS_2 electrode shows 5000Ω. This significant reduction in the R_{ct} of NbS_2/rGO clearly evidenced that incorporation of a conductive graphene support will aid in efficient charge transport. The higher activity and greater decrease in the charge transfer resistance of graphene supported NbS_2 (shown in the inset of Figure 4.6b) are ascribed to the solid electronic coupling between them, making more edge active sites available for catalysis. The schematic representation of the evolution of hydrogen on the basal plane of the NbS_2 nanoflakes is given in Figure 4.6d. Furthermore, the stability of the electrode materials is one of the key parameters in determining the efficiency of electrocatalysts. Cyclic voltammetric experiments were performed in the potential range between -0.3 and 0.2 V in acidic medium to evaluate the catalyst stability. Even after 500 cycles both the electrodes are able to retain their catalytic activity with a negligible decrease in the cathodic current (Figure 4.7). The stability of the NbS_2/rGO was again analyzed using the SEM technique and we found that both NbS_2 and graphene have a stable morphology even after 500 cycles. In Figure 4.7b (inset), we can see disintegrated NbS_2 flakes with rigid edges without any morphological changes along with rGO confirming the stable HER performance. This disintegration might have occurred due to the sonication assisted sample preparation of HER catalysts.

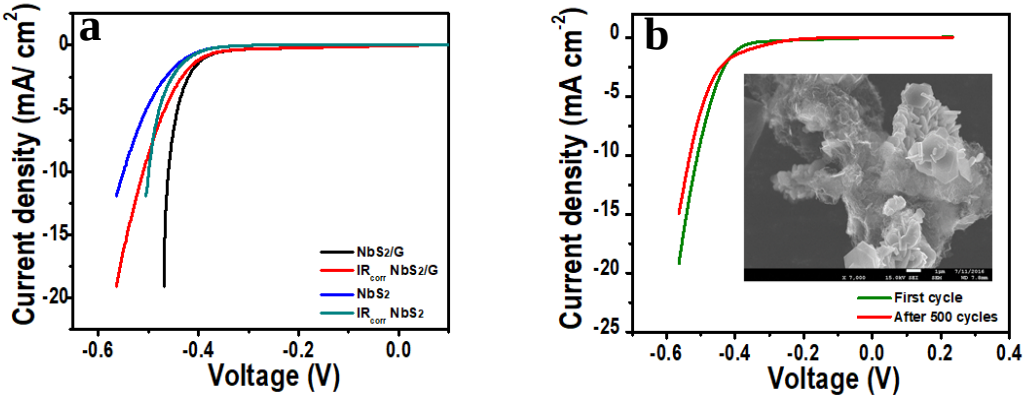

Figure 4.7. a. Comparison of LSVs of NbS_2 and NbS_2/G with and without IR correction. b. stability of NbS_2/G composite towards HER (inset : SEM image of NbS_2/G after 500 cycles)

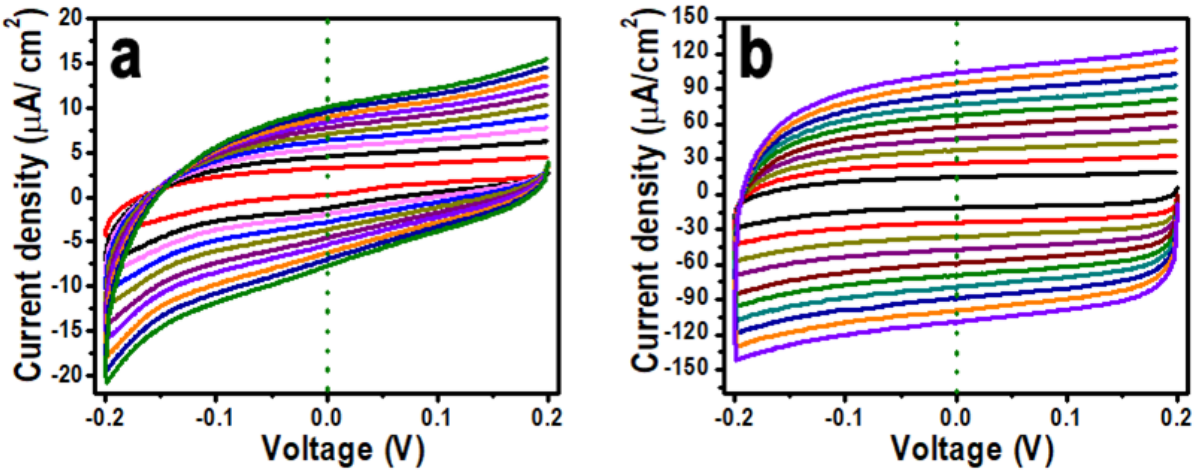

Figure 4.8. Electrochemical cyclic voltammogram of a) NbS_2 nanoflakes and b) NbS_2/G at different potential scanning rates.

Besides charge transfer kinetic measurements, to corroborate the superior HER performance of NbS_2/rGO compared to bare NbS_2, we estimated the effective surface area using a simple cyclic voltammetry method (Figure 4.8).

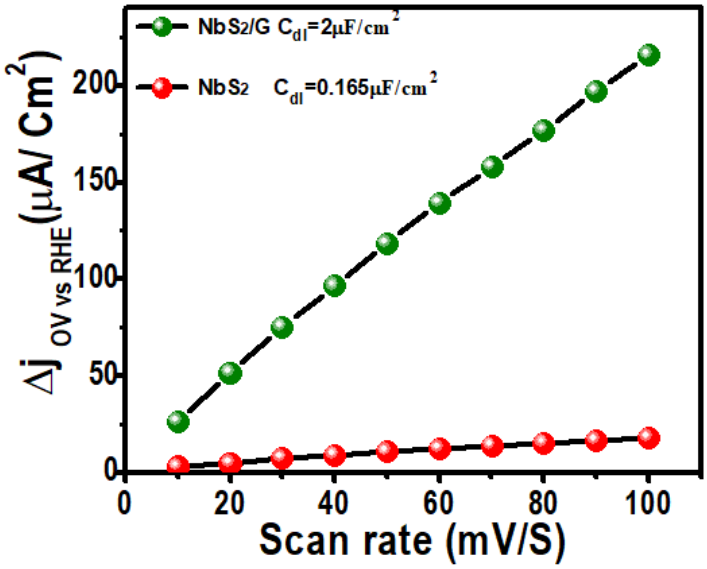

Figure 4.9. Linear fitting of the capacitive current differences against scan rates. The calculated double layer capacitances of both the NbS_2 and NbS_2/rGO electrodes are given.

From Figure 4.9, the slopes of the plot where half of the positive and negative current densities plotted against the different voltage scan rate give the electrochemical double-layer capacitances, C_{dl}. NbS_2/rGO exhibits a C_{dl} value of 2 mF cm^{-2}, larger than that of NbS_2 nanoflakes alone which reveals the enhanced surface area of the NbS_2/rGO composite through the rGO incorporation helping it to expose a more active area for better HER performance.

4.3.2 Lithium Sulfur Battery studies of NbS_2 nanoflakes and NbS_2/CC

The high catalytic activity of NbS_2 nanoflakes makes them a potential candidate for LiPS adsorption. Towards this, we loaded the carbon cloth with this catalytically active NbS_2 nanoflakes through the filtration method. To expose the preferable sites on the catalyst surface, the coalesced NbS_2 nanoflakes were undergone sonication to disintegrate into single flakes. These morphological changes are analyzed using SEM and are shown in Figure 4.10. Figure 4.10a shows the SEM image of as synthesized NbS_2 nanoflakes which are found to be thin layered with definite edges which can be associated with the absence of restacking. However, the bunches of NbS_2 flakes were got fragmented into single flakes upon sonication in water: ethanol (4:3) mixture, as shown in figure 4.10b. Single individual flakes can make more active surfaces available for LiPS adsorption thereby improving the overall redox kinetics. These fragmented flakes were deposited uniformly through the filtration method which is shown in figure 4.10d and the smooth surface of CC fibers can be seen is in SEM image of bare CC (figure 4.10c). The NbS_2 deposited CC was taken further for electrochemical Li-S battery measurements.

To reveal the electrochemical performance of the NbS_2/ CC composite, bare NbS_2 and bare CC, galvanostatic charge discharge was carried out by fabricating 2032-coin cells using them as cathode vs. metallic lithium as anode.

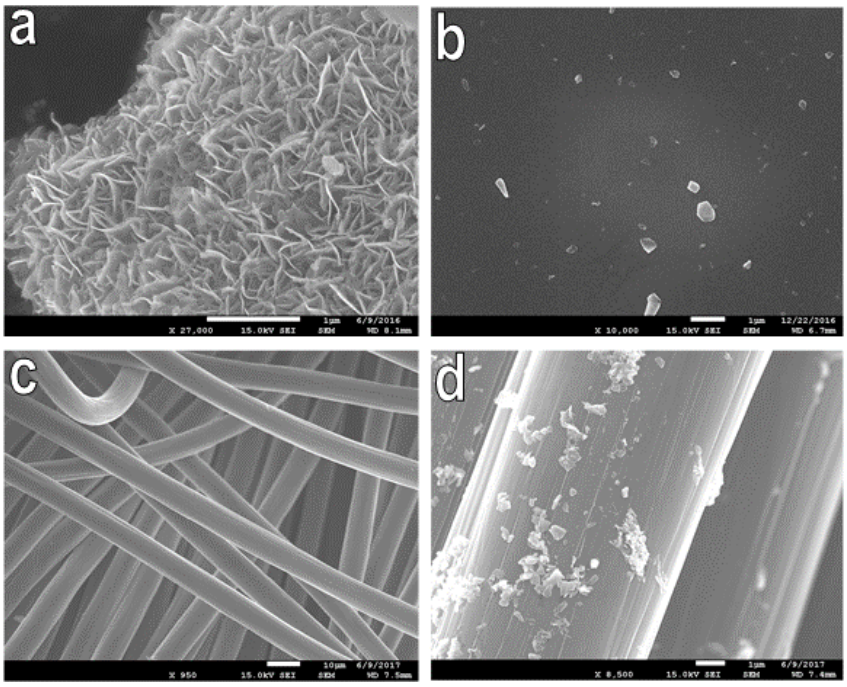

Figure 4.10. Morphological characterization of NbS_2 nanoflakes, NbS_2/CC: (a) SEM image of NbS_2 flakes, (b) the fragmented single NbS_2 nanoflakes after sonication process, (c) SEM image of bare CC, and (d) fragmented NbS_2 flakes on CC after deposition

Figure 4.11 a and b shows the charge discharge behavior of these NbS_2/CC and bare CC electrodes at a current rate of 0.1C (based on sulfur mass in the cell) respectively. The discharge curves showed the typical discharge plateaus at 2.35 V and 1.97 V corresponding to the formation of soluble higher order polysulfides and their dissociation to low order insoluble Li_2S_X respectively. During the charging process, a reversible conversion reaction occurred at 2.3V, which can be assigned to the transition of lower LiPS to high order PS. There were no significant changes observed in the charge discharge profiles of the NbS_2/CC and bare CC electrodes. NbS_2/CC composite with its improved conductivity along with the ability of NbS_2 to catalyze the LiPS during charge discharge helped in excellent reversibility and improved capacity, which took them a step ahead of bare NbS_2 and carbon electrodes. The NbS_2/CC electrode exhibits a stable charge-discharge capacities of 810 mAh g^{-1} at a C-rate of 0.1 C whereas the bare CC showed a

capacity around 600 mA h g^{-1} over 25cycles, which exposes the strength of catalytic NbS_2 on CC electrode to adsorb and increase the LiPS redox reaction kinetics along with the improved conductivity from CC. Figure 4.11c shows the cyclic life of both the electrodes and confirms the capacity retention is good for both which supports the need for a conducting matrix for enhanced electrochemical performance.

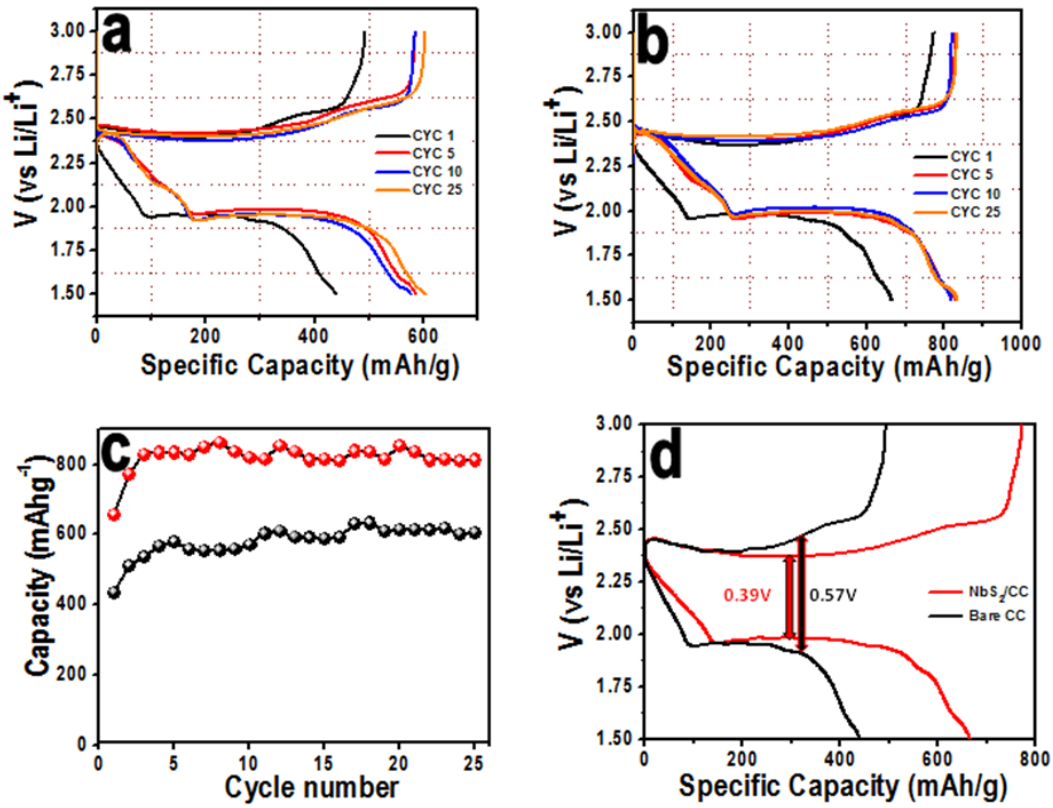

Figure 4.11. Electrochemical behavior: (a) and (b) charge–discharge profiles of bare CC and NbS2/CC at 0.1 C rate, respectively, (c) cycling study of electrocatalytically active NbS2/CC and bare CC as working electrode versus Li/Li^+ with catholyte consisting of 0.2 M Li_2S_8 at 0.1 C rate, and (d) comparison of charge discharge curves of NbS_2/CC and bare CC for analyzing the polarization behavior.

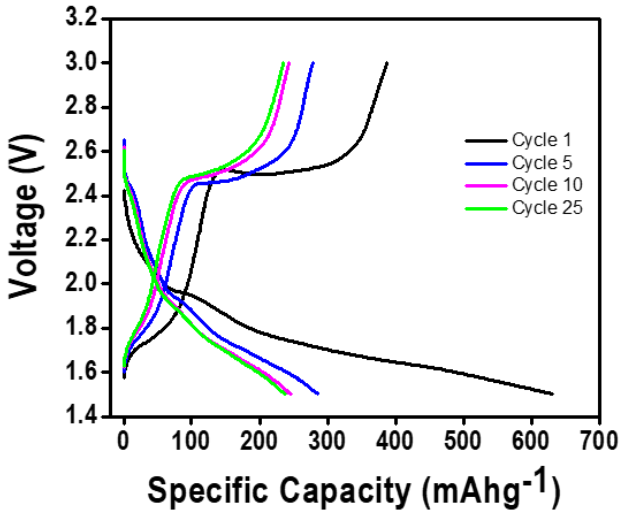

Figure 4.12. Charge–discharge profiles of bare NbS_2 at 0.1 C rate

Figure 4.12 shows the charge discharge behavior of bare semiconducting NbS_2 flakes which undergo huge capacity fade upon cycling explaining the inability to hold the PS, its reversible conversion (from liquid LiPS to solid and vice versa). Notably, we can understand the effect of conducting surface towards PS adsorption, mass transport and electron transfer capability etc. Also, the excellent coulombic efficiency can be seen for the NbS_2/CC electrodes when compared with that of CC alone (Figure 4.13).

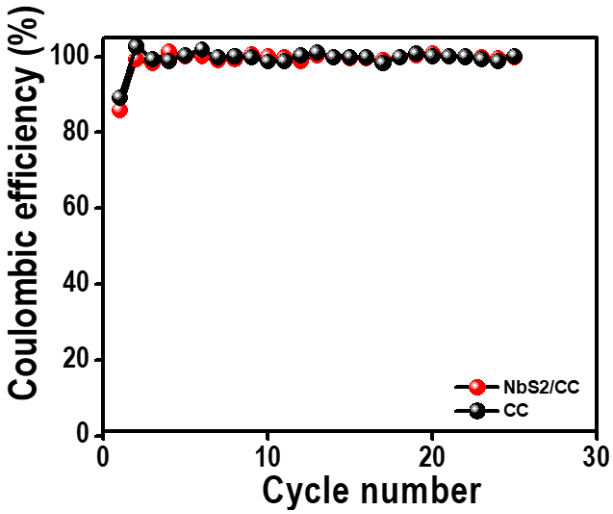

Figure 4.13. Coulombic efficiency of NbS_2/CC and bare CC electrodes

The potential difference between the charge discharge plateaus reflects the polarization of the electrode which in turn related to the reaction kinetics of the whole system. Here the potential difference between the plateaus is measured and found that the potential difference becomes larger for bare carbon, i.e 0.57 V when compared to that of NbS_2/CC (0.39 V). This low polarization suggests better reaction kinetics which is due to the improved electrical conductivity and efficient contact between the NbS_2 on CC.

This synergistic effect of the catalytic and conducting surface towards better PS adsorption and kinetics are reconfirmed with AC impedance measurements. Electrochemical impedance of both bare CC and NbS_2/CC was measured to confirm the enhanced electrical conductivity, structural stability and Li ion diffusion as we designed our approach (Figure 4.14a). Clearly, the presence of CC with NbS_2 nanoflakes contribute towards the improved electrical conductivity, R_e from 136 Ω (bare CC) to 93 Ω. Also, from the impedance data, it can be inferred that the porosity and structure of CC is well maintained.

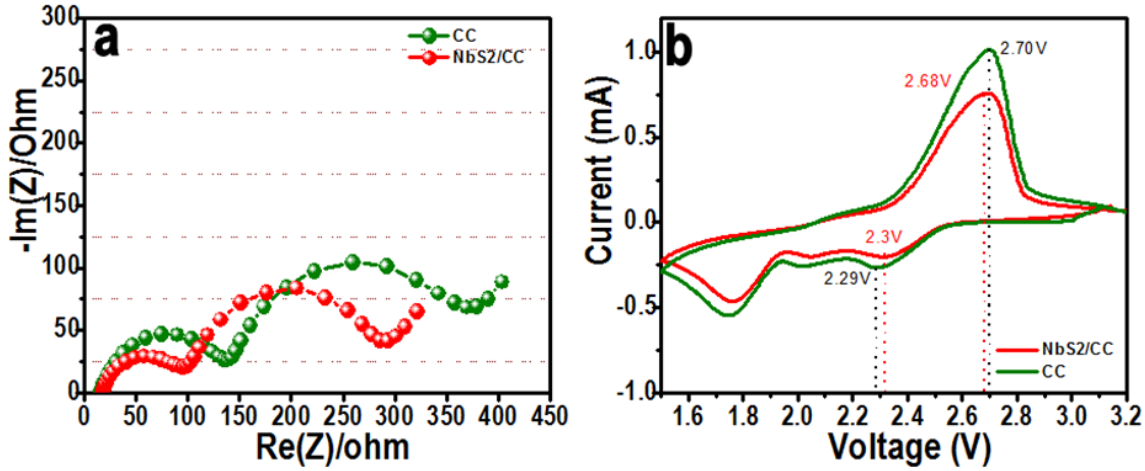

Figure 4.14. Electrocatalytic properties: (a) AC impedance measurements of NbS_2/CC and bare CC electrode and (b) comparative cyclic voltammograms of NbS_2/CC and bare CC as a working electrode versus Li/Li^+ in 0.06 M catholyte solution at scan rate of 0.1 mV/s

Again, electrocatalysis of LiPS redox activity at different electrode surfaces was measured using potentiodynamic cyclic voltammetry technique. From figure 4.14b, LiPS reduction peak potential of NbS_2/CC was found to be 2.3V which gets anodically shifted from 2.29V when compared to that of carbon. In addition, the anodic and cathodic peak potential difference of each catalytic surface gives major information regarding the advantage of having an electrocatalytic surface towards polysulfide redox activity. The reduction in the peak potential difference values minimizes the cell polarization, increases the rate capability and cycle life. Here, the difference between anodic and cathodic peak potentials for NbS_2/CC was 380 mV, which is lower than that of Carbon (410 mV) attributing towards a catalytic nature of NbS_2/CC. Similarly, LiPS oxidation peak potential was cathodically favored for NbS_2/CC (2.68 V) while compared with carbon (2.7 V) which again confirms the influence of catalytic surface towards better polysulfide catalysis. The CV derived parameter like peak potential difference clearly attribute to the surface dependency on LiPS redox kinetics[114, 131]. Polysulfide interaction with metal sulfides purely depends on the charge transfer mechanism rather than the direct bond formation. The unsaturated dangling bonds present in the edge sites of NbS_2 will interact more with the polysulfides which will allow the polysulfide redox reactions on their surface. In the earlier chapter, we have proved that the metal sulfide can act as a catalyst that enhances the polysulfide adsorption, accelerates the liquid to solid PS conversion and improves oxidation kinetics of Li_2S[28, 29, 166]. Thus, aqueous PS redox can be activated by the catalytic surface which experimentally proves our concept of the surface involved electrocatalysis driven sulfur redox process in the Li−S battery system.

4.4 Conclusion

In this chapter, we demonstrate an easy and novel route synthesis of NbS_2 using Nb powder and S sources under a controlled atmosphere. The NbS_2 nanoflakes were well-characterized and

found with 3R polymorph with rhombohedral crystal structures. The optical bandgap was measured and found to be ~1.49 eV confirming the semiconducting nature of 3R-NbS_2. With its flakey morphology and a large number of exposed active sites along with the electrical coupling with the graphene, the NbS_2-graphene hybrid showed an enhanced HER activity with a small onset potential ~0.15 eV, Tafel slope of 84 mV/decade, and a large cathodic current. Thus, this novel one-pot synthesis of an NbS_2/G hybrid composite opens the potential of NbS_2 as a good electrocatalyst. Also, we have successfully explained the role of conducting and catalytic surfaces for improving the lithium-sulfur redox kinetics while effectively adsorbing the LiPS onto them. Thus, the catalytic surface holds the LiPS from dissolution, reduces the redox overpotential and improves the diffusion properties of PS anions, which ends up in high capacity gaining and enhanced cell reversibility. The improvement in conductivity through the incorporation of carbon cloth along with the catalytic behavior of NbS_2 helped to give a stable capacity of 810 mAh g^{-1} for NbS_2/CC electrodes. Impedance analysis supported the results by exhibiting a lower charge transfer resistance attributed to the better conductivity of the electrode.

CHAPTER 5 IONIC LIQUID CRYSTALLINE ELECTROLYTE TO SUPPRESS DENDRITE GROWTH IN Li METAL BATTERIES: AN EFFECT OF ANISOTROPIC MASS TRANSPORT

5.1 Background and Motivation

Research on rechargeable Li metal-based batteries has been amplified as Li metal can deliver a specific capacity of ∼3862 mAh g^{-1}, which positions it as a promising component in portable energy devices, electric vehicle systems, robotics and other grid storage technologies[12, 167-169]. However, the demand for portable energy storage devices with high energy density remains a challenge. In this scenario, Li-O_2 and Li-S batteries are capable of delivering ultra-high energy densities and considered as next generation energy storage systems[170]. Unfortunately, the intrinsic issues instigated by electrode/electrolyte interactions causing problems in terms of safety and cyclability in these batteries, hindering their practical implementation in certain applications[14, 171]. In particularly, the heterogeneous anode materials can lead to the formation of dendrites on their surface, which has a longstanding negative affect on the Li battery (LiB) performance in terms of safety and cycle life[73, 172]. The effects on battery cycle stability can be due to increased interfacial resistance and poor Coulombic efficiencies which lead to cell short circuiting, cell failure, and explosion[73, 173]. Hence, prevention of dendrite formation is necessary to employ Li metal as an anode in batteries.

At the Li metal/electrolyte interface, Li-ions will react with electrons during the charging process and electrochemically get reduced and deposited onto the Li metal anode[18, 174]. Impurities and protrusions on the anode surface will cause the nucleation of dendritic Li structures with faster kinetics and inconsistent deposition[175]. Li mass transport is the main factor for the dendrite growth, which depends on many physical processes such as advection, ion migration and reactions at the electrode / electrolyte interface[176, 177]. Large variations in the Li+ ion concentration gradient across the surface of the anode also appear to encourage the deposition and

Li dendrite formation. Researchers have taken tremendous efforts to suppress dendrite growth through various techniques such as electrode modification, controlling the Li morphology, designing different cell configurations by introducing protective layers and conducting scaffolds, implementing different kinds of electrolytes including solid-state, gel electrolytes, and more[172, 173].The limited success of these strategies call for a better approach towards dendrite suppression. Recently, theoretical studies based on liquid crystals propose that their anisotropic properties can control the Li-ion mass transport and paves the way for dendrite growth suppression[174]. Also, modelling and simulation studies recommend that an electrolyte that enables high ionic conductivity and lithium transference number (tLi+) near to unity at the reaction sites can reduce the concentration gradient and thereby the dendrite growth[178, 179]. Among several electrolytes explored, Ionic liquid Crystals (ILCs) are promising due to their exceptional efficient 1D, 2D and 3D anisotropic ion-conduction pathways and have the capability to form robust solid electrolyte interfaces (SEI) with reduced resistance because of their liquid-like mobility[180-185]. Recently, rod like ILCs consisting of cyclic carbonate derivative moiety and Lithium bis (trifluoromethylsulfonyl)imide (LiTFSI) have been studied in Li-ion batteries[186]. However, till date, there are no reports on how an anisotropic property of ILC could influence dendrite growth on Li anode.

5.1.1 Liquid Crystals and Ionic Liquid Crystals

Liquid Crystals (LCs) are a state of matter with unique combinations of flow-like liquid and long-range orderly oriented molecules [187-189]. The driving force to form such an unusual liquid-crystalline phase (mesophase) is interactions between the dissimilar molecules or charged species in a regular manner (dipole-dipole interactions, van der Waals interactions, π-π stacking etc.)[190, 191]. LCs are made of rigid aromatic core with flexible aliphatic tails. The shape of the

liquid crystalline molecule can determine the type of mesophase formed. The most of the known mesogens are rod-shaped or calamitic (Figure 5.1a), others are disc-shaped or discotic mesogens (Figure 5.1b) and bent-core or banana-shaped (Figure 5.1c). the molecular anisotropy is the key driving forces or factor for mesophase formation[192]. Symmetry of mesophase, the molecular arrangement can be of two orders : orientation and position order, which determines the type of mesophase. Accordingly, there are **nematic (N)** phase where molecules show orientational order, **smectic (Sm)** and **columnar (Col)** phases that shows both orientational order and long-range positional in one or two dimensions, respectively[187, 191-193]. Phases with both orientational order and 1D positional order along the director ñ are known as smectic phases which have layered mesophases that differ in the in-layer molecular arrangement. All these mesophases have two factors in common and they are order and anisotropy. The variation in these common factors make them a prominent candidate in many applications in the field of displays, actuators, sensing, micro-optics and various other fields[193].

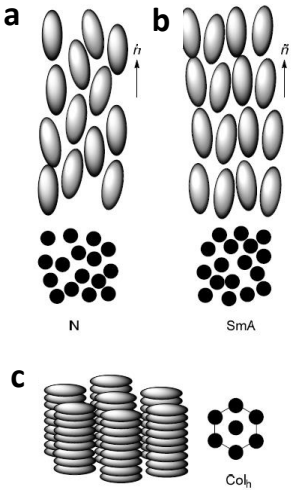

Figure 5.1. Schematic representation of LC phases[192].

Moreover, such a class of materials unveils ionic character with charge transport properties like ionic liquids. Hence, LCs known as ionic liquid crystals (ILCs) which exhibit synergistic properties of liquid crystals (anisotropy) and ionic liquids (fluid-like flow) have gained tremendous research attention in several applications. including energy storage devices[182]. Ionic liquids (ILs) and Ionic liquid crystals (ILCs) have attracted much attention in recent years because of their potential capability to make a breakthrough in electrochemical device field. Ionic liquids are the molten salts with a low melting point (below 100°C) and are composed of bulky organic cation and weak inorganic or organic anion[194]. They are brilliant properties like negligible vapor pressure, high thermal stability, high ionic conductivity, wide electrochemical stability window and are nonflammable [191, 193]. Being made of ion pairs with non-covalent interactions, ILs will make them suitable for many fascinating applications. They have been used as an interesting class of alternative electrolytes for existing energy storage devices. Typically, ILs contain the bulky asymmetric cationic centers like nitrogen, oxygen, sulphur, phosphorous atoms and weakly coordinating counter anions, such as halides, hexafluorophosphate (PF_6^-), tetrafluoroborate (BF_4^-), bistriflimide $[(CF_3SO_2)_2N]^-$, etc. as shown in figure 5.2. Common cations such as imidazolium, pyridinium, pyrrolidinium, and piperidinium are well investigated[193]. Structure of ILs determine its temperature limits, functional properties, and self-assembly ability. Cations, anions, and side chain of ILs contribute towards their self-assembly process. The organic cations and anions present in ILs are stabilized by resonance with the highly delocalized charges in them. Compared to ILs, ILCs with synergistic properties of both ionic liquids and liquid crystals, makes them more viable for flexible electronics as safe electrolyte. The important parameters like the type of cationic core, the length and nature of a substituted aliphatic chain and the counter ion determine the type of ILCs and their properties. Mesophase can be induced in ILCs through the

response to the thermal, concentration, potential, magnetic, light, mechanic stimuli etc. And this is accompanied with the formation of ion conducting 1D, 2D or 3D channels due to the controlled self-assembly. Ionic conductivity showed by ILCs has received significant in day today research and various applications. With the temperature increase, 3D ordered crystalline phase transforms into 2- or 1D ordered LC phases, where more freedom for the transport of charge carriers are guaranteed resulting in higher conductivity. There are temperature and concentration depended LC phase formation, and those class of LCs can be categorized as thermotropic and lyotropic LCs respectively. The enhancement in with temperature is attributed to the thermotropic phase transitions which further envisioned from the temperature-dependent variation of charge diffusion coefficient (D) values. Likewise, lyotropic liquid-crystalline phase formation is studied through conductivity measurements and rheological analysis[195].

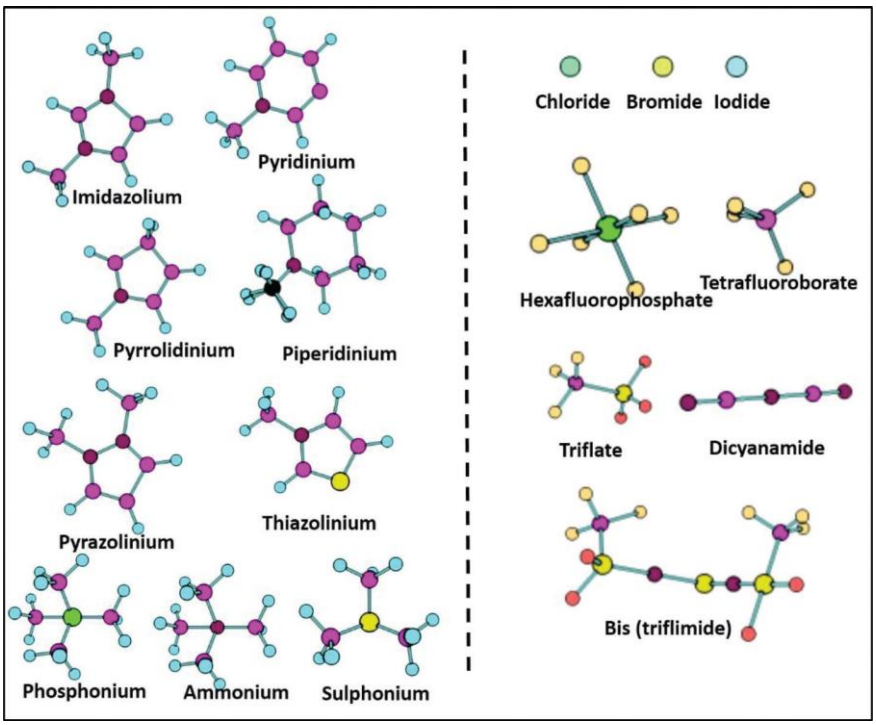

Figure 5.2. common cations and anions in ILs[195].

A wide range of thermotropic liquid crystalline (mesophase) materials have been reported primarily inspired by results from classical LCs and ILs. Firstly, alkali metal soaps with halides were studied[196], followed by N-alkylammonium[197], N-alkylimidazoilium and *N*-alkylpyridinium salts which have also been found to exhibit thermotropic liquid crystalline behavior[198-200]. The majority of early studies have heavily focused on concentrated halide species as anions (Cl^-, Br^- and I^-) with some others, notably metallomesogens $[MCl_4]^{2-}$ (M=Co, Ni), $[ZnBr_4]^{2-}$, $[C_{12}H_{25}OSO_3]^-$ and tartrates[201-204] also considered. As far as the cation is concerned, imidazolium and pyridinium-based materials have been presented to be versatile for obtaining self-assembled ion-conduction pathways and hence projected their potential application in energy devices[191, 205-208]. Several attempts have been made to induce and stabilize mesophases of ILCs by modifying the structure of cations[208]. Further, new class of ILC electrolyte systems have been identified with 2D pathways for I^-/I^{3-} redox couple transportation consisting of a carbonate-based mesogen and an IL that self-assembles into a two-component LC. ILCs have also been attempted for use as an electrolyte for Li-ion batteries[186]. ILCs have great potential and are on-par with other similar electrolytes based on polymeric, solid inorganic materials as backbone and also conventional room temperature ILs (RTILs). The polymer and inorganic solid electrolytes possess sufficient rigidity and anisotropic nature to effectively prevent lithium dendrites formation, but poor ionic conductivities and large electrode-electrolyte resistance make them incompatible for Li batteries. RTILs, though they have better ionic conductivity than solid electrolytes, they fall short on anisotropic properties to prevent dendrites. On the other hand, ILCs are exceptional in their efficient 1D, 2D and 3D anisotropic ion-conduction pathways and capability to form electrode-electrolyte interfaces (SEI) with reduced resistance because of their liquid-like mobility. Among the different phases of ILCs, mesophase (co-existence of crystallinity

and liquid like-flow) has lower activation energy for ionic mobility than that of the isotropic phase. This represents that the orderly arranged LC molecules provide efficient conduction pathways and definite pores for migration of ionic species. Therefore, achieving mesophase at ambient temperatures with sufficient ionic conductivity is a fundamental aspect to ILCs applications in Li batteries.

Here, we develop a novel imidazolium based thermotropic ionic liquid crystalline material derived from a long-alkylated phenol, 3-Pentadecyl phenol (3 PDP). The synthesized ILC was characterized, revealing its bent core structure with self-assembled molecules exhibiting high ionic conductivity at both RT and elevated temperatures. We report that these ILCs with their anisotropic properties can act as a pseudo separator-cum-electrolyte and control the Li ion concentration gradient at the electrolyte-anode interface, which helps in controlling Li ion mass transportation and thereby suppressing dendrite growth. To complement the experimental results, numerical simulations were performed to explore the mechanism of dendrite suppression based on the material properties of the ILC electrolyte.

5.2 Experimental Section

5.2.1 Synthesis Methods

5.2.1.1 Preparation of 1-(12-bromododecoxy)-3-pentadecyl benzene (BDDPB)

3g of 3-pentadecyl phenol is accurately weighed out in a round bottomed flask containing 1g of 1, 12-dibromododecane. Then the mixture is stirred magnetically for 1 hour at 70 ˚C for the complete dissolution to make a pure phase orange colored composite. KOH (1g) is weighed, powdered, and added to the reaction mixture to be continuously stirred for 48 hours. The progress of the reaction is monitored every 12 hours by conducting Thin Layer Chromatography (TLC) using 5% ethyl acetate in hexane. After confirming the completion of the reaction, the solid residue

is filtered off using a filtration set up and then purified by passing through a silica column with different weight percentages of ethyl acetate in hexane solution. The product is then Rota vapored to get a slight yellowish powder and used for the second step.

5.2.1.2 Preparation of 3-(12-(3-pentadecylphenoxy) dodecyl)-1-methylimidazole_3-3ium hexafluoro-phosphate (PDDMHP)

1g of BDDPB is added to 2g of 1-methyl imidazole at 0° C under vigorous stirring conditions and then further heated to reflux at around 75° C for 48 hours, then cooled to room temperature. The solid residue is washed with diethyl ether several times to remove unreacted reactants from the compound. The white solid precipitate is collected and dried under vacuum to obtain the product in good yield. Bromide salts are highly moisture sensitive, so to make them environmentally stable they are diluted with distilled water and further converted into corresponding hexafluorophosphate salt by a simple anion metathesis reaction using a large amount of sodium hexafluorophosphate. An aqueous solution of bromide salt is stirred magnetically for 12 hours with a high molar solution of sodium hexafluorophosphate, which is added drop wise. The ILC with hexafluorophosphate salt is precipitated and later filtered and washed with water to remove unreacted bromide salts and excess sodium salts. It is dried under vacuum for 12 hours to obtain PDDMHP in dry form. Thus, overall synthesis procedure involves O-Alkylation of 3-PDP followed by quaternization with 1-methyl imidazole to synthesize this imidazolium based ionic liquid crystals.

5.2.2 Characterization of ILC electrolytes

ILC electrolytes were characterized for their ionic conductivity and anisotropic nature using Electrochemical impedance spectroscopy (EIS) and Differential scanning calorimetry (DSC) analysis. ^{1}H NMR was carried out to confirm the formation of targeted LC. Further, wide angle X-ray diffraction (WAXD), small angle X-ray scattering (SAXS) and polarizing optical

microscopy (PLOM) studies were used to determine the crystal data and orientation of additive containing LC.

5.2.3 Anisotropy conductivity measurements

Anisotropic ionic conductivity was measured in both directions parallel and perpendicular to the self-assembled layers using the alternating current impedance technique. Anisotropy in ionic conductivity of LCs was analyzed by a pair of comb shaped gold electrodes (Cell A) and a pair of Indium tin oxide (ITO) plates (Cell B). First, gold was sputtered onto a glass plate in a comb shape by leaving a 1mm distance between the teeth and a sidewise width of approximately 0.3 mm. The thickness of the sputtered gold was about 0.8 um. The compound mixtures were filled in both the cells and their orientation were confirmed by a polarizing microscope. Ionic conductivity parallel to the oriented layer was measured using cell A, and the one perpendicular to the oriented layer was obtained by using cell B. In Cell B, a pair of indium tin oxide (ITO) electrodes were separated with a thickness of 30 um using a Teflon spacer. In both cases, homeotropic alignment of sample mixtures were observed.

5.2.4 Interfacial Mesoscale Modeling

The numerical simulations use a multiphase reactive transport model based on smoothed particle hydrodynamics (SPH) which is a Lagrangian particle-based method. SPH was first developed for astrophysical problems and has been adapted to solve fluid dynamics, multiphase flows, and reactive transport by discretizing the continuity equations[174, 209-211]. The model used for the studies presented in this work are based on previous modeling of dendrite growth[174, 212, 213]. The details of the model equations and implementation can be found in Tan et al 2016[174]. This model was developed using an open-source software called Large-scale Atomic/Molecular Massively Parallel Simulator (LAMMPS)[214].

5.2.5 Electrochemical measurement

The electrodeposition of Li in the LC based electrolytes using galvanostatic cycling of Li| LiTFSI-LC| Li symmetric lithium cells in which lithium striping process was carried out under constant current which resembles conventional Lithium metal battery. The symmetric cells were fabricated using CR2032 cells with Li electrodes of 10 mm in size on both sides of the separator made of Teflon with a hole of 1.6 mm diameter at the center facilitating the ionic mobility between the Li electrodes without allowing any other side reactions. The prepared novel ILC electrolyte with optimized amount of LiTFSI was filled in the hole of separator. Symmetric cell cycling from -1 to 1 V was conducted on Arbin electrochemical workstation with a current density 0.1 $mAcm^{-1}$ at 60 ^{o}C. The charging and discharge times were restricted to 3 hours. The control experiment with electrolyte containing LiTFSI and PC were also carried out for comparison studies. Electrochemical impedance spectroscopic (EIS) studies were conducted in the frequency range 1 Hz to 1 MHz using a Bio-logic electrochemical workstation.

5.3 Results and discussion

Details pertaining to the synthesis of 3-(12-(3-pentadecylphenoxy) dodecyl)-1-methylimidazole_3-3ium hexafluoro-phosphate (PDDMHP) is explained and provided in the supporting information. Formation of the targeted compound is schematically represented in scheme 5.1 and confirmed by Proton Nuclear magnetic resonance (^{1}H NMR) analysis.

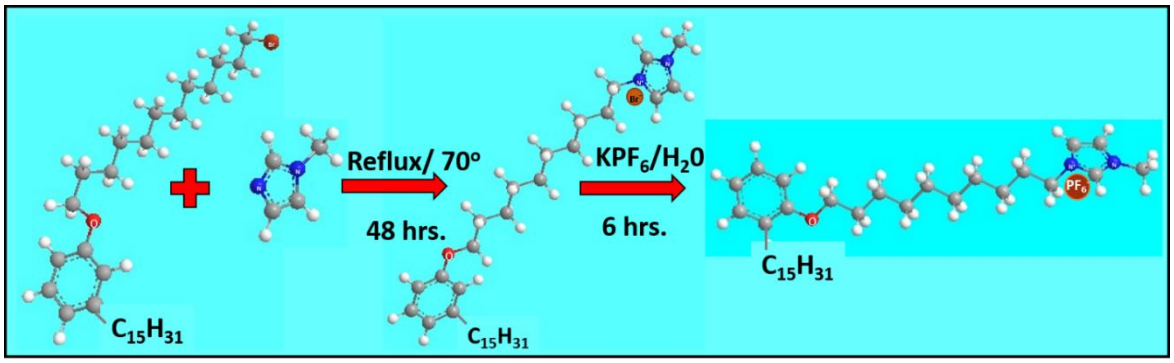

Scheme 5.1 Schematic representation of synthesis of thermotropic ILC, PDDMHP.

In the NMR spectrum (Figure. 5.3) of PDDMHP, the triplet at a δ value of 0.9 ppm is corresponding to the terminal methyl protons of the pentadecyl chain. Peaks in between 1 and 3 ppm are ascribed to the methylenic protons present in the pentadecyl side chain and dodecyl spacer chain. Methylenic protons present adjacent to the electronegative O^- and N^- atoms give characteristic triplets at 3.9 and 4.2 ppm, respectively. A sharp singlet at 3.8 ppm is due to the protons of the methyl groups attached directly to the imidazolium ring. Aromatic protons in the phenyl ring give characteristic peaks in between 6.8 and 7.2 ppm, whereas the protons in the imidazole ring produce peaks at 7.8 and 9.2 ppm. Thus, ^{1}HNMR analysis clearly confirmed the formation of an imidazolium based ionic liquid crystal.

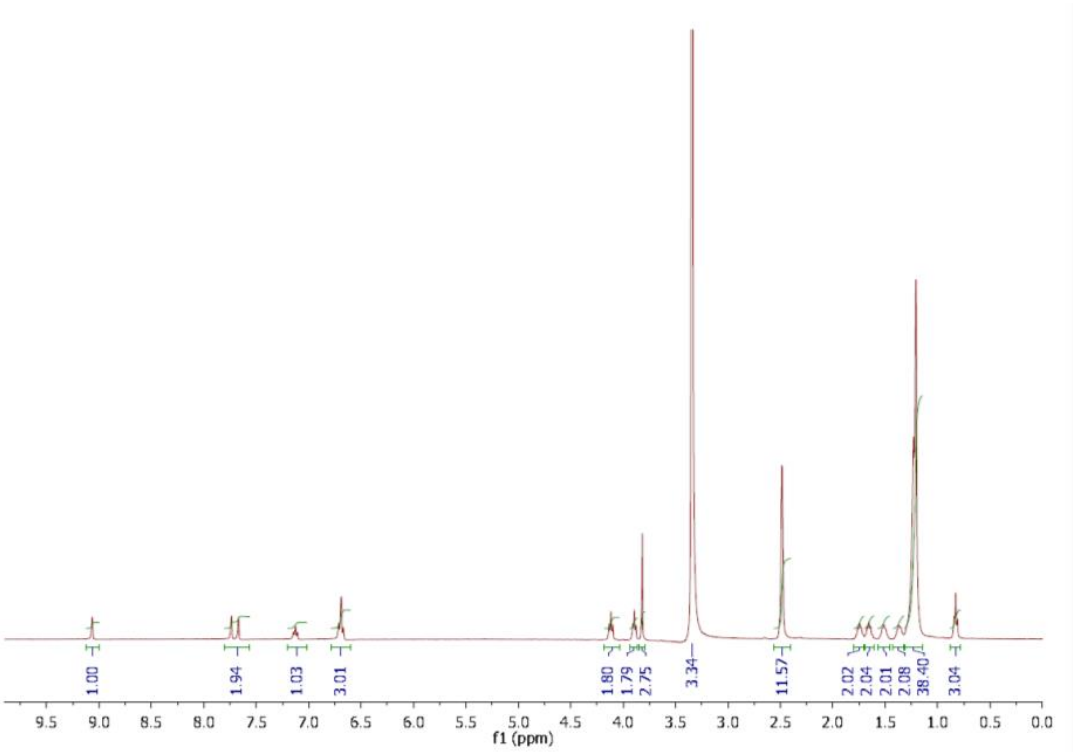

Figure 5.3. NMR Spectrum of PDDMHP

Further, Fourier transform infrared spectrometer (FT-IR) analysis was carried out to confirm the functional group present in the as synthesized compound and the corresponding

spectra is shown in Figure 5.4. The presence of an alkyl chain having symmetric and asymmetric C-H stretching vibrations, which can be observed as multiple peaks in the range of 2800 – 3000 cm^{-1}. The peaks from 3000 to 3200 cm^{-1} correspond to C-H vibration modes of aromatic rings. C-C stretching, and C-N bending vibrations can be observed from the peaks in the range of 1600 – 1585 cm^{-1}. The peak at 1455 cm^{-1} contributes to C-H alkyl deformation, where a peak at 1189 cm^{-1} indicates the C-N stretching vibration. C-O-C stretching of alkyl aryl ether is visible with the presence of a peak at 1158 cm^{-1}. Finally, P-F stretching vibrations of PF^6 anion is observed at 820 cm^{-1}.

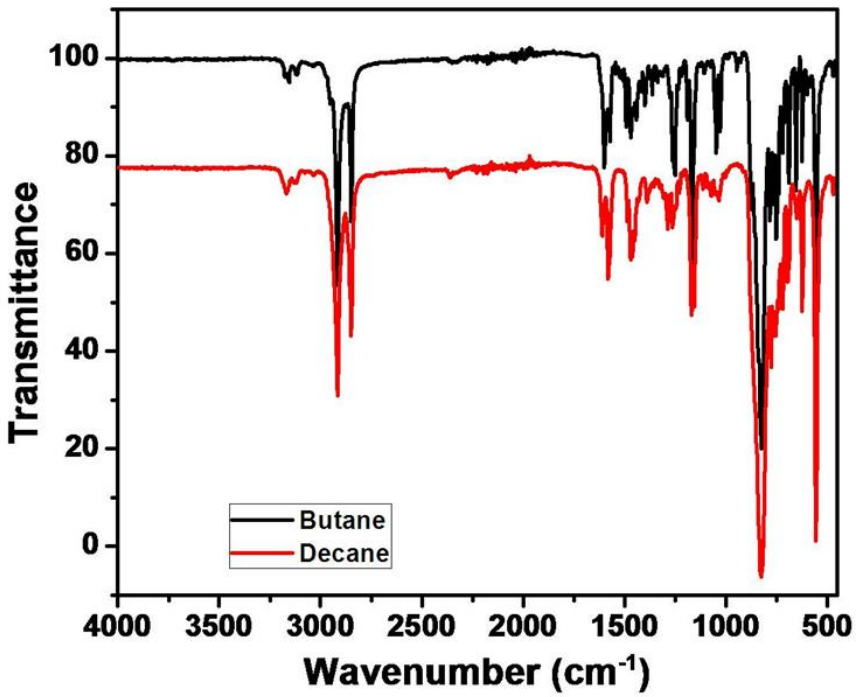

Figure 5.4. FT IR spectrum of PDDMHP.

To validate the synthesized imidazolium based ILCs exhibited a thermotropic mesophase, we have performed differential scanning calorimetry (DSC) thermograms measurements. To

analyze the thermotropic phase transition of the synthesized compound, the sample is heated and cooled from -20 to 200 ^{o}C. On a heating ramp, PDDMHP displays a transition from crystalline to liquid crystalline phase, i.e. Smectic A (SmA) at a temperature of 55 ^{o}C and an isotropic phase at 165 ^{o}C (Figure 5.5a). On cooling from the isotropic melt, PDDMHP transforms to smectic A phase again at 165 ^{o}C and returns to its crystalline nature at 25°C. These features can be observed clearly in the DSC spectrum shown in Figure (5.5a). The phase transition temperatures and enthalpy changes of PDDMHP are derived from DSC traces and are listed in Table 5.1. Though the precise phase cannot be identified using DSC, the level of enthalpy change involved at the phase transition gives an estimate of the type of phase involved[215, 216]. The structural changes, which occur during the temperature variation, reflect the enthalpy changes. The enthalpy changes of liquid crystalline to an isotropic liquid transition indicate that the LC phase is smectic A (SmA)[217].

Phase transition	Phase transition temperatures	ΔH (kJ/mol)
Cryst - SmA	55 °C	65.69
SmA - Iso	165 °C	0.72

Table 5.1. Phase transition temperatures (°C), enthalpy changes (kJ/mol) of the PDDMHP

Furthermore, the type of mesophase that the compound exhibits is confirmed by using optical polarizing microscopy in conjunction with DSC analysis. The images (Figure 5.5b) are taken while cooling from the isotropic phase starting at 165 ^{o}C. During cooling, the randomly aligned or disordered ionic liquid crystal molecules are aligned together to form supramolecular organized liquid crystalline phases by several noncovalent interactions such as electrostatic, ionic assembling and Van der Waal's interactions, helping to form a mesophase in the compound with different extents of order. The images show that liquid crystals are in the smectic A phase at temperatures ranging from 55 to 165 ^{o}C and are shown in Figure (5.5b).

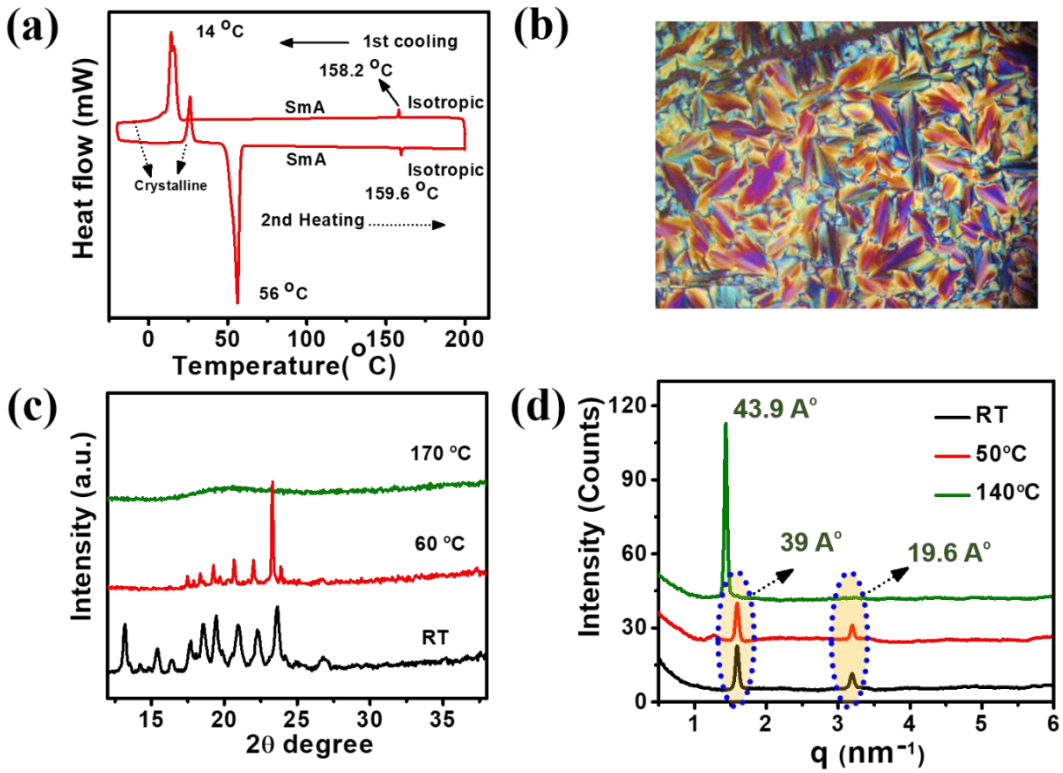

Figure 5.5. (a) DSC heating and cooling scans of PDDMHP showing thermotropic behavior. (b) PLOM images showing the SmA phase of the PDDMHP. (c) WAXD patterns of PDDMHP at different temperature (d) SAXS pattern of PDDMHP.

Wide angle X-ray diffraction (WAXD) was carried out at different temperatures to examine the phase transformation of the synthesized compound and is shown in Figure 5.5c. At room temperature, PDDMHP was highly crystalline due to the strong ionic interactions between the charged counterparts and long alkyl chains. PDDMHP was heated to form amorphous phases without any characteristic peaks, showing a complete transformation to the isotropic phase above 170 °C. On cooling from the melt, the quasi-crystalline nature reappeared with a few of the reflections at a temperature below 100 °C, confirming the recrystallization of the melt to an anisotropic liquid crystalline phase. The high intensity peaks at the LC and crystalline phases are attributed to the stacking of imidazolium cations. Emergence of moderately crystalline peaks when

the isotropic melt is cooled below 100 ºC could be corroborated to the formation of the anisotropic LC phase. This observation is in well agreement with the DSC analysis. Thermotropic liquid crystalline phase formation of the compound is followed with Small-angle X-ray scattering (SAXS) analysis (Figure 5.5d). At room temperature, the SAXS pattern of PDMHP displays two peaks with d-spacing values of 39 Å and 19.6 Å owing to the crystalline order of the ionic liquid crystal. Increasing the temperature to 50 ℃, the liquid crystalline phase begins to emerge, and in addition to the peaks mentioned before, an additional shoulder initiates at a lower scattering vector. SAXS analysis of the compound at 140 ℃ clearly illustrates the formation of a liquid crystalline phase as the crystalline peaks completely disappear and a sharp self-assembly peak with a d-spacing of 43.9 Å persists. This sharp peak corresponds to the self- assembly of PDMHP by means of non-covalent interactions such as alkyl chain interdigitation, van der Waal's interactions and ion-lone pair interactions.

The expected layered 2D conduction pathways allow ion transportation in both parallel and perpendicular directions. This is confirmed by carrying out anisotropic ILC measurements in both directions for ILCs at varying temperature. The ionic conductivity value of each cell (gold electrode and Indium tin oxide (ITO) based electrode) is different at each temperature (SmA phase), explaining the anisotropic nature of these ILCs (Figure 5.6a and 5.6b). Both gold and ITO electrode cell configurations are shown in figure 5.6c. The ionic conductivity (IC) between the gold teeth (parallel to the smectic layer) is found to be one order of magnitude higher when compared to that between ITO plates perpendicular to the layer. The IC values at various temperatures in both directions are summarized in the figure 5.6d.

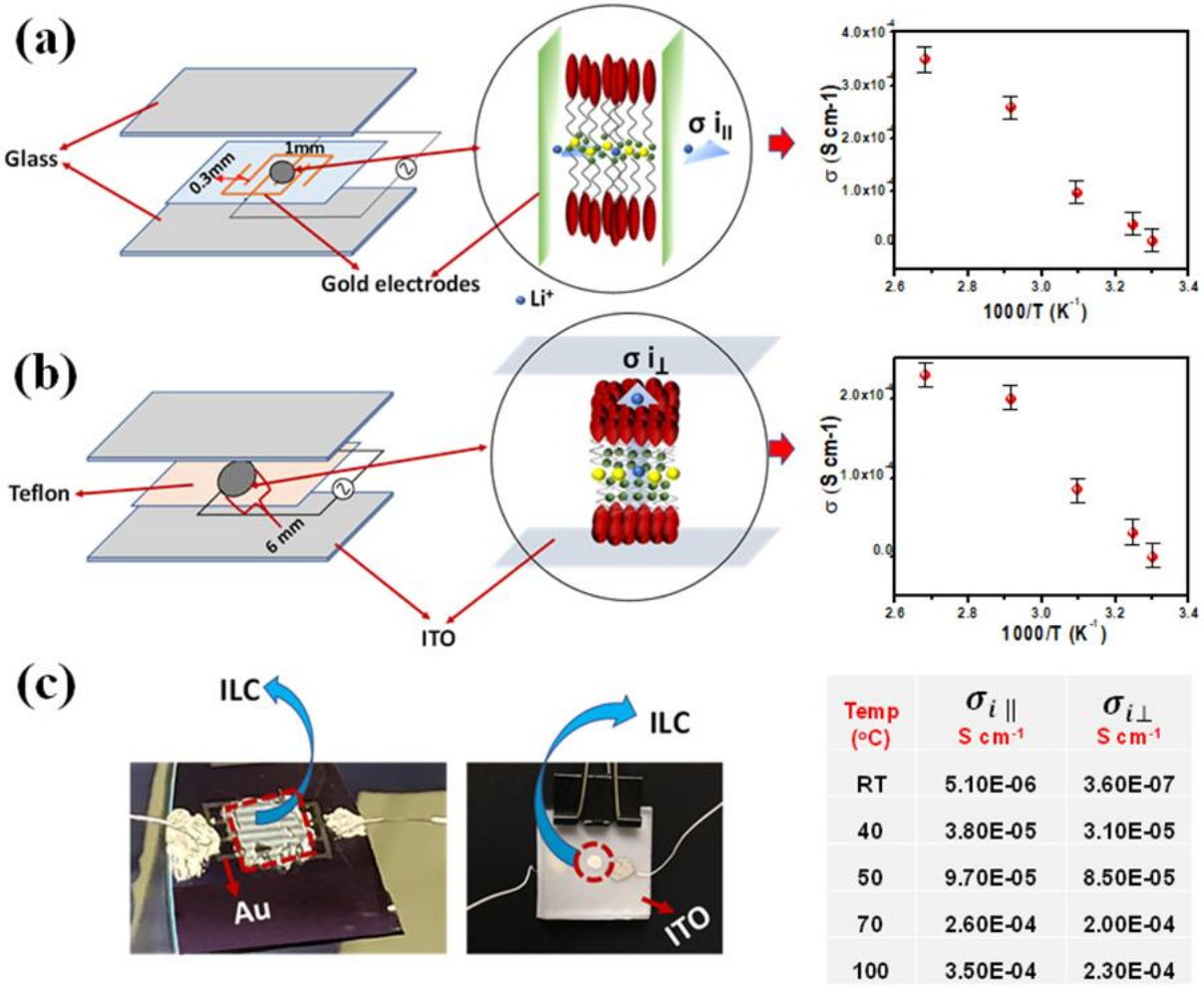

Temp (°C)	$\sigma_{i\parallel}$ S cm^{-1}	$\sigma_{i\perp}$ S cm^{-1}
RT	5.10E-06	3.60E-07
40	3.80E-05	3.10E-05
50	9.70E-05	8.50E-05
70	2.60E-04	2.00E-04
100	3.50E-04	2.30E-04

Figure 5.6. Anisotropic ionic conductivity measurements. (a). Structure of comb shaped gold electrode cell for horizontal ionic conductivity analysis of PDDMHP. (b) Structure of ITO electrode cell for perpendicular ion conductivity analysis. (c) gold electrode cell and ITO electrode cell. (d) Table with parallel and perpendicular ionic conductivity in PDDMHP at different temperatures varying from RT, 40, 50, 70 and 100 ^{o}C.

To further use LCs as an electrolyte for LiBs, the synthesized compounds are mixed with an optimized amount of lithium bis (trifluoromethyl sulfonyl) imide (LiTFSI) salt. This is to form 2D ion conducting pathways through ion – dipole interactions between the imidazole group and Li ions in the salt.[186, 218] It is expected that the concentration of salt has an impact on liquid-crystalline behavior, along with its viscosity and ionic conductivity. To verify, lithium composites of different ratios of 9:1, 3:1 and 1:1 respectively were prepared by solvent evaporation of a corresponding solution in tetrahydrofuran. Ionic conductivities of these electrolytes were measured repeatedly in ambient atmosphere by AC impedance spectroscopy over a frequency range of 1 Hz to 1 MHz at 60°C with amplitude 10 mV to ensure the reproducibility. Figure 5.7 shows the resultant electrochemical impedance Nyquist plot and corresponding equivalent circuit.

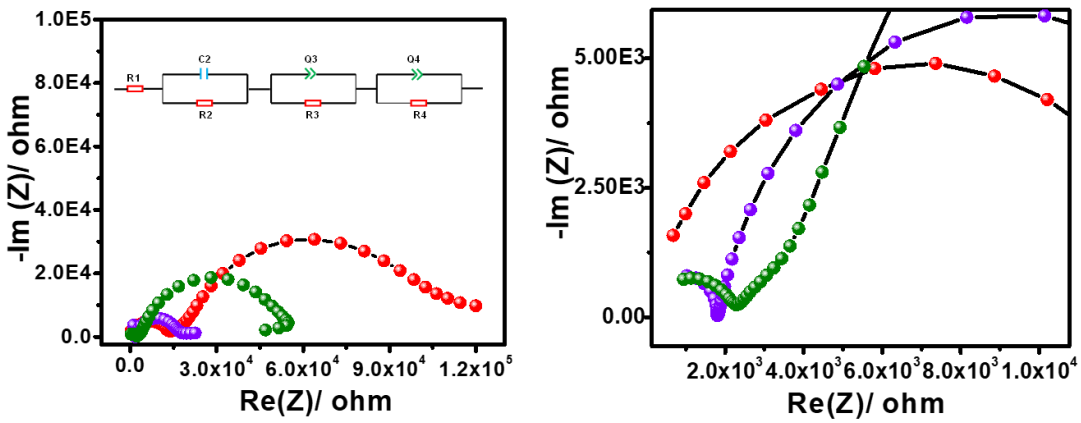

Figure 5.7. Electrochemical impedance Nyquist plot of different composition of PDDMHP with LiTFSI and corresponding equivalent circuit.

The solution resistance from the fitted impedance spectra is measured and ionic conductivity is mathematically calculated and plotted against temperature (1000/T) (Figure 5.8a) [219, 220].

The expression for ionic conductivity calculation is :

$\boldsymbol{\sigma} = (1/\boldsymbol{R}_s)(\boldsymbol{l}/\boldsymbol{a})$ where l is the thickness of the samples and a is the area of the electrode.

The measured Ionic conductivities in the order of 10^{-4} S cm^{-1} are obtained in the SmA phase and are shown in Table 5.2. There is an increase in ionic conductivity as the temperature is increased and when the material transforms to the liquid crystalline phase, SmA phase which can be due to the oriented conductive pathways creation. The higher conductivities at elevated temperatures, at SmA phases (<60°C) are due to the lower viscosity and broader 2D conducting pathways[221] (Figure 5.6b). This 2D arrangements of the ion conducting groups can provide opportunities for lithium ions to travel in both X and Y-directions, overcoming the defects confronted throughout the pathways while continuing directional movement. Among the different compositions of LC and Li salt, 9:1 ratio shows high ionic conductivity. The optimized amount of LiTFSI was found to be 9 equimolar (the molar ratio of PDMHP to LiTFSI was 9:1) and this mixture was selected as electrolyte for further electrochemical measurements.

Composition	σ (S/cm²)
LC/LiTFSI, 1:1	$1.37*10^{-4}$
LC/LiTFSI, 3:1	$1.72*10^{-4}$
LC/LiTFSI, 9:1	$1.85*10^{-4}$

Table 5.2. Ionic conductivities of different lithium composites containing PDDMPH and LiTFSI at different ratios of 9:1, 3:1 and 1:1 respectively.

Ion conductivity measurements are followed by lithium transference number (tLi^{+}) studies we carried out to find the suitability of these electrolytes for better Li-ion battery performance. The Li transference number (tLi^{+}) is calculated at RT and 60 ^{o}C via electrochemical impedance spectroscopy (EIS) before and after the chronoamperometric technique (CA) test. In Figure 5.8b, Chronoamperometry and EIS results of both the cells with and without LC are shown. At room temperature, tLi^{+} is found to be 0.062 whereas at elevated temperature (100 ^{o}C), it increases to

0.32. As per previous reports, it is expected that with a higher tLi^+ value, the concentration gradient will be reduced by removing the anion depletion induced electric fields near the electrode/ electrolyte interface, which limits the nucleation of Li dendrites[222]. According to Monroe and Newman's simulation studies, when tLi+ approaches unity, the ion concentration gradient near the Li anode is suppressed by extending the sands time i.e. stopping or delaying the dendrite growth[222, 223]. The synergistic effect of higher ionic conductivity and tLi+ values for parallel Li-ion conduction thus controls the concentration gradient near the electrode surface through effectively regulating Li ion mass transfer, which eventually inhibiting the dendrite formation and their growth. This is further evidenced by both the experimental and the interfacial computational simulations as given below.

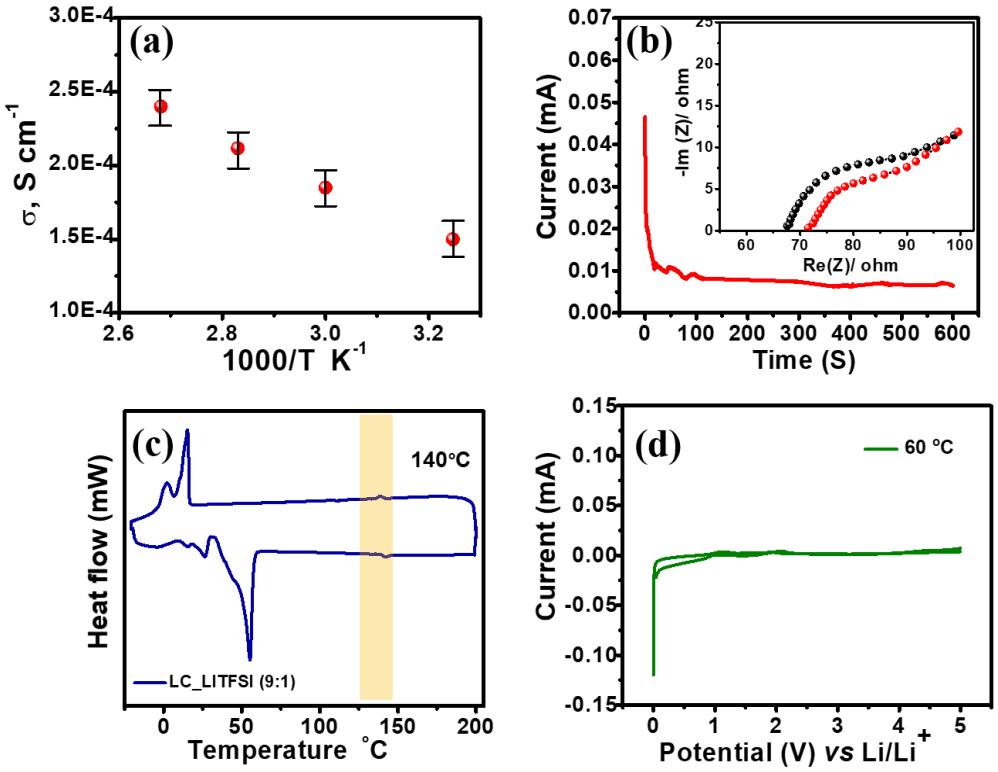

Figure 5.8. (a). DSC measurements of optimized LiTFSI/PDDMHP. (b) Electrochemical stability of formulated ILC based electrolyte. (c). Ionic conductivity of optimized LiTFSI/PDDMHP. (d). Li transference number measurement: Chronoamperometry profile for PDDMHP as electrolyte in symmetric Li/ (LiTFSI/PDDMHP) / Li cell with an applied voltage of 10mV, Nyquist plot for symmetric Li/ (LiTFSI/PDDMHP) / Li cell before and after polarization.

To corroborate the ILC property after adding LiTFSI salts, we have performed DSC measurement on the LC-LiTFSI (9:1) mixture, as shown in figure 5.8c. These thermotropic ILCs have a wide liquid crystalline window that provides the potential of utilizing their anisotropic nature over a wide range of temperatures. A DSC measurement confirmed that the mixture is still in the LC phase, with small changes in its anisotropy or mesophase window (Figure 5.8c). With the incorporation of Li salt (LiTFSI) to this ILC, there is a slight decrease in the anisotropic window, although it still extends up to 140 ^{o}C. The smectic A phase transitions have undergone small changes with the incorporation of LiTFSI. This is attributed to the fact that the in-plane packing of mesogens within the smectic layer is disturbed by the addition of bulky LiTFSI salts. Also, the LC electrolyte is expected to show higher ionic conductivity and is chosen as an electrolyte for electrochemical measurements. The isotropization temperature decreases for the mixture containing ILC and LiTFSI in a 9:1 molar ratio, although the SmA phase is still present over a wide temperature range. The SmA phase with higher molecular motion exhibited higher molecular conductivity as expected at an elevated liquid crystalline temperature, making them preferable for use as electrolytes in LiBs. As previously mentioned, the ionic conductivity is satisfactorily enhanced to 10E-4 at a temperature of 60 ^{O}C due to the lower viscosity and highly efficient oriented ion conducting pathways of the SmA phase. Thus, while using this ILC: LITFSI mixture in a 9:1 molar ratio, can act as an electrolyte with its persisting anisotropic nature enabling controlled Li ion mass transport.

Electrochemical stability of the ILC- LiTFSI composite based electrolyte is evaluated using cyclic voltammetry using Li/Li^{+} symmetric cells at an elevated temperature of 100°C where the SmA – anisotropic phase is observed (Figure 5.8d). The measurement was conducted in a potential range from 0 to 5 V versus Li/Li^{+} at a scan rate of 0.025 mVs^{-1} and the voltammogram is shown

in Figure (5.8d). There is a small current near the 0 V versus Li/Li^+ during the anodic and cathodic sweep, which is due to the Li deposition and dissolution. There is no significant electrolyte decomposition at higher voltage, which suggests stable Li transportation, and electrochemical reactions at the electrodes in the presence of an ILC electrolyte in a wide potential window. Thus, the electrolyte mixture with an optimized molar ratio of ILC and LiTFSI shows a higher electrochemical stability without any decomposition at a higher voltage range, indicating the efficient transport of Li ions between the electrodes without undergoing any electrochemical reactions. This can be attributed to the presence of mesogens acting as an ion conducting moiety.

Electrochemical cycling performance

After formulating the electrolyte, dendrite suppression studies have been carried out where the anisotropic nature of the ILC believed to be regulate the ion concentration gradient at the interface. The electrodeposition of Li in the ILC based electrolytes was investigated using galvanostatic cycling of Li| LC-LiTFSI| Li symmetric lithium cells in which the lithium striping process is carried out under constant current 0.032 mA. The symmetric cells contain Li counter/ reference and working electrode on both sides of a hollow teflon spacer filled with ILC electrolyte. Symmetrical Li/Li cells with and without ILC as an electrolyte are tested at a current density of 0.1 mA cm^{-2} and a temperature of 60 ^{o}C to evaluate the long-term electrochemical cycling stability of the Li electrodes. Li/ ILC-LiTFSI /Li showed a stable Li plating / stripping behavior in the presence of an anisotropic electrolyte with a gradual increase in polarization, which can be clearly seen in the voltage hysteresis. The difference between Li stripping and plating voltages represents the voltage hysteresis and is principally determined from the applied current density, electrode/ electrolyte interfacial properties and charge transfer resistance. A symmetrical Li/Li cell containing LiTFSI/Propylene Carbonate (PC) as an electrolyte show a stable voltage hysteresis

without any irregular oscillations when compared with the cell having ILC; however, a dendrite induced internal short circuit is seen after 400 h (Figure 5.9). In contrast, the cell with the ILC electrolyte is able to cycle stably for more than 800 hours as the anisotropic electrolyte medium can improve the Li^+ mass transport between the major dendrite growth sites, and thereby form dendrites in a uniform and compact way.

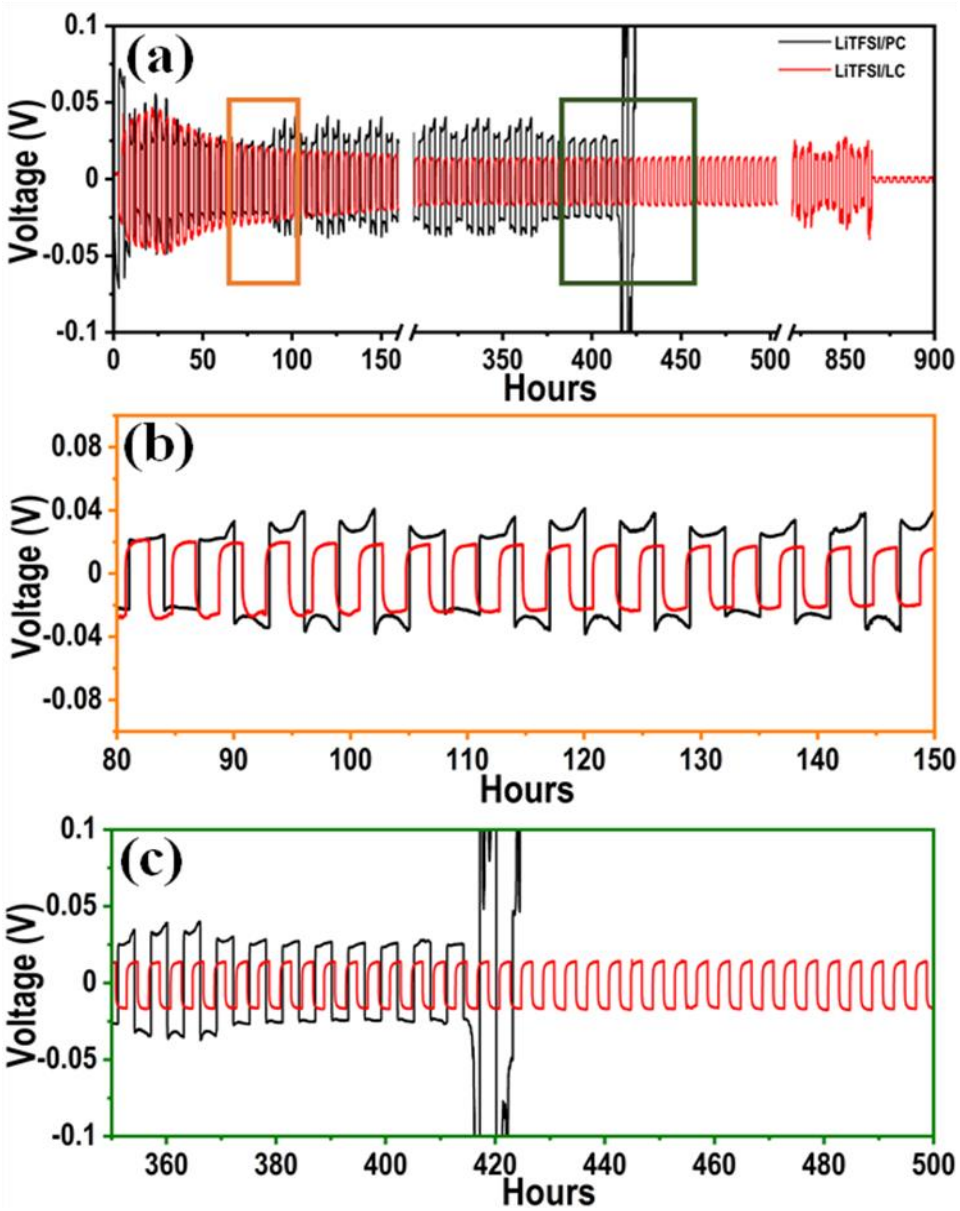

Figure 5.9. Electrochemical characterization of symmetric Li/ (LiTFSI/PDDMHP) / Li and Li/ LiTFSI/ Li cells. (a) potential profiles during galvanostatic cycles with a current density of 0.1 mA cm^{-2}. Zoomed in view of selected cycles are shown below.

Simulation of the Interfacial Reactive Transport

To understand the local transport mechanisms that lead to dendrite suppression in the ILC electrolyte, a numerical model is developed to study the reactive transport near the electrode-electrolyte interface. A Lagrangian particle-based modeling method known as smoothed particle hydrodynamics (SPH) is used to investigate how changes in local ion transport properties affect the growth of dendrites. To approximate the ILC electrolyte, a pseudo-separator like structure is simulated. Based on the experimental characterization of the ILC electrolyte, it is assumed ILC supra molecules in the electrolyte have a semi-ordered structure that can be approximated as a separator of rod-like particles. Rod-like particles on the order of a few microns in length are dispersed throughout the electrolyte in different orientations. The effects of particle orientation are varied from completely parallel to the anode surface, to randomly oriented (Figure 5.10a). Simulations are used to elucidate how the ILCs effect local transport and dendrite growth. Dendrite growth increases as the supramolecules align perpendicular to the anode surface. While a random orientation or alignment favoring the direction parallel to the anode reduces the dendrite growth, as seen in Figure 5.10a. This can also be seen in the contour plots of local mass flux in Figure 5.10b and the growth rate of Figure 5.10c. The anisotropic mass transport effect is proposed as a novel concept towards dendrite growth suppression in Li batteries and the corresponding schematic is shown in Figure 5.10d. The concentration gradient near the anode-electrolyte interface can be controlled by inducing these directional properties in Li ion batteries with the help of anisotropic ILCs[193]. From the numerical models of Figure 5.10b, it can be seen that the ILC supramolecules restrict local mass transport near the electrode interface. This leads to slower dendrite growth. The parallelly aligned liquid crystalline molecules with their layered structure control the Li ion mass transfer, which in turn affects the Li ion concentration in the vicinity of the

electrode. The Li ion concentration gradient near the electrode/ electrode interface is the major reason for dendrite growth after nucleation. This lesser ion concentration gradient is reflected in the uniform SEI formation, which controls the dendrite growth rate.

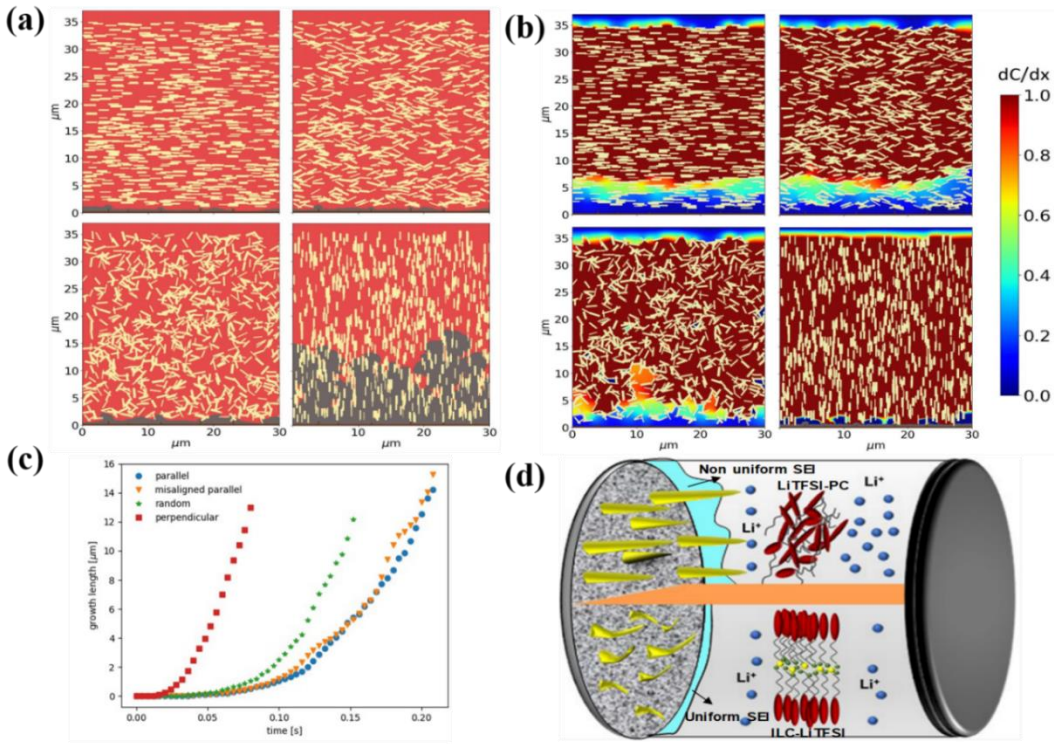

Figure 5.10. (a) Simulations domains for structures parallel, misaligned parallel, random, and perpendicular to the anode. (b) Local mass flux through the separators as dendrite grow into the separator from the anode (at y=0). (c) Growth rate of dendrites over time for each separator structure. (d) Graphical representation of the proposed mechanism.

The effects of local transport mechanisms on dendrite growth are also seen in the numerical models of the interface as seen in Figures 5.10b. The concentration gradients drive the transport of Li near the interface. Along the surface of the anode (bottom of fig.5.10 a-b), the gradient goes toward zero in the cases of parallel, random, and misaligned parallel structures. This is due to the high tortuosity through these structures. In the case of the perpendicular structure the tortuosity is roughly one and the separator has little effect on the local mass flux. The lower mass flux along

the anode leads to suppression of dendrite growth and longer battery lifetime. The low mass flux indicates an even distribution of Li concentration across the anode surface, which leads to a more even Li deposition. This allows for slower and more uniform growth, resulting in less harmful dendrites. In the presence of an anisotropic electrolyte medium, major dendrites form at the interspace between the initial dendritic nucleation sites, while the already formed dendrites are suppressed. This is supported by the numerical models as seen in the parallel and random cases of Figure 5.10b. In the anisotropic case, the Li ion diffusion to the major dendrite growth region decreases and hinders the replenishment of Li+ ions in that region, prompting Li+ ions to deposit in the adjacent dendrite free regions and thus leads to the formation of more compact and flat dendrites. Thus, this thermotropic ILC electrolytes with their ability to orient themselves in different directions to control Li mass transport and thereby dendrite growth can act as pseudo separator.

5.4 Conclusions

In summary, we have shown that the synthesis of anisotropic liquid crystalline electrolytes and its efficacy in mitigation of dendrite growth characteristics through reduce the Li ion concentration near the dendrite tip. The numerical models have demonstrated the mechanism of ILC electrolytes in dendrite suppression and for better Li diffusion control. This anisotropic mass transport effect can suppress the dendrite growth without sacrificing battery performance. New thermotropic ILC with SmA phase for a wide temperature window containing 2D ion conducting pathways have been prepared and well characterized using various microscopic and spectroscopic techniques. The anisotropic ion conductivity was probed by conducting EIS measurements using both gold electrodes and ITO electrodes in both parallel and perpendicular directions consecutively. The PDDMHP: LiTFSI in the 9:1 molar ratio has been tested for dendrite studies

and showed a highly ionic conducting pathways and near unity tLi^+ can greatly reduce the Li ion concentration at the anode surface and retard the dendrite formation and growth. This is further exemplified through continuous lithium plating/stripping around 850 hrs. with negligible changes polarization at extended cycling, suggesting the compact and robustness of an anisotropic ILC electrolyte mitigating dendrites formation. The demonstrated results reveal that the anisotropic ILCs are promising LIB electrolytes for long cell cycle life while ensure safety by controlling dendritic parasitic reactions in the cells.

CHAPTER 6 SUMMARY AND FUTURE OUTLOOK

Lithium–sulfur batteries with their high theoretical energy density and environmental friendliness received much attention in the past decade. However, the uncontrollable growth of lithium dendrites in the Li metal anode during repeated Li plating/ stripping processes commonly causes rapid capacity decay and serious safety issue of Li–S batteries. Also, on the sulfur cathode, a series of highly soluble lithium polysulfides (Li_2S_x, $4 \leq \times \leq 8$) intermediates are unavoidably produced and shuttled between the electrodes, which would react with lithium anode, following the fast self-discharge and rapid capacity fading of Li–S batteries. Thus, in order to address these problems from both anode and cathode side, there is a high need of effective strategies. Towards this, we proposed electrocatalysis principles into Li-S battery configuration to stabilize polysulfide shuttle process and to improve the rate capabilities. As a proof of concept, we have studied LiPS conversion reactions with different electrocatalysts such as Pt, WS_2, NbS_2 etc. where we demonstrated the significance of electrocatalytic surfaces on lithium-sulfur redox kinetics by using electrochemical potentiodynamic and potentiostatic methods. Thus, we concluded that the catalytic interface reduces the redox overpotential and enhances the surface diffusion properties of LiPS anions. Thorough and systematic analysis validates the enhanced adsorption capability of soluble LiPS on the catalytic interface and the successive electrochemical reactions rather than polysulfide dissolution. More relevantly, we summarize that the catalyst exhibits a substantial activity towards LiPS liquid-to-solid conversion and directs the Li_2S nucleation process *via* instantaneous growth, which had a direct impact on high capacity gaining. In-depth analysis confirmed that the electrocatalyst plays a major role in accelerating the Li_2S process kinetics among multistep LiPS redox reactions. The improvement in conductivity through the integration of carbon cloth along with the catalytic behavior of NbS_2 aided to give a stable capacity of 810

mA h g^{-1} for NbS_2/CC electrodes. Additionally, our study gave evidence to the potential ability of catalytic active sites for improving the cell reversibility. Regarding the Li metal anode issue, our research explored the use of a special class of ionic liquids (ILs) with liquid crystal properties for the electrolyte of Li metal batteries towards the dendrite suppression. we showed the synthesis of anisotropic liquid crystalline electrolytes and its efficacy in mitigation of dendrite growth characteristics through reduce the Li ion concentration near the dendrite tip. We also carried out numerical models demonstrating the mechanism of ILC electrolytes in dendrite suppression and better Li diffusion control. Thus, we concluded that the anisotropic mass transport effect can suppress the dendrite growth without sacrificing battery performance. Towards this, a novel thermotropic ILC with SmA phase for a wide temperature window containing 2D ion conducting pathways have been prepared and well characterized using various microscopic and spectroscopic techniques. The anisotropic ion conductivity was investigated by conducting EIS measurements using both gold electrodes and ITO electrodes in both parallel and perpendicular directions consecutively. The ILC: LiTFSI in the 9:1 molar ratio has been tested for dendrite studies and showed a highly ionic conducting pathways and near unity tLi^+ which reduced the Li ion concentration at the anode surface and slowed down the dendrite formation and growth. This potential ability of ILC is further exemplified through continuous lithium plating/stripping around 850 hrs. with negligible changes polarization at extended cycling, suggesting the mitigation of dendrites formation. Thus, our study confirms that the anisotropic ILCs are promising LIB electrolytes for long cell cycle life while ensuring safety by controlling dendritic parasitic reactions in the cells.

Kinetic issue of the sulfur cathode is addressed by heterogeneous polysulfide electrocatalysis, which aims to accelerate the cathode redox kinetics by reducing the activation

energy barriers. This polysulfide electrocatalysis improved the overall battery performance by reducing the polarization, improving the rate response, and extending the cycle life. All these efforts greatly enhanced the Li-S battery performance, and thus, the same approach could be implemented to other metal polysulfide batteries such as Na-S, Mg-S etc. to achieve high energy density and power density battery systems. The performance promotion is realized in the laboratory scale under ideal conditions, can be used to provide guidance towards the practical pouch cell level. Additionally, in-depth studies on the novel Li−S chemistry will provide fresh insights and enlighten other key energy-related processes based on multielectron and multiphase electrochemical reactions. Towards the dendrite suppression in Li-S batteries, ILCs act as promising electrolytes. However, details on their ionic conductivity over the range of temperature, electrochemical stability and feasibility are yet to be reported in-detail. Thus, ILCs are highly desirable to explore, design, and/or optimize electrolytes for general Li metal batteries to address the issues of Li dendrite growth and stabilize their electrochemical performance, such as specific capacities, cycle life and rate capabilities. In addition to Li-S batteries, dendrite growth is also a problem for other battery chemistries, such as Li-ion, Li-O_2, NaS and NiCd, and for many metal and electronic fabrication processes, such as solidification and electroplating. If anisotropic transport properties are shown to improve the performance of batteries, then similar principles can be used to increase the performance of other batteries. Also, the effect of different cations, alkyl chain length on the extent of anisotropy and their effect on dendrite growth should be studied which will finally help in the development of RT ILC based electrolyte. Though we were able to individually address the major issues with the Li-S battery chemistry, it is still a big challenge to explore a bifunctional material for simultaneously inhibiting lithium dendrites and polysulfide shuttle in Li–S batteries.

REFERENCES

[1] P. G. Bruce, S. A. Freunberger, L. J. Hardwick, and J.-M. Tarascon, "Li-O2 and Li-S batteries with high energy storage," *Nat Mater,* 10.1038/nmat3191 vol. 11, no. 1, pp. 19-29, 01//print 2012. [Online]. Available: http://dx.doi.org/10.1038/nmat3191.

[2] G. Girishkumar, B. McCloskey, A. C. Luntz, S. Swanson, and W. Wilcke, "Lithium−Air Battery: Promise and Challenges," *The Journal of Physical Chemistry Letters,* vol. 1, no. 14, pp. 2193-2203, 2010, doi: 10.1021/jz1005384.

[3] B. Dunn, H. Kamath, and J.-M. Tarascon, "Electrical Energy Storage for the Grid: A Battery of Choices," *Science,* vol. 334, no. 6058, p. 928, 2011, doi: 10.1126/science.1212741.

[4] M. Winter and R. J. Brodd, "What Are Batteries, Fuel Cells, and Supercapacitors?," *Chemical Reviews,* vol. 104, no. 10, pp. 4245-4270, 2004/10/01 2004, doi: 10.1021/cr020730k.

[5] S. Andrews, "Preface to the second edition," in *Modern Batteries (Second Edition)*, C. A. Vincent and B. Scrosati Eds. Oxford: Butterworth-Heinemann, 1997, pp. ix-x.

[6] B. R. Thomas, *Linden's Handbook of Batteries, Fourth Edition*, 4th ed. ed. New York: McGraw-Hill Education (in eng), 2011.

[7] J. M. Tarascon and M. Armand, "Issues and challenges facing rechargeable lithium batteries," *Nature,* vol. 414, no. 6861, pp. 359-367, 2001/11/01 2001, doi: 10.1038/35104644.

[8] D. Lin, Y. Liu, and Y. Cui, "Reviving the lithium metal anode for high-energy batteries," *Nature Nanotechnology,* Review Article vol. 12, p. 194, 03/07/online 2017, doi: 10.1038/nnano.2017.16.

[9] M. S. Whittingham, "Electrical Energy Storage and Intercalation Chemistry," *Science,* vol. 192, no. 4244, p. 1126, 1976, doi: 10.1126/science.192.4244.1126.

[10] M. M. Thackeray, W. I. F. David, P. G. Bruce, and J. B. Goodenough, "Lithium insertion into manganese spinels," *Materials Research Bulletin,* vol. 18, no. 4, pp. 461-472, 1983/04/01/ 1983, doi: https://doi.org/10.1016/0025-5408(83)90138-1.

[11] B. Dunn, H. Kamath, and J.-M. Tarascon, "Electrical Energy Storage for the Grid: A Battery of Choices," *Science,* vol. 334, no. 6058, pp. 928-935, 2011, doi: 10.1126/science.1212741.

[12] J. M. Tarascon and M. Armand, "Issues and challenges facing rechargeable lithium batteries," *Nature,* vol. 414, p. 359, 11/15/online 2001, doi: 10.1038/35104644.

[13] W. Xu *et al.*, "Lithium metal anodes for rechargeable batteries," *Energy & Environmental Science,* 10.1039/C3EE40795K vol. 7, no. 2, pp. 513-537, 2014, doi: 10.1039/C3EE40795K.

[14] J. B. Goodenough and K.-S. Park, "The Li-Ion Rechargeable Battery: A Perspective," *Journal of the American Chemical Society,* vol. 135, no. 4, pp. 1167-1176, 2013/01/30 2013, doi: 10.1021/ja3091438.

[15] B. Scrosati and J. Garche, "Lithium batteries: Status, prospects and future," *Journal of Power Sources,* vol. 195, no. 9, pp. 2419-2430, 2010/05/01/ 2010, doi: https://doi.org/10.1016/j.jpowsour.2009.11.048.

[16] T. Ohzuku and R. J. Brodd, "An overview of positive-electrode materials for advanced lithium-ion batteries," *Journal of Power Sources,* vol. 174, no. 2, pp. 449-456, 2007/12/06/ 2007, doi: https://doi.org/10.1016/j.jpowsour.2007.06.154.

[17] R. Roque-Malherbe, *The physical chemistry of materials: Energy and environmental applications*. 2016, pp. 1-500.

[18] K. Nishikawa, T. Mori, T. Nishida, Y. Fukunaka, and M. Rosso, "Li dendrite growth and Li+ ionic mass transfer phenomenon," *Journal of Electroanalytical Chemistry,* vol. 661, no. 84, 2011.

[19] D. Aurbach, E. Zinigrad, Y. Cohen, and H. Teller, "A short review of failure mechanisms of lithium metal and lithiated graphite anodes in liquid electrolyte solutions," *Solid State Ionics,* vol. 148, no. 3, pp. 405-416, 2002/06/02/ 2002, doi: https://doi.org/10.1016/S0167-2738(02)00080-2.

[20] X. Wang, Z. Wen, Y. Liu, and X. Wu, "A novel composite containing nanosized silicon and tin as anode material for lithium ion batteries," *Electrochimica Acta,* vol. 54, no. 20, pp. 4662-4667, 2009/08/01/ 2009, doi: https://doi.org/10.1016/j.electacta.2009.03.055.

[21] D. Deng, "Li-ion batteries: basics, progress, and challenges," *Energy Science & Engineering,* vol. 3, no. 5, pp. 385-418, 2015, doi: 10.1002/ese3.95.

[22] D. Wang, W. Zhang, W. Zheng, X. Cui, T. Rojo, and Q. Zhang, "Towards High-Safe Lithium Metal Anodes: Suppressing Lithium Dendrites via Tuning Surface Energy," *Advanced Science,* vol. 4, no. 1, p. 1600168, 2017, doi: 10.1002/advs.201600168.

[23] J. B. Goodenough and Y. Kim, "Challenges for Rechargeable Li Batteries," *Chemistry of Materials,* vol. 22, no. 3, pp. 587-603, 2010/02/09 2010, doi: 10.1021/cm901452z.

[24] L. Carbone, S. G. Greenbaum, and J. Hassoun, "Lithium sulfur and lithium oxygen batteries: new frontiers of sustainable energy storage," *Sustainable Energy & Fuels,* 10.1039/C6SE00124F vol. 1, no. 2, pp. 228-247, 2017, doi: 10.1039/C6SE00124F.

[25] P. G. Bruce, "Energy storage beyond the horizon: Rechargeable lithium batteries," *Solid State Ionics,* vol. 179, no. 21, pp. 752-760, 2008/09/15/ 2008, doi: https://doi.org/10.1016/j.ssi.2008.01.095.

[26] E. M. Erickson, C. Ghanty, and D. Aurbach, "New Horizons for Conventional Lithium Ion Battery Technology," *The Journal of Physical Chemistry Letters,* vol. 5, no. 19, pp. 3313-3324, 2014/10/02 2014, doi: 10.1021/jz501387m.

[27] B. Scrosati, J. Hassoun, and Y.-K. Sun, "Lithium-ion batteries. A look into the future," *Energy & Environmental Science,* 10.1039/C1EE01388B vol. 4, no. 9, pp. 3287-3295, 2011, doi: 10.1039/C1EE01388B.

[28] G. Babu, K. Ababtain, K. Y. S. Ng, and L. M. R. Arava, "Electrocatalysis of Lithium Polysulfides: Current Collectors as Electrodes in Li/S Battery Configuration," Article vol. 5, p. 8763, 03/05/online 2015, doi: 10.1038/srep08763

[29] G. Babu, N. Masurkar, H. Al Salem, and L. M. R. Arava, "Transition Metal Dichalcogenide Atomic Layers for Lithium Polysulfides Electrocatalysis," *Journal of the American Chemical Society,* vol. 139, no. 1, pp. 171-178, 2017/01/11 2017, doi: 10.1021/jacs.6b08681.

[30] S. A. Freunberger *et al.*, "Reactions in the Rechargeable Lithium–O2 Battery with Alkyl Carbonate Electrolytes," *Journal of the American Chemical Society,* vol. 133, no. 20, pp. 8040-8047, 2011/05/25 2011, doi: 10.1021/ja2021747.

[31] A. Débart, J. Bao, G. Armstrong, and P. G. Bruce, "An O2 cathode for rechargeable lithium batteries: The effect of a catalyst," *Journal of Power Sources,* vol. 174, no. 2, pp. 1177-1182, 2007/12/06/ 2007, doi: https://doi.org/10.1016/j.jpowsour.2007.06.180.

[32] X. B. Zhu, T. S. Zhao, Z. H. Wei, P. Tan, and L. An, "A high-rate and long cycle life solid-state lithium–air battery," *Energy & Environmental Science,* 10.1039/C5EE02867A vol. 8, no. 12, pp. 3745-3754, 2015, doi: 10.1039/C5EE02867A.

[33] B. M. Gallant, D. G. Kwabi, R. R. Mitchell, J. Zhou, C. V. Thompson, and Y. Shao-Horn, "Influence of Li2O2 morphology on oxygen reduction and evolution kinetics in Li–O2 batteries," *Energy & Environmental Science,* 10.1039/C3EE40998H vol. 6, no. 8, pp. 2518-2528, 2013, doi: 10.1039/C3EE40998H.

[34] Y.-C. Lu, H. A. Gasteiger, and Y. Shao-Horn, "Catalytic Activity Trends of Oxygen Reduction Reaction for Nonaqueous Li-Air Batteries," *Journal of the American Chemical Society,* vol. 133, no. 47, pp. 19048-19051, 2011/11/30 2011, doi: 10.1021/ja208608s.

[35] A. Manthiram, Y. Fu, S.-H. Chung, C. Zu, and Y.-S. Su, "Rechargeable Lithium–Sulfur Batteries," *Chemical Reviews,* vol. 114, no. 23, pp. 11751-11787, 2014/12/10 2014, doi: 10.1021/cr500062v.

[36] X. Ji and L. F. Nazar, "Advances in Li-S batteries," *Journal of Materials Chemistry,* 10.1039/B925751A vol. 20, no. 44, pp. 9821-9826, 2010, doi: 10.1039/B925751A.

[37] S. S. Zhang, "Liquid electrolyte lithium/sulfur battery: Fundamental chemistry, problems, and solutions," *Journal of Power Sources,* vol. 231, pp. 153-162, 2013/06/01/ 2013, doi: http://dx.doi.org/10.1016/j.jpowsour.2012.12.102.

[38] Y. Luo *et al.*, "Strategies for inhibiting anode dendrite growth in lithium–sulfur batteries," *Journal of Materials Chemistry A,* 10.1039/C9TA12910C vol. 8, no. 9, pp. 4629-4646, 2020, doi: 10.1039/C9TA12910C.

[39] J. Liang, Z.-H. Sun, F. Li, and H.-M. Cheng, "Carbon materials for Li–S batteries: Functional evolution and performance improvement," *Energy Storage Materials,* vol. 2, pp. 76-106, 2016/01/01/ 2016, doi: https://doi.org/10.1016/j.ensm.2015.09.007.

[40] A. Rosenman, E. Markevich, G. Salitra, D. Aurbach, A. Garsuch, and F. F. Chesneau, "Review on Li-Sulfur Battery Systems: an Integral Perspective," *Advanced Energy Materials,* vol. 5, no. 16, p. 1500212, 2015/08/01 2015, doi: 10.1002/aenm.201500212.

[41] J. Lochala, D. Liu, B. Wu, C. Robinson, and J. Xiao, "Research Progress toward the Practical Applications of Lithium–Sulfur Batteries," *ACS Applied Materials & Interfaces,* vol. 9, no. 29, pp. 24407-24421, 2017/07/26 2017, doi: 10.1021/acsami.7b06208.

[42] M. Wild *et al.*, "Lithium sulfur batteries, a mechanistic review," *Energy & Environmental Science,* 10.1039/C5EE01388G vol. 8, no. 12, pp. 3477-3494, 2015, doi: 10.1039/C5EE01388G.

[43] L. Carbone *et al.*, "Comparative Study of Ether-Based Electrolytes for Application in Lithium–Sulfur Battery," *ACS Applied Materials & Interfaces,* vol. 7, no. 25, pp. 13859-13865, 2015/07/01 2015, doi: 10.1021/acsami.5b02160.

[44] D. Devaux, R. Bouchet, D. Glé, and R. Denoyel, "Mechanism of ion transport in PEO/LiTFSI complexes: Effect of temperature, molecular weight and end groups," *Solid State Ionics,* vol. 227, pp. 119-127, 2012/10/29/ 2012, doi: https://doi.org/10.1016/j.ssi.2012.09.020.

[45] O. Borodin, G. D. Smith, and W. Henderson, "Li+ Cation Environment, Transport, and Mechanical Properties of the LiTFSI Doped N-Methyl-N-alkylpyrrolidinium+TFSI- Ionic Liquids," *The Journal of Physical Chemistry B,* vol. 110, no. 34, pp. 16879-16886, 2006/08/01 2006, doi: 10.1021/jp061930t.

[46] C. Zu, Y.-S. Su, Y. Fu, and A. Manthiram, "Improved lithium–sulfur cells with a treated carbon paper interlayer," *Physical Chemistry Chemical Physics,* 10.1039/C2CP43394J vol. 15, no. 7, pp. 2291-2297, 2013, doi: 10.1039/C2CP43394J.

[47] S. Jeong, D. Bresser, D. Buchholz, M. Winter, and S. Passerini, "Carbon coated lithium sulfide particles for lithium battery cathodes," *Journal of Power Sources,* vol. 235, pp. 220-225, 2013/08/01/ 2013, doi: https://doi.org/10.1016/j.jpowsour.2013.01.084.

[48] X. Ji and L. F. Nazar, "Advances in Li–S batteries," *Journal of Materials Chemistry,* 10.1039/B925751A vol. 20, no. 44, pp. 9821-9826, 2010, doi: 10.1039/B925751A.

[49] Y. M. Lee, N.-S. Choi, J. H. Park, and J.-K. Park, "Electrochemical performance of lithium/sulfur batteries with protected Li anodes," *Journal of Power Sources,* vol. 119-121, pp. 964-972, 2003/06/01/ 2003, doi: https://doi.org/10.1016/S0378-7753(03)00300-8.

[50] D. Wang, W. Zhang, W. Zheng, X. Cui, T. Rojo, and Q. Zhang, "Towards High-Safe Lithium Metal Anodes: Suppressing Lithium Dendrites via Tuning Surface Energy," *Advanced Science,* vol. 4, no. 1, pp. 1600168-n/a, 2017, Art no. 1600168, doi: 10.1002/advs.201600168.

[51] X. Liang, C. Hart, Q. Pang, A. Garsuch, T. Weiss, and L. F. Nazar, "A highly efficient polysulfide mediator for lithium–sulfur batteries," Article vol. 6, p. 5682, 01/06/online 2015, doi: 10.1038/ncomms6682

[52] Z. Yuan *et al.*, "Powering lithium–sulfur battery performance by propelling polysulfide redox at sulfiphilic hosts," *Nano letters,* vol. 16, no. 1, pp. 519-527, 2016. [Online]. Available:

[53] R. Kumar, J. Liu, J.-Y. Hwang, and Y.-K. Sun, "Recent research trends in Li–S batteries," *Journal of Materials Chemistry A,* 10.1039/C8TA01483C vol. 6, no. 25, pp. 11582-11605, 2018, doi: 10.1039/C8TA01483C.

[54] J. Zhang *et al.*, "Nanostructured Host Materials for Trapping Sulfur in Rechargeable Li–S Batteries: Structure Design and Interfacial Chemistry," *Small Methods,* vol. 2, no. 1, p. 1700279, 2018/01/01 2018, doi: 10.1002/smtd.201700279.

[55] W. Chen *et al.*, "A New Hydrophilic Binder Enabling Strongly Anchoring Polysulfides for High-Performance Sulfur Electrodes in Lithium-Sulfur Battery," *Advanced Energy Materials,* vol. 8, no. 12, p. 1702889, 2018/04/01 2018, doi: 10.1002/aenm.201702889.

[56] X. Li and X. Sun, "Interface Design and Development of Coating Materials in Lithium–Sulfur Batteries," *Advanced Functional Materials,* vol. 28, no. 30, p. 1801323, 2018/07/01 2018, doi: 10.1002/adfm.201801323.

[57] H. Zhang, C. Lin, X. Hu, B. Zhu, and D. Yu, "Effective Dual Polysulfide Rejection by a Tannic Acid/FeIII Complex-Coated Separator in Lithium–Sulfur Batteries," *ACS Applied Materials & Interfaces,* vol. 10, no. 15, pp. 12708-12715, 2018/04/18 2018, doi: 10.1021/acsami.8b01189.

[58] C. Dai *et al.*, "Honeycomb-Like Spherical Cathode Host Constructed from Hollow Metallic and Polar Co9S8 Tubules for Advanced Lithium–Sulfur Batteries," *Advanced Functional Materials,* vol. 28, no. 14, p. 1704443, 2018/04/01 2018, doi: 10.1002/adfm.201704443.

[59] R. Fang, K. Chen, L. Yin, Z. Sun, F. Li, and H.-M. Cheng, "The Regulating Role of Carbon Nanotubes and Graphene in Lithium-Ion and Lithium–Sulfur Batteries," *Advanced Materials,* vol. 31, no. 9, p. 1800863, 2019/03/01 2019, doi: 10.1002/adma.201800863.

[60] X. Ni, T. Qian, X. Liu, N. Xu, J. Liu, and C. Yan, "High Lithium Ion Conductivity LiF/GO Solid Electrolyte Interphase Inhibiting the Shuttle of Lithium Polysulfides in Long-Life Li–S Batteries," *Advanced Functional Materials,* vol. 28, no. 13, p. 1706513, 2018/03/01 2018, doi: 10.1002/adfm.201706513.

[61] D.-W. Wang *et al.*, "Carbon–sulfur composites for Li–S batteries: status and prospects," *Journal of Materials Chemistry A,* 10.1039/C3TA11045A vol. 1, no. 33, pp. 9382-9394, 2013, doi: 10.1039/C3TA11045A.

[62] Y. Yang, G. Zheng, and Y. Cui, "Nanostructured sulfur cathodes," *Chemical Society Reviews,* 10.1039/C2CS35256G vol. 42, no. 7, pp. 3018-3032, 2013, doi: 10.1039/C2CS35256G.

[63] M.-K. Song, Y. Zhang, and E. J. Cairns, "A Long-Life, High-Rate Lithium/Sulfur Cell: A Multifaceted Approach to Enhancing Cell Performance," *Nano Letters,* vol. 13, no. 12, pp. 5891-5899, 2013/12/11 2013, doi: 10.1021/nl402793z.

[64] M.-S. Song *et al.*, "Effects of Nanosized Adsorbing Material on Electrochemical Properties of Sulfur Cathodes for Li/S Secondary Batteries," *Journal of The Electrochemical Society,* vol. 151, no. 6, p. A791, 2004, doi: 10.1149/1.1710895.

[65] Z. Xiao *et al.*, "A Lightweight TiO_2/Graphene Interlayer, Applied as a Highly Effective Polysulfide Absorbent for Fast, Long-Life Lithium-Sulfur Batteries," (in eng), *Adv Mater,* vol. 27, no. 18, pp. 2891-8, May 13 2015, doi: 10.1002/adma.201405637.

[66] X. Ji, S. Evers, R. Black, and L. F. Nazar, "Stabilizing lithium–sulphur cathodes using polysulphide reservoirs," *Nature Communications,* vol. 2, no. 1, p. 325, 2011/05/24 2011, doi: 10.1038/ncomms1293.

[67] Q. Pang, X. Liang, C. Y. Kwok, and L. F. Nazar, "Advances in lithium–sulfur batteries based on multifunctional cathodes and electrolytes," *Nature Energy,* vol. 1, no. 9, p. 16132, 2016/09/08 2016, doi: 10.1038/nenergy.2016.132.

[68] E. Peled, "The Electrochemical Behavior of Alkali and Alkaline Earth Metals in Nonaqueous Battery Systems—The Solid Electrolyte Interphase Model," *Journal of The Electrochemical Society,* vol. 126, no. 12, pp. 2047-2051, December 1, 1979 1979, doi: 10.1149/1.2128859.

[69] N.-W. Li, Y.-X. Yin, C.-P. Yang, and Y.-G. Guo, "An Artificial Solid Electrolyte Interphase Layer for Stable Lithium Metal Anodes," *Advanced Materials,* vol. 28, no. 9, pp. 1853-1858, 2016, doi: 10.1002/adma.201504526.

[70] G. A. Umeda, E. Menke, M. Richard, K. L. Stamm, F. Wudl, and B. Dunn, "Protection of lithium metal surfaces using tetraethoxysilane," *Journal of Materials Chemistry,* 10.1039/C0JM02305A vol. 21, no. 5, pp. 1593-1599, 2011, doi: 10.1039/C0JM02305A.

[71] G. Zheng *et al.*, "Interconnected hollow carbon nanospheres for stable lithium metal anodes," *Nature Nanotechnology,* Article vol. 9, p. 618, 07/27/online 2014, doi: 10.1038/nnano.2014.152

[72] A. C. Kozen *et al.*, "Next-Generation Lithium Metal Anode Engineering via Atomic Layer Deposition," *ACS Nano,* vol. 9, no. 6, pp. 5884-5892, 2015/06/23 2015, doi: 10.1021/acsnano.5b02166.

[73] X.-B. Cheng, R. Zhang, C.-Z. Zhao, and Q. Zhang, "Toward Safe Lithium Metal Anode in Rechargeable Batteries: A Review," *Chemical Reviews,* vol. 117, no. 15, pp. 10403-10473, 2017/08/09 2017, doi: 10.1021/acs.chemrev.7b00115.

[74] K. Fu *et al.*, "Flexible, solid-state, ion-conducting membrane with 3D garnet nanofiber networks for lithium batteries," *Proceedings of the National Academy of Sciences,* vol. 113, no. 26, pp. 7094-7099, June 28, 2016 2016, doi: 10.1073/pnas.1600422113.

[75] R. Zhang, N.-W. Li, X.-B. Cheng, Y.-X. Yin, Q. Zhang, and Y.-G. Guo, "Advanced Micro/Nanostructures for Lithium Metal Anodes," *Advanced Science,* vol. 4, no. 3, pp. 1600445-n/a, 2017, Art no. 1600445, doi: 10.1002/advs.201600445.

[76] X.-B. Cheng *et al.*, "Dendrite-Free Lithium Deposition Induced by Uniformly Distributed Lithium Ions for Efficient Lithium Metal Batteries," *Advanced Materials,* vol. 28, no. 15, pp. 2888-2895, 2016, doi: 10.1002/adma.201506124.

[77] H. Al Salem, G. Babu, C. V. Rao, and L. M. R. Arava, "Electrocatalytic Polysulfide Traps for Controlling Redox Shuttle Process of Li–S Batteries," *Journal of the American Chemical Society,* vol. 137, no. 36, pp. 11542-11545, 2015/09/16 2015, doi: 10.1021/jacs.5b04472.

[78] J. W. Choi, J. K. Kim, G. Cheruvally, J. H. Ahn, H. J. Ahn, and K. W. Kim, "Rechargeable lithium/sulfur battery with suitable mixed liquid electrolytes," (in English), *Electrochimica Acta,* vol. 52, no. 5, pp. 2075-2082, Jan 1 2007, doi: 10.1016/j.electacta.2006.08.016.

[79] E. Peled, Y. Sternberg, A. Gorenshtein, and Y. Lavi, "Lithium-sulfur battery: evaluation of dioxolane-based electrolytes," *J Electrochem Soc,* vol. 136, no. 6, pp. 1621-1625, 1989.

[80] S. Zhang, K. Ueno, K. Dokko, and M. Watanabe, "Recent advances in electrolytes for lithium–sulfur batteries," *Advanced Energy Materials,* vol. 5, no. 16, 2015.

[81] J. Hassoun and B. Scrosati, "Moving to a Solid-State Configuration: A Valid Approach to Making Lithium-Sulfur Batteries Viable for Practical Applications," *Advanced Materials,* vol. 22, no. 45, pp. 5198-5201, 2010.

[82] Y.-S. Su and A. Manthiram, "A new approach to improve cycle performance of rechargeable lithium–sulfur batteries by inserting a free-standing MWCNT interlayer," *Chemical Communications,* vol. 48, no. 70, pp. 8817-8819, 2012.

[83] S. H. Chung and A. Manthiram, "Bifunctional Separator with a Light-Weight Carbon-Coating for Dynamically and Statically Stable Lithium-Sulfur Batteries," *Advanced Functional Materials,* vol. 24, no. 33, pp. 5299-5306, 2014.

[84] H. Yao *et al.*, "Improved lithium–sulfur batteries with a conductive coating on the separator to prevent the accumulation of inactive S-related species at the cathode–separator interface," *Energy & Environmental Science,* vol. 7, no. 10, pp. 3381-3390, 2014.

[85] S. Evers and L. F. Nazar, "New approaches for high energy density lithium–sulfur battery cathodes," *Accounts of chemical research,* vol. 46, no. 5, pp. 1135-1143, 2012.

[86] Q. Pang, X. Liang, C. Y. Kwok, and L. F. Nazar, "Advances in lithium–sulfur batteries based on multifunctional cathodes and electrolytes," *Nature Energy,* vol. 1, p. 16132, 2016.

[87] H.-K. Jing, L.-L. Kong, S. Liu, G.-R. Li, and X.-P. Gao, "Protected lithium anode with porous Al 2 O 3 layer for lithium–sulfur battery," *Journal of Materials Chemistry A,* vol. 3, no. 23, pp. 12213-12219, 2015.

[88] G. Ma *et al.*, "A lithium anode protection guided highly-stable lithium–sulfur battery," *Chemical Communications,* vol. 50, no. 91, pp. 14209-14212, 2014.

[89] X. Ji, K. T. Lee, and L. F. Nazar, "A highly ordered nanostructured carbon–sulphur cathode for lithium–sulphur batteries," *Nature materials,* vol. 8, no. 6, pp. 500-506, 2009.

[90] J. Guo, Y. Xu, and C. Wang, "Sulfur-impregnated disordered carbon nanotubes cathode for lithium–sulfur batteries," *Nano letters,* vol. 11, no. 10, pp. 4288-4294, 2011.

[91] N. Jayaprakash, J. Shen, S. S. Moganty, A. Corona, and L. A. Archer, "Porous hollow carbon@ sulfur composites for high-power lithium–sulfur batteries," *Angewandte Chemie,* vol. 123, no. 26, pp. 6026-6030, 2011.

[92] H. Yao *et al.*, "Improving lithium–sulphur batteries through spatial control of sulphur species deposition on a hybrid electrode surface," *Nature communications,* vol. 5, 2014.

[93] C. Zhang, H. B. Wu, C. Yuan, Z. Guo, and X. W. D. Lou, "Confining sulfur in double-shelled hollow carbon spheres for lithium–sulfur batteries," *Angewandte Chemie,* vol. 124, no. 38, pp. 9730-9733, 2012.

[94] X. Liang, C. Hart, Q. Pang, A. Garsuch, T. Weiss, and L. F. Nazar, "A highly efficient polysulfide mediator for lithium–sulfur batteries," *Nature communications,* vol. 6, 2015.

[95] M. Liu, F. Ye, W. Li, H. Li, and Y. Zhang, "Chemical routes toward long-lasting lithium/sulfur cells," *Nano Research,* vol. 9, no. 1, pp. 94-116, 2016.

[96] J. Zheng *et al.*, "Lewis acid–base interactions between polysulfides and metal organic framework in lithium sulfur batteries," *Nano letters,* vol. 14, no. 5, pp. 2345-2352, 2014.

[97] Q. Pang, D. Kundu, M. Cuisinier, and L. Nazar, "Surface-enhanced redox chemistry of polysulphides on a metallic and polar host for lithium-sulphur batteries," *Nature communications,* vol. 5, 2014.

[98] G. Babu, K. Ababtain, K. S. Ng, and L. M. R. Arava, "Electrocatalysis of lithium polysulfides: current collectors as electrodes in Li/S battery configuration," *Scientific reports,* vol. 5, 2015.

[99] N. S. Manan *et al.*, "Electrochemistry of sulfur and polysulfides in ionic liquids," *The Journal of Physical Chemistry B,* vol. 115, no. 47, pp. 13873-13879, 2011.

[100] Y. Jung, S. Kim, B.-S. Kim, D.-H. Han, S.-M. Park, and J. Kwak, "Effect of organic solvents and electrode materials on electrochemical reduction of sulfur," *INTERNATIONAL JOURNAL OF ELECTROCHEMICAL SCIENCE,* vol. 3, no. 5, pp. 566-577, 2008.

[101] R. P. Martin, W. H. Doub Jr, J. L. Roberts Jr, and D. T. Sawyer, "Electrochemical reduction of sulfur in aprotic solvents," *Inorganic Chemistry,* vol. 12, no. 8, pp. 1921-1925, 1973.

[102] E. Levillain, F. Gaillard, P. Leghie, A. Demortier, and J. Lelieur, "On the understanding of the reduction of sulfur (S 8) in dimethylformamide (DMF)," *J Electroanal Chem,* vol. 420, no. 1, pp. 167-177, 1997.

[103] A. Evans, M. Montenegro, and D. Pletcher, "The mechanism for the cathodic reduction of sulphur in dimethylformamide: low temperature voltammetry," *Electrochemistry communications,* vol. 3, no. 9, pp. 514-518, 2001.

[104] Y.-C. Lu, Q. He, and H. A. Gasteiger, "Probing the Lithium–Sulfur Redox Reactions: A Rotating-Ring Disk Electrode Study," *The Journal of Physical Chemistry C,* vol. 118, no. 11, pp. 5733-5741, 2014.

[105] R. Xu, J. Lu, and K. Amine, "Progress in Mechanistic Understanding and Characterization Techniques of Li-S Batteries," *Advanced Energy Materials,* vol. 5, no. 16, 2015.

[106] M. Wild *et al.*, "Lithium sulfur batteries, a mechanistic review," *Energy & Environmental Science,* vol. 8, no. 12, pp. 3477-3494, 2015.

[107] H. Yamin, A. Gorenshtein, J. Penciner, Y. Sternberg, and E. Peled, "Lithium sulfur battery oxidation/reduction mechanisms of polysulfides in THF solutions," *J Electrochem Soc,* vol. 135, no. 5, pp. 1045-1048, 1988.

[108] H. Yamin, J. Penciner, A. Gorenshtain, M. Elam, and E. Peled, "The electrochemical behavior of polysulfides in tetrahydrofuran," *Journal of Power Sources,* vol. 14, no. 1–3, pp. 129-134, 1// 1985, doi: http://dx.doi.org/10.1016/0378-7753(85)88022-8.

[109] S. Abada, G. Marlair, A. Lecocq, M. Petit, V. Sauvant-Moynot, and F. Huet, "Safety focused modeling of lithium-ion batteries: A review," (in English), *Journal of Power Sources,* vol. 306, pp. 178-192, Feb 29 2016, doi: 10.1016/j.jpowsour.2015.11.100.

[110] G. Hodes, J. Manassen, and D. Cahen, "Photo-electrochemical energy conversion: electrocatalytic sulphur electrodes," *J Appl Electrochem,* vol. 7, no. 2, pp. 181-182, 1977.

[111] G. Hodes, J. Manassen, and D. Cahen, "Electrocatalytic electrodes for the polysulfide redox system," *J Electrochem Soc,* vol. 127, no. 3, pp. 544-549, 1980.

[112] I. E. Stephens, C. Ducati, and D. J. Fray, "Correlating microstructure and activity for polysulfide reduction and oxidation at WS2 electrocatalysts," *J Electrochem Soc,* vol. 160, no. 6, pp. A757-A768, 2013.

[113] P. Zhao, H. Zhang, H. Zhou, and B. Yi, "Nickel foam and carbon felt applications for sodium polysulfide/bromine redox flow battery electrodes," *Electrochimica Acta,* vol. 51, no. 6, pp. 1091-1098, 2005.

[114] Y. Shao *et al.*, "Nanostructured Electrocatalysts for PEM Fuel Cells and Redox Flow Batteries: A Selected Review," *ACS Catalysis,* vol. 5, no. 12, pp. 7288-7298, 2015/12/04 2015, doi: 10.1021/acscatal.5b01737.

[115] H. J. Peng *et al.*, "Enhanced Electrochemical Kinetics on Conductive Polar Mediators for Lithium–Sulfur Batteries," *Angewandte Chemie,* vol. 128, no. 42, pp. 13184-13189, 2016.

[116] S. Kapusta, A. Viehbeck, S. Wilhelm, and N. Hackerman, "The anodic oxidation of sulfide on platinum electrodes," *Journal of Electroanalytical Chemistry and Interfacial Electrochemistry,* vol. 153, no. 1-2, pp. 157-174, 1983.

[117] Y.-E. Sung, W. Chrzanowski, A. Zolfaghari, G. Jerkiewicz, and A. Wieckowski, "Structure of chemisorbed sulfur on a Pt (111) electrode," *Journal of the American Chemical Society,* vol. 119, no. 1, pp. 194-200, 1997.

[118] F. C. Anson and R. A. Osteryoung, "Chronocoulometry: A convenient, rapid and reliable technique for detection and determination of adsorbed reactants," vol. 60, no. 4, pp. 293-296, 1983, doi: 10.1021/ed060p293.

[119] F. C. Anson, "Innovations in the Study of Adsorbed Reactants by Chronocoulometry," *Analytical Chemistry,* vol. 38, no. 1, pp. 54-57, 1966/01/01 1966, doi: 10.1021/ac60233a014.

[120] G. Babu, N. Masurkar, H. Al Salem, and L. M. Arava, "Transition Metal Dichalcogenide Atomic Layers for Lithium Polysulfides Electrocatalysis," *J Am Chem Soc,* vol. 139, no. 1, pp. 171-178, Jan 11 2017, doi: 10.1021/jacs.6b08681.

[121] Z. Liu and P. P. Mukherjee, "Mesoscale Elucidation of Surface Passivation in the Li–Sulfur Battery Cathode," *ACS Applied Materials & Interfaces,* vol. 9, no. 6, pp. 5263-5271, 2017/02/15 2017, doi: 10.1021/acsami.6b15066.

[122] F. Y. Fan, W. C. Carter, and Y.-M. Chiang, "Mechanism and Kinetics of Li2S Precipitation in Lithium–Sulfur Batteries," *Advanced Materials,* vol. 27, no. 35, pp. 5203-5209, 2015, doi: 10.1002/adma.201501559.

[123] Q. Zhang, Y. Wang, Z. W. Seh, Z. Fu, R. Zhang, and Y. Cui, "Understanding the Anchoring Effect of Two-Dimensional Layered Materials for Lithium–Sulfur Batteries," *Nano Letters,* vol. 15, no. 6, pp. 3780-3786, 2015/06/10 2015, doi: 10.1021/acs.nanolett.5b00367.

[124] X. Liang, A. Garsuch, and L. F. Nazar, "Sulfur Cathodes Based on Conductive MXene Nanosheets for High-Performance Lithium–Sulfur Batteries," *Angewandte Chemie International Edition,* vol. 54, no. 13, pp. 3907-3911, 2015, doi: 10.1002/anie.201410174.

[125] A. Bruix *et al.*, "In Situ Detection of Active Edge Sites in Single-Layer MoS2 Catalysts," (in eng), *ACS Nano,* vol. 9, no. 9, pp. 9322-30, Sep 22 2015, doi: 10.1021/acsnano.5b03199.

[126] F. Bonaccorso *et al.*, "2D materials. Graphene, related two-dimensional crystals, and hybrid systems for energy conversion and storage," (in eng), *Science,* vol. 347, no. 6217, p. 1246501, Jan 2 2015, doi: 10.1126/science.1246501.

[127] D. Voiry *et al.*, "Enhanced catalytic activity in strained chemically exfoliated WS_2 nanosheets for hydrogen evolution," (in eng), *Nat Mater,* vol. 12, no. 9, pp. 850-5, Sep 2013, doi: 10.1038/nmat3700.

[128] X. Chen, Y. Gu, G. Tao, Y. Pei, G. Wang, and N. Cui, "Origin of hydrogen evolution activity on MS2 (M = Mo or Nb) monolayers," *Journal of Materials Chemistry A,* 10.1039/C5TA02817E vol. 3, no. 37, pp. 18898-18905, 2015, doi: 10.1039/C5TA02817E.

[129] X. Yu, M. S. Prévot, N. Guijarro, and K. Sivula, "Self-assembled 2D WSe2 thin films for photoelectrochemical hydrogen production," *Nature Communications,* vol. 6, no. 1, p. 7596, 2015/07/01 2015, doi: 10.1038/ncomms8596.

[130] Q. Lu, Y. Yu, Q. Ma, B. Chen, and H. Zhang, "2D Transition-Metal-Dichalcogenide-Nanosheet-Based Composites for Photocatalytic and Electrocatalytic Hydrogen Evolution Reactions," (in eng), *Adv Mater,* vol. 28, no. 10, pp. 1917-33, Mar 9 2016, doi: 10.1002/adma.201503270.

[131] I. E. L. Stephens, C. Ducati, and D. J. Fray, "Correlating Microstructure and Activity for Polysulfide Reduction and Oxidation at WS2 Electrocatalysts," *Journal of The Electrochemical Society,* vol. 160, no. 6, pp. A757-A768, 2013, doi: 10.1149/2.027306jes.

[132] M. Chhowalla, H. S. Shin, G. Eda, L.-J. Li, K. P. Loh, and H. Zhang, "The chemistry of two-dimensional layered transition metal dichalcogenide nanosheets," *Nat Chem,* 10.1038/nchem.1589 vol. 5, no. 4, pp. 263-275, 04//print 2013.

[133] Y. Gong *et al.*, "Vertical and in-plane heterostructures from WS2/MoS2 monolayers," (in eng), *Nat Mater,* vol. 13, no. 12, pp. 1135-42, Dec 2014, doi: 10.1038/nmat4091.

[134] Z. Chen, D. Cummins, B. N. Reinecke, E. Clark, M. K. Sunkara, and T. F. Jaramillo, "Core–shell MoO3–MoS2 Nanowires for Hydrogen Evolution: A Functional Design for Electrocatalytic Materials," *Nano Letters,* vol. 11, no. 10, pp. 4168-4175, 2011/10/12 2011, doi: 10.1021/nl2020476.

[135] T. A. Shifa *et al.*, "A vertical-oriented WS2 nanosheet sensitized by graphene: an advanced electrocatalyst for hydrogen evolution reaction," (in eng), *Nanoscale,* vol. 7, no. 35, pp. 14760-5, Sep 21 2015, doi: 10.1039/c5nr03704b.

[136] X. Geng *et al.*, "Pure and stable metallic phase molybdenum disulfide nanosheets for hydrogen evolution reaction," (in eng), *Nat Commun,* vol. 7, p. 10672, Feb 10 2016, doi: 10.1038/ncomms10672.

[137] X. Shang *et al.*, "Oriented Stacking along Vertical (002) Planes of MoS2: A Novel Assembling Style to Enhance Activity for Hydrogen Evolution," *Electrochimica Acta,* vol. 224, no. Supplement C, pp. 25-31, 2017/01/10/ 2017, doi: https://doi.org/10.1016/j.electacta.2016.12.027.

[138] W.-H. Hu *et al.*, "Effect of pH on the growth of MoS2 (002) plane and electrocatalytic activity for HER," *International Journal of Hydrogen Energy,* vol. 41, no. 1, pp. 294-299, 2016/01/05/ 2016, doi: https://doi.org/10.1016/j.ijhydene.2015.09.076.

[139] W.-H. Hu *et al.*, "MoSx supported graphene oxides with different degree of oxidation as efficient electrocatalysts for hydrogen evolution," *Carbon,* vol. 100, no. Supplement C, pp. 236-242, 2016/04/01/ 2016, doi: https://doi.org/10.1016/j.carbon.2016.01.019.

[140] G.-Q. Han *et al.*, "Electrodeposited MoSx films assisted by liquid crystal template with ultrahigh electrocatalytic activity for hydrogen evolution reaction," *International Journal of Hydrogen Energy,* vol. 42, no. 8, pp. 5132-5138, 2017/02/23/ 2017, doi: https://doi.org/10.1016/j.ijhydene.2017.01.009.

[141] W. Ge, K. Kawahara, M. Tsuji, and H. Ago, "Large-scale synthesis of NbS2 nanosheets with controlled orientation on graphene by ambient pressure CVD," *Nanoscale,* 10.1039/C3NR00723E vol. 5, no. 13, pp. 5773-5778, 2013, doi: 10.1039/C3NR00723E.

[142] J. A. Wilson and A. D. Yoffe, "The transition metal dichalcogenides discussion and interpretation of the observed optical, electrical and structural properties," *Advances in Physics,* vol. 18, no. 73, pp. 193-335, 1969/05/01 1969, doi: 10.1080/00018736900101307.

[143] Y. Zhou *et al.*, "Tensile Strain Switched Ferromagnetism in Layered NbS2 and NbSe2," *ACS Nano,* vol. 6, no. 11, pp. 9727-9736, 2012/11/27 2012, doi: 10.1021/nn303198w.

[144] W. G. Fisher and M. J. Sienko, "Stoichiometry, structure, and physical properties of niobium disulfide," *Inorganic Chemistry,* vol. 19, no. 1, pp. 39-43, 1980/01/01 1980, doi: 10.1021/ic50203a009.

[145] C. Geantet, J. Afonso, M. Breysse, N. Allali, and M. Danot, "Niobium sulfides as catalysts for hydrotreating reactions," *Catalysis today,* vol. 28, no. 1-2, pp. 23-30, 1996, doi: 10.1016/0920-5861(95)00215-4.

[146] N. Kumagai and K. Tanno, "Kinetic and structural characteristics of 3R-niobium disulfide as a positive material for secondary lithium batteries," *Electrochimica acta,* vol. 36, no. 5-6, pp. 935-941, 01/1991, doi: 10.1016/0013-4686(91)85297-K.

[147] W. M. R. Divigalpitiya, R. F. Frindt, and S. R. Morrison, "Effect of humidity on spread NbS 2 films," *Journal of Physics D: Applied Physics,* vol. 23, no. 7, p. 966, 1990. [

[148] Y. Zhang *et al.*, "Controlled Growth of High-Quality Monolayer WS2 Layers on Sapphire and Imaging Its Grain Boundary," *ACS Nano,* vol. 7, no. 10, pp. 8963-8971, 2013/10/22 2013, doi: 10.1021/nn403454e.

[149] Y. Zhan, Z. Liu, S. Najmaei, P. M. Ajayan, and J. Lou, "Large-Area Vapor-Phase Growth and Characterization of MoS2 Atomic Layers on a SiO2 Substrate," *Small,* vol. 8, no. 7, pp. 966-971, 2012, doi: 10.1002/smll.201102654.

[150] J. K. Dash, L. Chen, P. H. Dinolfo, T.-M. Lu, and G.-C. Wang, "A Method Toward Fabricating Semiconducting 3R-NbS2 Ultrathin Films," *The Journal of Physical Chemistry C,* vol. 119, no. 34, pp. 19763-19771, 2015/08/27 2015, doi: 10.1021/acs.jpcc.5b04057.

[151] Claire J. Carmalt, Emily S. Peters, Ivan P. Parkin, Troy D. Manning, and Andrew L. Hector, "Chemical Vapor Deposition of Niobium Disulfide Thin Films," *European Journal of Inorganic Chemistry,* vol. 2004, no. 22, pp. 4470-4476, 2004, doi: 10.1002/ejic.200400308.

[152] J. Yuan *et al.*, "Facile Synthesis of Single Crystal Vanadium Disulfide Nanosheets by Chemical Vapor Deposition for Efficient Hydrogen Evolution Reaction," *Advanced Materials,* vol. 27, no. 37, pp. 5605-5609, 2015, doi: 10.1002/adma.201502075.

[153] Y. Li, Y. Yu, Y. Huang, R. A. Nielsen, and W. A. Goddard, "Engineering the Composition and Crystallinity of Molybdenum Sulfide for High-Performance Electrocatalytic Hydrogen Evolution," *ACS catalysis,* vol. 5, no. 1, pp. 448-455, 2015, doi: 10.1021/cs501635v.

[154] M. S. Dresselhaus and I. L. Thomas, "Alternative energy technologies," *Nature,* 10.1038/35104599 vol. 414, no. 6861, pp. 332-337, 11/15/print 2001. [

[155] X. Chia, A. Ambrosi, P. Lazar, Z. Sofer, and M. Pumera, "Electrocatalysis of layered Group 5 metallic transition metal dichalcogenides (MX2, M = V, Nb, and Ta; X = S, Se, and Te)," *Journal of Materials Chemistry A,* 10.1039/C6TA05110C vol. 4, no. 37, pp. 14241-14253, 2016, doi: 10.1039/C6TA05110C.

[156] C. Tsai, K. Chan, J. K. Nørskov, and F. Abild-Pedersen, "Theoretical insights into the hydrogen evolution activity of layered transition metal dichalcogenides," *Surface Science,* vol. 640, pp. 133-140, 10// 2015, doi: http://dx.doi.org/10.1016/j.susc.2015.01.019.

[157] D. Gopalakrishnan, D. Damien, and M. M. Shaijumon, "MoS2 Quantum Dot-Interspersed Exfoliated MoS2 Nanosheets," *ACS Nano,* vol. 8, no. 5, pp. 5297-5303, 2014/05/27 2014, doi: 10.1021/nn501479e.

[158] D. Gopalakrishnan *et al.*, "Electrochemical synthesis of luminescent MoS2 quantum dots," *Chemical Communications,* 10.1039/C4CC09826A vol. 51, no. 29, pp. 6293-6296, 2015, doi: 10.1039/C4CC09826A.

[159] D. R. Cummins *et al.*, "Efficient hydrogen evolution in transition metal dichalcogenides via a simple one-step hydrazine reaction," *Nature Communications,* Article vol. 7, p. 11857, 06/10/online 2016, doi: 10.1038/ncomms11857

[160] A. B. Laursen, S. Kegnaes, S. Dahl, and I. Chorkendorff, "Molybdenum sulfides-efficient and viable materials for electro - and photoelectrocatalytic hydrogen evolution," *Energy & Environmental Science,* 10.1039/C2EE02618J vol. 5, no. 2, pp. 5577-5591, 2012, doi: 10.1039/C2EE02618J.

[161] Y. Li, H. Wang, L. Xie, Y. Liang, G. Hong, and H. Dai, "MoS2 Nanoparticles Grown on Graphene: An Advanced Catalyst for the Hydrogen Evolution Reaction," *Journal of the American Chemical Society,* vol. 133, no. 19, pp. 7296-7299, 2011/05/18 2011, doi: 10.1021/ja201269b.

[162] J. Duan, S. Chen, M. Jaroniec, and S. Z. Qiao, "Porous C_3N_4 Nanolayers@N-Graphene Films as Catalyst Electrodes for Highly Efficient Hydrogen Evolution," *ACS Nano,* vol. 9, no. 1, pp. 931-940, 2015/01/27 2015, doi: 10.1021/nn506701x.

[163] J.-S. Li *et al.*, "Coupled molybdenum carbide and reduced graphene oxide electrocatalysts for efficient hydrogen evolution," *Nature Communications,* Article vol. 7, p. 11204, 04/01/online 2016, doi: 10.1038/ncomms11204

[164] P. C. K. Vesborg, B. Seger, and I. Chorkendorff, "Recent Development in Hydrogen Evolution Reaction Catalysts and Their Practical Implementation," *The Journal of Physical Chemistry Letters,* vol. 6, no. 6, pp. 951-957, 2015/03/19 2015, doi: 10.1021/acs.jpclett.5b00306.

[165] M. Zeng and Y. Li, "Recent advances in heterogeneous electrocatalysts for the hydrogen evolution reaction," *Journal of Materials Chemistry A,* 10.1039/C5TA02974K vol. 3, no. 29, pp. 14942-14962, 2015, doi: 10.1039/C5TA02974K.

[166] N. K. Thangavel, D. Gopalakrishnan, and L. M. R. Arava, "Understanding Heterogeneous Electrocatalysis of Lithium Polysulfide Redox on Pt and WS_2 Surfaces," *The Journal of Physical Chemistry C,* 2017/05/11 2017, doi: 10.1021/acs.jpcc.7b01514.

[167] P. G. Bruce, S. A. Freunberger, L. J. Hardwick, and J.-M. Tarascon, "Li–O_2 and Li–S batteries with high energy storage," *Nature Materials,* Review Article vol. 11, p. 19, 12/15/online 2011, doi: 10.1038/nmat3191.

[168] F. Croce, G. B. Appetecchi, L. Persi, and B. Scrosati, "Nanocomposite polymer electrolytes for lithium batteries," *Nature,* vol. 394, p. 456, 07/30/online 1998, doi: 10.1038/28818.

[169] Y. Lu, Z. Tu, and L. A. Archer, "Stable lithium electrodeposition in liquid and nanoporous solid electrolytes," *Nat Mater,* Article vol. 13, no. 10, pp. 961-969, 10//print 2014, doi: 10.1038/nmat4041

[170] P. G. Bruce, L. J. Hardwick, and K. M. Abraham, "Lithium-air and lithium-sulfur batteries," *MRS Bulletin,* vol. 36, no. 7, pp. 506-512, 2011, doi: 10.1557/mrs.2011.157.

[171] N. Nitta, F. Wu, J. T. Lee, and G. Yushin, "Li-ion battery materials: present and future," *Materials Today,* vol. 18, no. 5, pp. 252-264, 2015/06/01/ 2015, doi: https://doi.org/10.1016/j.mattod.2014.10.040.

[172] Y. Guo, H. Li, and T. Zhai, "Reviving Lithium-Metal Anodes for Next-Generation High-Energy Batteries," *Advanced Materials,* vol. 29, no. 29, p. 1700007, 2017/08/01 2017, doi: 10.1002/adma.201700007.

[173] D. Wang, W. Zhang, W. Zheng, X. Cui, T. Rojo, and Q. Zhang, "Towards High-Safe Lithium Metal Anodes: Suppressing Lithium Dendrites via Tuning Surface Energy," *Advanced Science,* vol. 4, no. 1, p. 1600168, 2017/01/01 2016, doi: 10.1002/advs.201600168.

[174] J. Tan, A. M. Tartakovsky, K. Ferris, and E. M. Ryan, "Investigating the Effects of Anisotropic Mass Transport on Dendrite Growth in High Energy Density Lithium Batteries," *Journal of The Electrochemical Society,* vol. 163, no. 2, pp. A318-A327, January 1, 2016 2016, doi: 10.1149/2.0951602jes.

[175] O. Crowther and A. C. West, "Effect of Electrolyte Composition on Lithium Dendrite Growth," *Journal of The Electrochemical Society,* vol. 155, no. 11, pp. A806-A811, November 1, 2008 2008, doi: 10.1149/1.2969424.

[176] J.-G. Zhang, W. Xu, and W. A. Henderson, "Characterization and Modeling of Lithium Dendrite Growth," in *Lithium Metal Anodes and Rechargeable Lithium Metal Batteries*. Cham: Springer International Publishing, 2017, pp. 5-43.

[177] C. T. Love, O. A. Baturina, and K. E. Swider-Lyons, "Observation of Lithium Dendrites at Ambient Temperature and Below," *ECS Electrochemistry Letters,* vol. 4, no. 2, pp. A24-A27, 2015, doi: 10.1149/2.0041502eel.

[178] P. Barai, K. Higa, and V. Srinivasan, "Impact of Electrolyte Transference Number on Lithium Dendrite Growth Process," *Meeting Abstracts,* vol. MA2017-02, no. 1, pp. 66-66, 2017.

[179] K. Deng *et al.*, "Effective Suppression of Lithium Dendrite Growth Using a Flexible Single-Ion Conducting Polymer Electrolyte," *Small,* vol. 14, no. 31, p. 1801420, 2018/08/01 2018, doi: 10.1002/smll.201801420.

[180] M. Yoshio, M. Yoshio, T. Mukai, K. Kanie, and M. Yoshizawa, "Layered Ionic Liquids: Anisotropic Ion Conduction in New Self-Organized Liquid-Crystalline Materials," *Advanced materials (Weinheim),* vol. 14, no. 5, p. 351, 04/2002, doi: 10.1002/1521-4095(20020304)14:5<351::AID-ADMA351>3.0.CO;2-D.

[181] M. Yoshio, T. Kato, T. Mukai, M. Yoshizawa, and H. Ohno, "SELF-ASSEMBLY OF AN IONIC LIQUID AND A HYDROXYL-TERMINATED LIQUID CRYSTAL: ANISOTROPIC ION CONDUCTION IN LAYERED NANOSTRUCTURES," *Molecular Crystals and Liquid Crystals,* vol. 413, no. 1, pp. 99-108, 2004/01/01 2004, doi: 10.1080/15421400490432632.

[182] Y. Uchida, T. Matsumoto, T. Akita, and N. Nishiyama, "Ion conductive properties in ionic liquid crystalline phases confined in a porous membrane," *Journal of Materials Chemistry C,* 10.1039/C5TC00314H vol. 3, no. 24, pp. 6144-6147, 2015, doi: 10.1039/C5TC00314H.

[183] M. Galiński, A. Lewandowski, and I. Stępniak, "Ionic liquids as electrolytes," *Electrochimica Acta,* vol. 51, no. 26, pp. 5567-5580, 8/15/ 2006, doi: http://dx.doi.org/10.1016/j.electacta.2006.03.016.

[184] R. Sasi, S. Sarojam, and S. J. Devaki, "High Performing Biobased Ionic Liquid Crystal Electrolytes for Supercapacitors," *ACS Sustainable Chemistry & Engineering,* vol. 4, no. 6, pp. 3535-3543, 2016/06/06 2016, doi: 10.1021/acssuschemeng.6b00585.

[185] R. Sasi, K. B. Jinesh, and S. J. Devaki, "Anisotropic Phase Formation Induced Enhancement of Resistive Switching in Bio–based Imidazolium Ionic Liquid Crystals," *ChemistrySelect,* vol. 2, no. 1, pp. 315-319, 2017/01/10 2017, doi: 10.1002/slct.201601715.

[186] J. Sakuda *et al.*, "Liquid-Crystalline Electrolytes for Lithium-Ion Batteries: Ordered Assemblies of a Mesogen-Containing Carbonate and a Lithium Salt," *Advanced Functional Materials,* vol. 25, no. 8, pp. 1206-1212, 2015, doi: 10.1002/adfm.201402509.

[187] S. Ermakov, A. Beletskii, O. Eismont, and V. Nikolaev, "Brief Review of Liquid Crystals," in *Liquid Crystals in Biotribology*, (Biological and Medical Physics, Biomedical Engineering: Springer International Publishing, 2016, ch. 2, pp. 37-56.

[188] Q. Chen and M. Hird, "Synthesis, mesomorphic behaviour and optical anisotropy of some novel liquid crystals with lateral and terminal fluoro substituents and a 2,6-disubstituted naphthalene core," *Liquid Crystals,* vol. 42, no. 5-6, pp. 877-886, 2015/06/03 2015, doi: 10.1080/02678292.2014.987706.

[189] P. Medle Rupnik, D. Lisjak, M. Čopič, and A. Mertelj, "Ferromagnetic liquid crystals for magnetic field visualisation," *Liquid Crystals,* pp. 1-5, 2015, doi: 10.1080/02678292.2015.1049570.

[190] D. Ster, U. Baumeister, J. L. Chao, C. Tschierske, and G. Israel, "Synthesis and mesophase behaviour of ionic liquid crystals," *Journal of Materials Chemistry,* 10.1039/B705519F vol. 17, no. 32, pp. 3393-3400, 2007, doi: 10.1039/B705519F.

[191] K. Binnemans, "Ionic Liquid Crystals," *Chemical Reviews,* vol. 105, no. 11, pp. 4148-4204, 2005/11/01 2005, doi: 10.1021/cr0400919.

[192] A. Alvarez Fernandez and P. H. J. Kouwer, "Key Developments in Ionic Liquid Crystals," *International Journal of Molecular Sciences,* vol. 17, no. 5, p. 731, 2016, doi: 10.3390/ijms17050731.

[193] K. Goossens, K. Lava, C. W. Bielawski, and K. Binnemans, "Ionic Liquid Crystals: Versatile Materials," *Chemical Reviews,* vol. 116, no. 8, pp. 4643-4807, 2016/04/27 2016, doi: 10.1021/cr400334b.

[194] A. Balducci, "Ionic Liquids in Lithium-Ion Batteries," *Topics in Current Chemistry,* journal article vol. 375, no. 2, p. 20, February 02 2017, doi: 10.1007/s41061-017-0109-8.

[195] S. J. Devaki and R. Sasi, "Ionic Liquids/Ionic Liquid Crystals for Safe and Sustainable Energy Storage Systems," in *Progress and Developments in Ionic Liquids*, S. Handy Ed. Rijeka: InTech, 2017, p. Ch. 14.

[196] A. E. Skoulios and V. Luzzati, "La structure des colloides d'association. III. Description des phases mesomorphes des savons de sodium purs, rencontrees au-dessus de 100degreesC," *Acta Crystallographica,* vol. 14, no. 3, pp. 278-286, 1961, doi: doi:10.1107/S0365110X61000863.

[197] V. Busico, P. Cernicchiaro, P. Corradini, and M. Vacatello, "Polymorphism in anhydrous amphiphilic systems. Long-chain primary n-alkylammonium chlorides," *The Journal of Physical Chemistry,* vol. 87, no. 9, pp. 1631-1635, 1983/04/01 1983, doi: 10.1021/j100232a035.

[198] C. M. Gordon, J. D. Holbrey, A. R. Kennedy, and K. R. Seddon, "Ionic liquid crystals: hexafluorophosphate salts," *Journal of Materials Chemistry,* 10.1039/A806169F vol. 8, no. 12, pp. 2627-2636, 1998, doi: 10.1039/A806169F.

[199] K. Hoshino, M. Yoshio, T. Mukai, K. Kishimoto, H. Ohno, and T. Kato, "Nanostructured ion-conductive films: Layered assembly of a side-chain liquid-crystalline polymer with an imidazolium ionic moiety," *Journal of Polymer Science Part A: Polymer Chemistry,* vol. 41, no. 22, pp. 3486-3492, 2003, doi: 10.1002/pola.10832.

[200] H. K. Bisoyi and S. Kumar, "Discotic nematic liquid crystals: science and technology," *Chemical Society Reviews,* 10.1039/B901792P vol. 39, no. 1, pp. 264-285, 2010, doi: 10.1039/B901792P.

[201] N. Hoshino, H. Murakami, Y. Matsunaga, T. Inabe, and Y. Maruyama, "Liquid crystalline copper(II) complexes of N-salicylideneaniline derivatives. Mesomorphic properties and a crystal structure," *Inorganic Chemistry,* vol. 29, no. 6, pp. 1177-1181, 1990/03/01 1990, doi: 10.1021/ic00331a014.

[202] W. Fischer and J. Brickmann, "Lennard-Jones (12,6) Parameters for the Non-Ionic Contributions to Interionic Pairpotentials of Alkali Cations and Halide Anions from Crystal Data," *Berichte der Bunsengesellschaft für physikalische Chemie,* vol. 86, no. 7, pp. 650-656, 1982, doi: 10.1002/bbpc.19820860715.

[203] C. J. Bowlas, D. W. Bruce, and K. R. Seddon, "Liquid-crystalline ionic liquids," *Chem. Commun.,* no. 14, pp. 1625-1626, 1996.

[204] S. Ujiie and K. Iimura, "Ion Complex Type of Novel Chiral Smectic C[*] Liquid Crystal Having Chiral Hydrogentartrate Counterion," *Chemistry Letters,* vol. 23, no. 1, pp. 17-20, 1994, doi: 10.1246/cl.1994.17.

[205] K. Ming Lee, C. Kuan Lee, and I. J. B. Lin, "First example of interdigitated U-shape benzimidazolium ionic liquid crystals," *Chemical Communications,* 10.1039/A608517B no. 9, pp. 899-900, 1997, doi: 10.1039/A608517B.

[206] J. D. Holbrey and K. R. Seddon, "The phase behaviour of 1-alkyl-3-methylimidazolium tetrafluoroborates; ionic liquids and ionic liquid crystals," *Journal of the Chemical Society, Dalton Transactions,* 10.1039/A902818H no. 13, pp. 2133-2140, 1999, doi: 10.1039/A902818H.

[207] J. Baudoux, P. Judeinstein, D. Cahard, and J.-C. Plaquevent, "Design and synthesis of novel ionic liquid/liquid crystals (IL2Cs) with axial chirality," *Tetrahedron Letters,* vol. 46, no. 7, pp. 1137-1140, 2/14/ 2005, doi: http://dx.doi.org/10.1016/j.tetlet.2004.12.097.

[208] W. Dobbs, L. Douce, L. Allouche, A. Louati, F. Malbosc, and R. Welter, "New ionic liquid crystals based on imidazolium salts," *New Journal of Chemistry,* 10.1039/B600279J vol. 30, no. 4, pp. 528-532, 2006, doi: 10.1039/B600279J.

[209] E. M. Ryan, A. M. Tartakovsky, and C. Amon, "Pore-scale modeling of competitive adsorption in porous media," *Journal of Contaminant Hydrology,* vol. 120-121, pp. 56-78, 2011/03/01/ 2011, doi: https://doi.org/10.1016/j.jconhyd.2010.06.008.

[210] J. J. Monaghan, "Smoothed particle hydrodynamics," *Reports on Progress in Physics,* vol. 68, p. 1703, 2005.

[211] E. M. Ryan and A. M. Tartakovsky, "A hybrid micro-scale model for transport in connected macro-pores in porous media," *Journal of Contaminant Hydrology,* vol. 126, no. 1, pp. 61-71, 2011/09/25/ 2011, doi: https://doi.org/10.1016/j.jconhyd.2011.06.005.

[212] J. Tan and E. M. Ryan, "Computational study of electro-convection effects on dendrite growth in batteries," *Journal of Power Sources,* vol. 323, pp. 67-77, 2016/08/15/ 2016, doi: https://doi.org/10.1016/j.jpowsour.2016.05.012.

[213] J. Tan and E. M. Ryan, "Structured electrolytes to suppress dendrite growth in high energy density batteries," *International Journal of Energy Research,* vol. 40, no. 13, pp. 1800-1810, 2016/10/25 2016, doi: 10.1002/er.3560.

[214] S. Plimpton, "Fast Parallel Algorithms for Short-Range Molecular Dynamics," *Journal of Computational Physics,* vol. 117, no. 1, pp. 1-19, 1995/03/01/ 1995, doi: https://doi.org/10.1006/jcph.1995.1039.

[215] S. Singh and D. Dunmur, *Liquid Crystals : Fundamentals*. Singapore, SINGAPORE: World Scientific Publishing Co Pte Ltd, 2002.

[216] S. Singh, "Phase transitions in liquid crystals," *Physics Reports,* vol. 324, no. 2, pp. 107-269, 2000/02/01/ 2000, doi: https://doi.org/10.1016/S0370-1573(99)00049-6.

[217] M. Subrao, D. M. Potukuchi, G. Sharada Ramachandra, and P. Bhagavath, "Novel biphenyl-substituted 1,2,4-oxadiazole ferroelectric liquid crystals: synthesis and characterization," *Beilstein journal of organic chemistry,* vol. 11, pp. 233-241, 2015, doi: 10.3762/bjoc.11.26.

[218] A. Guerfi *et al.*, "Improved electrolytes for Li-ion batteries: Mixtures of ionic liquid and organic electrolyte with enhanced safety and electrochemical performance," *Journal of Power Sources,* vol. 195, no. 3, pp. 845-852, 2/1/ 2010, doi: http://dx.doi.org/10.1016/j.jpowsour.2009.08.056.

[219] Y. Lu, Z. Tu, and L. A. Archer, "Stable lithium electrodeposition in liquid and nanoporous solid electrolytes," *Nature Materials,* Article vol. 13, p. 961, 08/10/online 2014, doi: 10.1038/nmat4041

[220] W.-K. Shin, A. G. Kannan, and D.-W. Kim, "Effective Suppression of Dendritic Lithium Growth Using an Ultrathin Coating of Nitrogen and Sulfur Codoped Graphene Nanosheets on Polymer Separator for Lithium Metal Batteries," *ACS applied materials & interfaces,* vol. 7, no. 42, pp. 23700-23707, 28/2015, doi: 10.1021/acsami.5b07730.

[221] N. Schweikert *et al.*, "Suppressed lithium dendrite growth in lithium batteries using ionic liquid electrolytes: Investigation by electrochemical impedance spectroscopy, scanning electron microscopy, and in situ 7Li nuclear magnetic resonance spectroscopy," *Journal of Power Sources,* vol. 228, pp. 237-243, 4/15/ 2013, doi: http://dx.doi.org/10.1016/j.jpowsour.2012.11.124.

[222] J. Jorne, "Transference Number Approaching Unity in Nanocomposite Electrolytes," *Nano Letters,* vol. 6, no. 12, pp. 2973-2976, 2006/12/01 2006, doi: 10.1021/nl062182m.

[223] L. Li, S. Li, and Y. Lu, "Suppression of dendritic lithium growth in lithium metal-based batteries," *Chemical Communications,* 10.1039/C8CC02280A vol. 54, no. 50, pp. 6648-6661, 2018, doi: 10.1039/C8CC02280A.

ABSTRACT

ADVANCED ELECTRODES AND ELECTROLYTES FOR LONG-LIVED AND HIGH-PERFORMANCE LITHIUM-SULFUR BATTERIES

by

DEEPESH GOPALAKRISHNAN

August 2020

Advisor: Dr. Leela Mohana Reddy Arava

Major: Mechanical Engineering

Degree: Doctor of Philosophy

Lithium – Sulfur (Li-S) batteries have received much attention and considered as a promising candidate for next generation energy storage devices because of their high theoretical energy density (≈2600 Wh kg^{-1}) and environmental friendliness. However, the uncontrollable growth of lithium dendrites in the lithium metal anode and the fatal effect of polysulfide shuttle hinder their practical applications. The formation of dendrites during repeated Li plating/stripping processes results in: reduced Li availability for the electrochemical reactions, disruption in Li transport through the interface causing rapid capacity decay and increased safety concerns due to short circuiting. Polysulfide shuttle is a common phenomenon in Li-S batteries where the soluble intermediate polysulfide species (Li_2S_x, $4 \leq \times \leq 8$) are inevitably produced and shuttled between cathode and anode, and react with the Li-metal to form insoluble Li_2S and Li_2S_2 on the surface of anode, resulting in surface passivation of Li metal anode, fast self-discharge and rapid capacity fading in Li-S batteries. Thus, the major problems from both anode and cathode side are needed to be addressed, preferably by employing effective strategies. These issues can be addressed only

when we have a better mechanistic understanding about chemical and electrochemical processes occurring in the Li-S battery.

In the past decade, several strategies have been developed around the world and recently, our group demonstrated utilization of electrocatalyst to improve the polysulfides reaction and trap them inside the cathode of Li−S battery[28, 29, 77]. The electrocatalyst reduces the energy barrier of electrochemical reaction and also act as an anchor for polysulfides and confide them to the cathode reducing their shuttle effect. Herein, we carried out fundamental electrochemical studies on the sulfur -electrocatalyst interface to develop a suitable catalytic cathode. The potentiodynamic and potentiostatic methodologies are used to infer diffusional, adsorption and the kinetics behavior of polysulfides with respect to catalytic and non-catalytic interfaces. In this context, we evaluated the kinetics of sulfur redox chemistry on different electrocatalytic surfaces such as Pt, WS_2 and NbS_2 and their influences on reaction kinetics at different stages. Also, we have demonstrated the influence of catalyst on solid-to-liquid & liquid-to-solid polysulfides reaction kinetics and their effect on Li_2S nucleation ending up in gaining of high capacity during the discharge process. In addition, we have explained in detail the impact of catalytic interface on cathode surfaces as well as on the reversibility of sulfur redox chemistry. We studied the synergistic effect of electrocatalyst NbS_2 and conductive carbon substrate in Li-S battery performance. The other issue that we address in the thesis is lithium dendrite formation in Li-S batteries. Though the dendrite formation is one of the oldest issues, fundamental understanding about how the interfacial chemistry and Li deposition is correlated, how anode overpotential affect the cell characteristics etc. are still have no answers which are essential to address the dendrite formation. Here, we demonstrate a novel strategy using a special class of ionic liquids (ILs) with liquid crystal properties called Ionic Liquid Crystals (ILCs) as electrolyte cum pseudo-separator to detain the dendrite growth with their

anisotropic nature controlling the Li-ion mass transport. The thermotropic ILC with two-dimensional Li-ion conducting pathways have been synthesized and well characterized. Detailed microscopic and spectroscopic analysis elucidates that the ILC is formed with Smectic A phase and can be utilized for wide temperature window operation. The electrochemical results corroborate the efficacy of ILC electrolytes in mitigating dendrites formation even after 800 hrs. and further substantiated by numerical simulation and deduced the mechanism involved in dendritic suppression. Thus, the research combines experimental development, characterization of the Ionic liquid crystals (ILCs) and analysis of their potential as electrolyte for improving Li battery performance supported by the numerical models.

AUTOBIOGRAPHICAL STATEMENT

DEEPESH GOPALAKRISHNAN

EDUCATION

Doctor of Philosophy, Wayne State University, Detroit, USA, 2015-2020
Master of Technology, University of Madras, Chennai, India, 2012
Bachelor of Science, Calicut University, Kerala, India, 2009

LIST OF JOURNAL PUBLICATIONS (Citations: 755; h-index: 8)

1. ***Gopalakrishnan, D***., Samia, A., Arava, L. M. R., Ionic Liquid Crystalline Electrolyte to suppress dendrite growth in Li metal-based batteries: An effect of anisotropic mass transport (Submitted to ACS Applied Materials and Interfaces, 2020).

2. ***Gopalakrishnan, D***., Lee,A., Thangavel, N., Arava, L. M. R.,2017, Facile synthesis of electrocatalytically active NbS_2 nanoflakes for enhanced hydrogen evolution reaction, Sustainable Energy & Fuels.

3. Arava, L. M. R., ***Gopalakrishnan, D***., Lee, A., 2017, "Electrocatalytically Active NbS_2 modified carbon cloth for Lithium-Sulfur Batteries", *ASME Journal of Electrochemical Energy Conversion and Storage*, 15(1), 011005.

4. Thangavel, N. K., ***Gopalakrishnan, D***., Arava, L. M. R., 2017, "Understanding Heterogeneous Electrocatalysis of Lithium Polysulfide Redox on Pt and WS_2 Surfaces", *The Journal of Physical Chemistry C*, 121 (23), 12718-12725.

5. Al Salem, H., Chitturi, V. R., Babu, G., ***Gopalakrishnan, D***., Arava, L. M. R., 2016, Stabilizing polysulfide-shuttle in a Li–S battery using transition metal carbide nanostructures", *RSC Advances*, 6 (111), 110301-110306.

6. ***Gopalakrishnan, D***.; Damien, D.; Shaijumon, M. M., MoS_2 Quantum Dot-Interspersed Exfoliated MoS2 Nanosheets. *ACS Nano* 2014, 8 (5), 5297.

7. ***Gopalakrishnan, D***.; Damien, D.; Li, B.; Gullappalli, H.; Pillai, V. K.; Ajayan, P. M.; Shaijumon, M. M., Electrochemical synthesis of luminescent MoS_2 quantum dots. *Chemical Communications* 2015, 51 (29), 6293-6296.

8. ***Gopalakrishnan, D***.; Bootharaju, M. S.; Udayabhaskararao, T.; Pradeep, T., Atomically precise silver clusters for efficient chlorocarbon degradation. Journal of Materials Chemistry A 2013, 1 (3), 611-620.

9. Chakraborty,I.;Udayabhaskararao,T. ;***Gopalakrishnan, D***.; Pradeep, T., Sunlight mediated synthesis and antibacterial properties of monolayer protected silver clusters. *Journal of Materials Chemistry B*, 2013, 1 (33), 4059-4064.

LIST OF PATENTS

1. Thalappil Pradeep, Indranath Chakraborty, Thumu Udayabhaskararao and ***Deepesh Gopalakrishnan***. "A method for preparing monolayer protected silver clusters as antibacterial agents." (Application no. 485/CHE/2013).
2. M. Shaijumon, ***Deepesh Gopalakrishnan*** and D. Damien,"A Single step process for the synthesis of MoS2 quantum dots". Indian Patent filed; (Application No: 3309/CHE/2014).
3. M. M. Shaijumon, ***Deepesh Gopalakrishnan*** and D. Damien, "Method for the Synthesis Of Layered Luminescent Transition Metal Dichalcogenide Quantum Dots". US Patent filed; (Publication No: 20170029962).